CLINICAL GRADE ACTIVE GUIDEWIRE DESIGN FOR CARDIOVASCULAR INTERVENTIONAL MRI

by

Merdim Sönmez

Bachelor of Science , in Electrical and Electronics Engineering, Middle East Technical University , 2004
Master of Science, in Biomedical Engineering, Bogazici University, 2008

Submitted to the Institute of Biomedical Engineering
in partial fulfillment of the requirements
for the degree of
Doctor
of
Philosophy

Boğaziçi University
2013

CLINICAL GRADE ACTIVE GUIDEWIRE DESIGN FOR CARDIOVASCULAR INTERVENTIONAL MRI

APPROVED BY:

Assist. Prof. Dr. Özgür Kocatürk (Thesis Advisor)	....
Prof. Dr. Cengizhan Öztürk	....
Assoc. Prof. Dr. Arda Deniz Yalçınkaya	....
Assoc. Prof. Dr. Ata Akın	....
Prof. Dr. Sabahattin Umman	....

DATE OF APPROVAL: 23.05.2013

ACKNOWLEDGMENTS

I would like to thank to Dr. Özgür Kocatürk for his guidance and support throughout my graduate training. Without his mentorship, this thesis would not have been possible. I would also like to thank Dr. Cengizhan Öztürk for introducing me to the world of MRI and his endless encouragement and support. In addition, I would like to express my gratitude to Dr. Robert J. Lederman for the critical insights he has provided along the way. His guidance and supervision have been invaluable to my graduate research, and I am grateful for his willingness to provide the resources of his lab.

I would also like to thank to my lab team for their strong support during my graduate training. I would like to thank Dominique for spending endless hours with me constructing and testing guidewires, putting together the FDA documentation, and for all her support during my thesis work. I would also like to thank Tony for his continuous support and patience in answering all of my questions, and Christina for spending so many hours with me during the heating tests and exploring solutions to heating problems. And I am thankful to Kanishka and Toby for helping with my animal experiments.

I would also like to express my thanks to Victor, Bill, and Kathy for their support and patience during my animal experiments.

I am extremely grateful to other members of NHLBI, especially Natalia and Michael, for showing me different perspectives on MRI safety and helping me to think about different aspects of MRI device design.

I would also like to thank my committee member, Dr.Arda Yalçınkaya for sharing his experience with electrical design.

Finally, I would like to thank my family and friends for supporting me in all my endeavors. I could not have come this far without their support. I would also like to thank my friends, Aytaç, Onur, and Murat for their friendship and support throughout my graduate training.

I am especially grateful to Pınar for her support, which has kept me motivated throughout this process.

ABSTRACT

CLINICAL GRADE ACTIVE GUIDEWIRE DESIGN FOR CARDIOVASCULAR INTERVENTIONAL MRI

In cardiovascular interventions, magnetic resonance imaging (MRI) can be used as an alternative to X-ray fluoroscopy to address problems such as soft tissue contrast and exposed ionized radiation. In recent years, advances in imaging techniques and innovative procedures have increased interest in using MRI guidance for minimally invasive procedure. An increasing number of procedures have been carried out on animals and quite a few studies have been conducted on humans. However, to accomplish a complete transition of MRI-guided therapies and treatments from animal experiments to clinic applications, some challenges need to be overcome. Chief among them is the fact that MRI-guided interventional procedures remain limited by a lack of availability of MR-compatible interventional instruments.

In this study, the main goal is to close the gap between investigational studies in animal and clinical applications. First, an MRI-compatible active guidewire for a clinical application was designed and tested. A $0.035''$ (128cm in length) active guidewire for MRI right and left heart catheterization at 1.5 T was manufactured in an ISO class 7 cleanroom. The design involved an internal fiber-optic temperature probe to monitor real-time temperature increases at the hottest spot of the guidewire to ensure patient safety during MRI scan. A solenoid coil at the distal end of the guidewire was also attached to change the current distribution of the guidewire and to create a conspicuous tip signal. Visualization of the exact location of the guidewire tip enhanced the safety and effectiveness of the right and left heart catheterization. And the mechanical requirements of the guidewire for right and left heart catheterization were met by using a taper nitinol wire as a core structure and thermoplastic elastomer material to support the entire structure. Second, the safety and effectiveness of the guidewire were evaluated through bench-top tests. The mechanical characteristics of the guidewire were compared to those of commercial counterparts. The guidewire design was modified until the mechanical requirements were met. The signal-to-noise ratio and imaging artifact were measured to evaluate the visibility of the guidewire. And a comprehensive in vitro heating test was conducted in an acrylic box filled with gel simulating human tissue conductivity. The longitudinal heating profile of the whole guidewire was acquired during these tests. In addition, the electrical safety of the guidewire was addressed by designing a leakage current blocking circuit to limit the leakage current.

The preclinical in vivo studies were designed and conducted in swine animal models to assess the feasibility of the guidewire during right and left heart catheterization. The studies complied with Good Laboratory Practice (GLP) standards. The guidewire was navigated through the vascular structure and chamber of the heart and used to support the diagnostic catheter. Extensive heating tests were performed to evaluate the heating risk of the guidewire. It was determined that guidewire visualization and mechanical properties were sufficient to complete all the steps during the procedures.

Finally, a proportional-integral-derivative (PID) controller was implemented to control the scan parameters during the MRI-guided procedure to ensure patient safety. The main aim was to reduce RF induced heating by dynamically adjusting the flip angle based on real- time temperature values coming from the guidewire shaft.

Keywords: Interventional Magnetic Resonance Imaging, Guidewire Design, Active Visualization, RF Safety, Preclinical In Vivo Study.

ÖZET

Girişimsel Kardiyovasküler Manyetik Rezonans Görüntüleme İçin Klinik Kılavuz Tel Tasarımı

Girişimsel kardiyovasküler müdahalelerde kullanılan X-ışını floroskopi, radyasyon yayılımı yapmakta ve yumuşak dokuyu görüntüleyememektedir. Bu yönteme alternatif olarak Manyetik Rezonans Görüntüleme (MRG) kulanabilir. Son yıllarda görüntüleme tekniklerindeki ilerlemeler, girişimsel prosedürlerde MRG kullanılımına olan ilgiyi arttırdı. Önemli ölçüde hayvan ve kısıtlı sayıda insan deneyi MRG yardımı ile yapıldı. MRG yardımıyla yapılan terapi ve tedavilerin hayvanlardan insanlara geçişi için bazı engellerin aşılması gerekmektedir. Bu engellerin içinde en önemlisi, Manyetik Rezonans (MR) uyumlu cihazların azlığıdır.

Bu çalışmadaki en önemli amaç, hayvan deneylerinden klinik deneylere geçişi sağlamakti. İlk önce, klinik uygulamalar için MR uyumlu aktif kılavuz tel tasarlandı ve test edildi. 1.5 T MR cihazında sağ ve sol kalp kateterizasyonu için, 0.035 inç çapında (128 cm uzunlukta) kılavuz tel ISO 7 temiz odada üretildi. Kılavuz tel üzerinde en sıcak noktadaki ısıyı gerçek zamanlı ölçebilmek için, kılavuz tel tasarımına fiber optik sıcaklık sensoru eklendi. Kılavuz telin ucuna yerleştirilen halka anten, telin distal ucundaki akım dağılımını değiştirerek ayırtedilebilir uç sinyali oluşturdu. Kılavuz tel ucun görüntüde tam olarak belirlenmesi, güvenli ve etkili sağ ve sol kalp kateterizasyonun gerçekleşmesini sağladı. Kılavuz telin mekanik özellikleri, uca doğru sivrilen nitinol tel ve telin gövdesini saran ısıl-plastik esnek madde ile iyileştirildi.

Kılavuz telin güvenlik ve etkinliği laboratuvar koşullarında test edildi. Mekaniksel özellikleri ticari kılavuz tellerle karşılaştırılarak test edildi. Kılavuz tel, mekaniksel gereksinimleri karşılama amacıyla tekrar geliştirildi. Sinyal-gürültü oranı ve görüntü bozulmaları hesaplandı. Kapsamlı sıcaklık testleri insan vücüdunu temsil eden jel ile doldurulmuş akrilik fantomda yapıldı. Bu testlerde, kılavuz tel üzerindeki boylamsal sıcaklık dağılımı ölçüldü.

Kılavuz telin sağ ve sol kalp kateterizasyona uygunluğu, klinik öncesi hayvan deneyleri ile test edildi. Deneyler İyi Klinik Uygulamaları standardı çerçevesinde gerçekleştirildi. Kılavuz tel damarlar ve kalpte başarıyla katetere kılavuzluk etti. Detaylı sıcaklık testlerinde kılavuz telin sıcaklığı ölçüldü. Kılavuz telin mekanik ve görüntüsel özellikleri, sağ ve sol kalp kateterizasyonun başarıyla tamamlanmasını sağladı.

Girişimsel MR prosedürlerinde, hasta güvenliğini sağlamak için PID denetleyici geliştirildi. Bu çalışmanın amaçı, görüntüleme parametrelerini dinamik olarak değiştirerek, radyo frekansından kaynaklanan ısınmaları engellemekti.

Anahtar Sözcükler: Girişimsel Manyetik Rezonans Görüntüleme, Atkif Kılavuz Tel Tasarımı, Radyo Frekans Güvenliği, Klinik Öncesi Hayvan Deneyi

TABLE OF CONTENTS

LIST OF FIGURES

LIST OF TABLES

LIST OF SYMBOLS

K_d	Derivative gain constant
K_i	Integral gain constant
K_p	Proportional gain constant
θ	Angle
ρ	Conductivity
σ	Density
γ	Gyromagnetic ratio
λ	Wavelength

LIST OF ABBREVIATIONS

ASTM	American Society for Testing and Materials
BNC	Bayonet Neill Concelman
bSSFP	Balanced Steady State Free Precession
CF	Cardiac Floating
Ch	Channel
DC	Direct Current
DTPA	Diethylenetriaminepentaacetic Acid
FA	Flip Angle
FISP	Fast Imaging with Steady-State Precession
Gd	Gadolinium
GLP	Good Laboratory Practice
GLP	Good Laboratory Practice
IEC	International Electrotechnical Commission
ISO	International Organization for Standardization
LC	Leakage Current
LCBC	Leakage Current Block Circuit
LED	Light-Emitting Diode
LV	Left Ventricle
MMCX	Micro-Miniature Connections
MR	Magnetic Resonance
MRI	Magnetic Resonance Imaging
MIP	Maximum Intensity Projection
NEMA	National Electrical Manufacturer Association
PAA	Polyacrylicacid
PIN	Positive-Intrinsic-Negative
PID	Proportional Integral Derivative
PTFE	Polytetrafluoroethylene
RF	Radio Frequency

ROI	Region of Interest
RV	Right Ventricle
SAR	Specific Absorption Rate
SNR	Signal to Noise Ratio
TE	Echo Time
TR	Repetition Time

1. INTRODUCTION

1.1 Motivation and Objectives

Interventional MRI has shown promise in terms of innovative procedures, most of which have been conducted in animals. However, interventional MRI has not been able to achieve a complete transition from animal experiments to clinical applications. Moreover, interventional instruments used during X-ray fluoroscopy are not compatible with the MRI environment either due to visibility or safety concerns. For this study, the objective was to develop and implement a clinical grade MRI compatible active guidewire that can be used to perform safe and effective cardiovascular procedures under MRI.

The specific aims of this study were: (i) to design and implement an MRI compatible, actively visualized, mechanically sound guidewire; (ii) to evaluate the safety and effectiveness of the active guidewire in bench-top and in vivo testing; and (iii) to implement a PID controller using real-time device temperature as a feedback and dynamically adjusting scan parameters to ensure patient safety while providing the maximum image SNR.

1.2 Overview of the Thesis

Chapter 1 provides an overview of MRI-guided procedures, interventional devices and the safety aspect of interventional MRI.

Chapter 2 introduces a novel guidewire design and discusses design parameters and preliminary test results.

Chapter 3 describes a comprehensive bench-top test used to assess the safety and effectiveness of the active guidewire.

Chapter 4 provides a detailed analysis of the preclinical study conduction on animal. Right and left heart catheterizations were performed on swine model using the active guidewire.

Chapter 5 discusses the implementation of a PID controller to adjust scan parameters in real time in order to ensure patient safety.

1.3 Interventional MRI

The field of interventional magnetic resonance imaging (iMRI) benefits from superior images of magnetic resonance imaging (MRI) which provides soft-tissue contrast, a multi-view oblique imaging plane, and functional and anatomical information. Recent advancements in real-time MRI enable non-invasive procedures under MRI as an alternative to X-ray fluoroscopy [1, 2, 3, 4]. While X-ray fluoroscopy is still the leading imaging modality for vascular intervention, it does not provide soft tissue contrast or 3D images. Contrast agents are used to visualize the contour of the vascular structures and cardiac chambers. However, there may be a patient population that is allergic to radio-opaque dyes [5]. There may also be inaccessible or occluded vessels that remain invisible. X-ray fluoroscopy also includes a risk of late cancer from exposure to ionizing radiation, especially for pediatric patients [6, 7]. Children with congenital heart diseases require multiple procedures. Even though patients are exposed to low-dose ionized radiation during the procedure, over the long term, accumulated doses can be such that the DNA of the cell can be damaged and chromosome alterations can be induced [8]. By contrast, MRI does not involve those risks and offers the additional advantage of providing soft-tissue visualization, cardiac motion, blood flow, and tissue perfusion [9].

Interventional vascular MRI guidance has been used in many investigational studies. For example, MRI guidance was used in closures of atrial or ventricular [10, 11] septal defects. Spuentrup et. al. [12] delivered passively-visualized stainless steel stents in coronary arteries of animal. Several groups have used MRI for atrial electrophysiological ablation therapies [13, 14, 15], cell delivery to infarct tissue [16], recanalization of occluded carotid arteries [17], dilatation of aortic coarctation [18], and valve placement [19, 20, 21]. Most of these procedures were conducted in animal models and showed promising results; however, few procedures have been conducted on humans.

Cardiovascular interventions require rapid imaging and data processing, high soft tissue contrast, and interactive control of the imaging plane. The need for rapid imaging of cardiovascular structures while creating contrast between blood and cardiac tissue has increased interest in balanced steady state free precession (bSSFP) [22]. Even though the bSSFP sequence suffers from bright fat signal, it is still desirable because of efficient use of magnetization, high contrast, and rapid scan. One disadvantage of this technique is higher specific absorption rates (SAR), which may cause high heat increases in the body. In an attempt to reduce SAR, spiral and radial sampling of k-space was introduced [23, 24, 25, 26].

Additionally, sophisticated filter techniques and pulse sequences enable diagnostic electrocardiogram monitoring [27, 28] and diagnostic electrophysiological mapping [29, 30, 31, 32] during MRI procedures.

1.3.1 Right Heart Catheterization

Right heart catheterization is performed to evaluate the performance of the heart by measuring the pressure in the heart and lungs and blood flow between the chambers. This is a routine procedure guided by X-ray fluoroscopy; however, MRI has been shown to overcome some problems associated with X-ray imaging such as poor visualization of heart chambers.

A recent research study on intravascular MRI published by Ratnayaka [33] involved the comparison of right heart pulmonary catheterization under X-ray fluoroscopy with real-time MRI-only guidance for 16 patients. The heart chambers were sampled for pressure and oximetry, and the time performance of catheter navigation between chambers was recorded. The study's authors found that catheterization times and success in reaching target areas in the heart under MRI were comparable. Researchers used two passive balloon catheters (gadolinium-filled and air-filled). Passive balloon catheter filled with gadolinium was more visible compared to catheter filled with air, as shown in Figure 1.1. In two incidents, catheter kinks were reported, therefore, the procedure was terminated and the catheter was withdrawn. The main reason for the failure was the lack of a stiff guidewire to support the catheter. The study authors emphasized the need for safe and visible MRI guidewires to improve the outcome of the procedure and speed up the procedure. Overall, it was an important study in terms of showing the feasibility of routine cardiovascular interventional magnetic resonance imaging in clinical applications.

Other successful MRI catheterization was conducted by another group. Researchers from King's College in London developed a cardiac catheterization under MRI and were able to navigate a passive non-braided catheter in 14 patients with congenital heart disease [34]. Only two patients in the study underwent diagnostic cardiac catheterization guided by MRI, but in the case of the other patients, partial X-ray and MRI guidance were required to complete the procedure. Using a non-braided catheter limited the torquability and steerability, which can pose a problem when used with seriously ill patients. On the basis of the study, researchers emphasized the need for conspicuous, safe, and mechanically adequate catheters and guidewires.

Muthurangu et. al. [35] conducted a study under MRI in 17 children or adults with pulmonary artery hypertension. The group showed the feasibility of total pulmonary arterial compliance measurement in humans by combining invasive pressure measurements and MR flow data. In addition, Kuehne et. al. [36] reported a study using MRI-guidance in 12 subjects, 6 control subjects, and 6 patients with chronic RV pressure overload from pulmonary hypertension; however, complete MRI catheterization was not performed. RV contractility was measured precisely with a method using MRI.

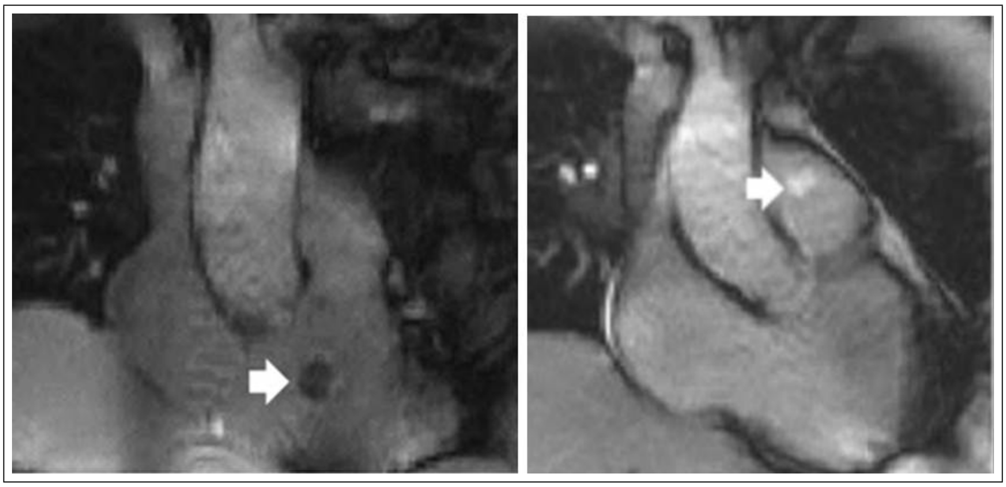

Figure 1.1 Magnetic resonance imaging catheterization using an air-filled (A) and gadolinium-filled (B) balloon catheter. White arrows indicate catheter tips when entering the main pulmonary artery from the right ventricle [33].

1.4 MRI Devices

Unlike X-ray guided interventional procedures that are well supported by a large number and variety of dedicated devices, MRI-guided applications are limited due to the lack of available MR-compatible interventional devices. In terms of design, device manufacturers need to consider not only the basic requirements for the intended use of interventional devices, but also the requirements for the MRI environment. One of these requirements is device visualization. There are two approaches to visualize the devices used in MRI: passive and active visualization.

1.4.1 Passive Devices

The passive approach relies on contrast agents or the material properties of the device. The intrinsic characteristic of a material can create field inhomogeneity, which may result in signal voids that appear dark in images, or enhance the local signal that appears as bright spots in images. Signal enhancement is usually accomplished by using paramagnetic materials on instruments [37, 38, 39], Figure 1.2.

Mekle et. al. [40] introduced a polymer-based, MR-compatible guidewire for

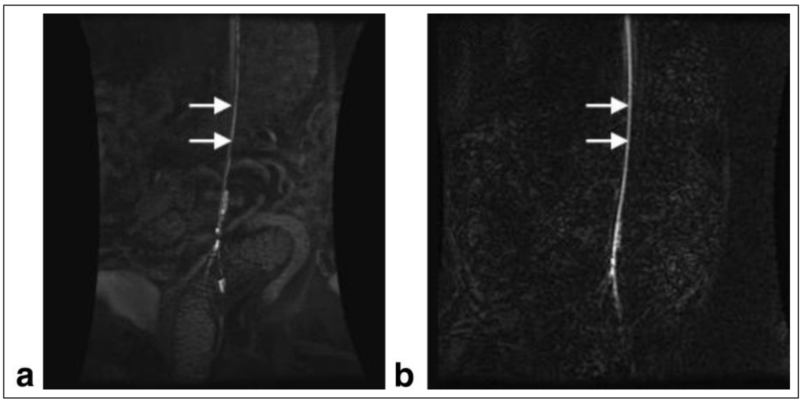

Figure 1.2 a: Coronal MIP image of a guidewire coated using Gd-DTPA in a canine aorta. b: The same guidewire with a projection dephaser in slice-select direction to suppress background signal in a canine aorta [37].

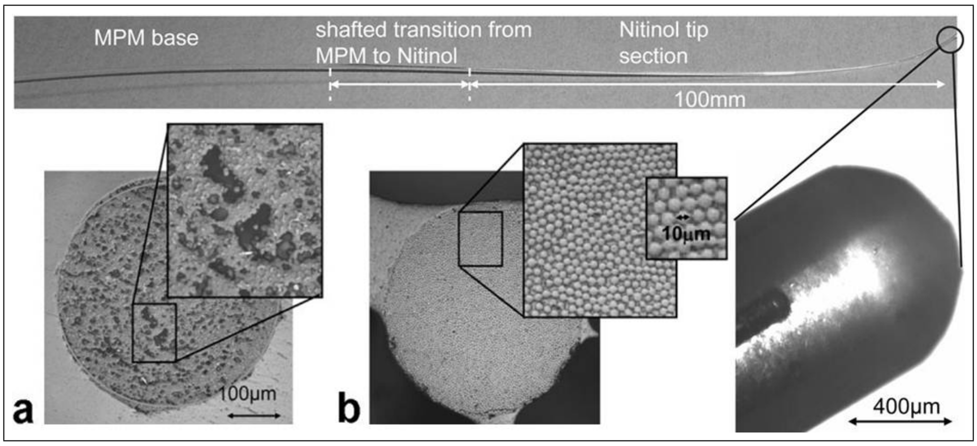

Figure 1.3 Schematic of guidewire design. The 0.018-inch micropultruded material core is shafted over a 25-mm transition region to a 100-mm-long Nitinol soft tip. (Left bottom) Microscopic sectional view of different qualities of the micropultruded material. (a) Material without optimization. (b) Material after optimization of the micropultrusion process. The improvement in fiber alignment and reduction of fiber gaps can be seen clearly [42].

MR-guided vascular interventions. A PEEK polymer based guidewire was coated with small iron particles (smaller than 10 micron) for passive device tracking. Buecker et. al. [41] used iron oxide markers to visualize a standard non-braided catheter consisting of nonconductive materials. Iron oxide markers changed the susceptibility of the catheter and created a distinct image artifact. However, the image artifact obscured the targeted anatomy and made it difficult to perform the procedure. Krueger et. al. [42] developed a guidewire from fiber-reinforced material, Figure 1.3, to mimic mechanical properties of commercially available X-ray guidewires.

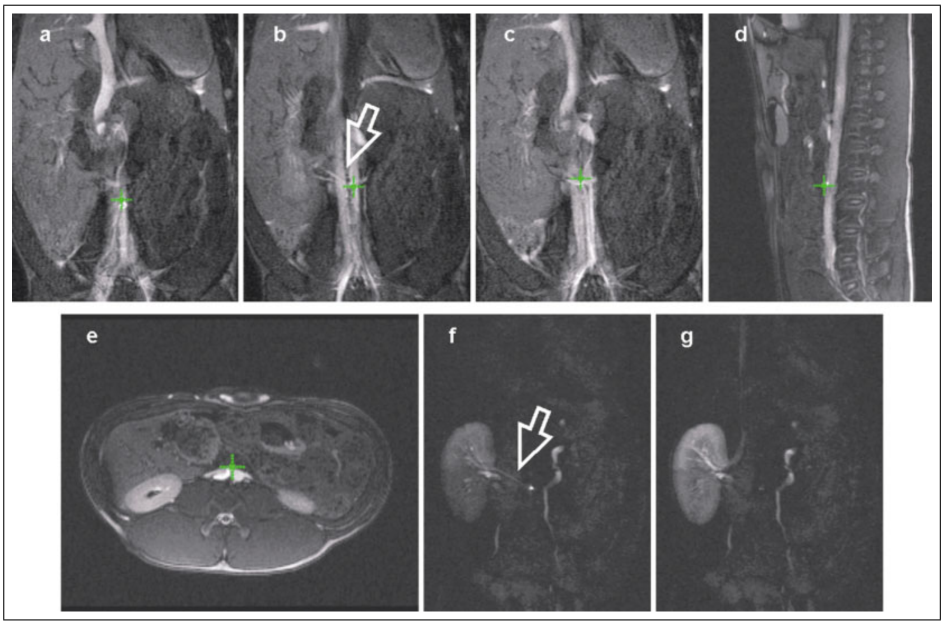

Figure 1.4 Selected images from a trueFISP time series showing the insertion of an active catheter with a single micro-coil (cross) into the right renal artery of a pig (a-e) [45].

While passive devices eliminate the RF safety concern because they do not incorporate long conductive metal wires or braiding, they have some important disadvantages. The disadvantages of passively-visualized devices include poor contrast that is further dependent on the device orientation relative to the main magnetic field (Bo) [43] and artifacts [39] that interfere with anatomic imaging.

1.4.2 Active Devices

Active visualization is based on small receive coils and antennas that are incorporated into the instrument. The signal received by coils and antennas are transmitted to the scanner and used for device tracking or visualization. A special sequence for device tracking locates the device position in MRI space and then the location is highlighted with a marker in anatomical images [44, 45, 46], Figure 1.4.

Semi-active devices employ inductively-coupled resonant coils at the tip or on the shaft [47, 48]. The received signal by the resonant coil is coupled with another coil outside the body and transmitted to the scanner for signal processing. Optical

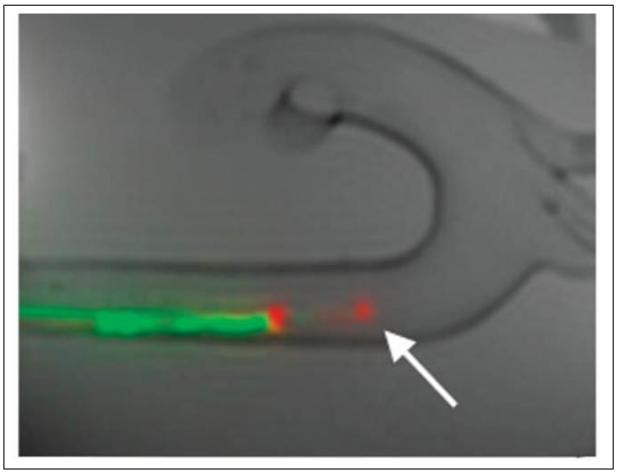

Figure 1.5 The long solenoid coil creates bright dots (red) at each end and the shaft is reconstructed from signal received by loopless antenna channel (green) [54].

tune/detune technics can improve device safety by eliminating the transmission line and detuning the resonant coil during the RF transmission [49, 50].

Active devices incorporating loopless antenna designs tuned to Larmour frequency detect the MR signal from the surrounding tissue. Embedded receive antennas are connected to an MRI scanner via a coaxial cable. The signal is amplified with a pre-amplifier to improve the SNR. A uniform shaft signal was obtained using a loopless design, but poor tip visibility impeded the safe use of the guidewire [51]. The tip signal was improved by using taper insulation at the distal end of the guidewire [52], but the distinct tip signal was an issue in this design. To improve tip visibility, a coiled copper wire was introduced at the distal tip of the device [53]. Another solution combined a loopless antenna with a solenoid coil at the tip in a single guidewire [54], Figure 1.5.

The challenge of incorporating electronic components into a guidewire and catheter while maintaining the mechanical integrity of the guidewire and RF induced heating due to E-field coupling are the limiting factors in active visualization. Table 1.1, summarizes the different device visualization strategies [55, 56, 57, 58, 59, 60, 61].

1.5 MR Safety

The MR imaging modality is not considered to be harmful to patients. This is true if the regulations and limitations are followed carefully. In contrast to X-rays, MRI is risk free of ionized radiation exposure to patients and operators. However, there are three electromagnetic fields used to obtain an MR image that may be harmful in some instances. The first one is the static magnetic field (B_0), a strong magnetic field that may attract ferromagnetic objects. B_0 can exert tremendous force on objects and attract them into the bore [64]. Therefore non-magnetic objects should not be introduced into MR scanner rooms, and before entering those rooms, people should be checked to prevent accidents.

The second field is gradient field (G), which is changed rapidly for slice selection. While rapid switching can increase the scan time, nerve simulation is possible due to the high slew rate [65, 66].

A pulsed radio frequency field is used to excite the spinning nucleuses. RF pulse produces a (B_1) magnetic field perpendicular to B_0 and an electric field parallel to B_0. The E-field component of the RF pulse coupled with long conductive wires causes heating in the body [67, 68, 69, 70, 71, 72, 73]. One approach to solving the RF induced heating issue was to integrate transformers into the transmission line, with the aim of segmenting one long transmission line into sections shorter than $\lambda/2$ wavelength [74]. Another approach used by Ladd [75] was to incorporate $\lambda/4$ wavelength coaxial chokes in the design. However, while these designs enhanced the RF safety of the device, they compromised the mechanical integrity of the guidewire. An alternative approach to an embedded RF choke was floating current traps tuned to Larmour frequency to minimize shield currents [76]. Replacing conductive transmission lines with fiberoptic cable to eliminate the RF induced heating on the transmission line was yet another solution that was attempted [77, 78]. Powering the electronic on the distal end of the device and size restrictions were the limiting factors in this approach. In another solution, high resistive wires for ECG monitoring leads reduced the heating considerably [79].

The factors affecting the RF heating of long conductive wires were wire diameter, insulation thickness, insulation permittivity, surrounding tissue connectivity [80], wire length, insertion length, wire position in the phantom, and phantom size [81]. These factors were tested using bare and insulated silver-plated copper wires in the phantom and method-of-moments-based EM field solver. In this study, it should be emphasized that the phantom and wire had a simple design and uniform material characteristics. As a result, the experimental findings were consistent with the simulation results. As noted by Bassen [82], simulations can be cumbersome when the design is complicated. Van den Bosch et. al. [83] investigated the relationship between the temperature increase at the tip of a straight metallic device and RF induced image artifact around the device in a phantom. The authors acquired a map of $B1+$ fields around the device and qualified the device current, which is proportional to RF heating. While this method is promising for stationary and straight conductors, it is not optimal for moving and curving devices, as $B1+$ mapping is time consuming, and device orientation is required for accurate calculations.

Zanchi et. al. [84] built an optically coupled system to monitor RF induced currents on long conductive wires. The authors of the study performed most of the testing in a custom-built 64 MHz birdcage and validated the system in a 1.5 T MRI scanner. Two optical probes were used to calculate the standing wave form on the wire. This approach is novel in terms of estimating heating without touching the guidewire in phantom testing where uniform electrical properties are present. However, standing waves and current distribution inside the body change significantly because the electrical properties of the environment change during in vivo procedures. Therefore, the system needs to be validated for the in vivo case.

An alternative temperature monitoring approach involved the use of infrared cameras [79], which can detect the heating on the surface of the phantom. However, this approach didn’t allow for the measurement of the heating of the device inserted into gel phantoms due to the limiting penetration of infrared light into the phantom. Another approach involved the use of heat-sensitive liquid crystal paint [67], which is water soluble and therefore unsuitable for aqueous gel phantoms that simulate the human body.

Reiter et. al. [85] showed the feasibility of using an irrigation system to suppress high heating on an EP catheter in a 1.5 T MRI scanner. The authors performed the heating experiment in a phantom and reduced heating by 22 °C with a 35 ml/min irrigation rate.

Table 1.1
Visualization techniques of MRI devices

Approach	**Advantages**	**Disadvantages**	**Examples**
Passive catheters visible based on intrinsic materials properties	Simple inexpensive. Can be used in combination with other approaches	Non-specific catheter image. Compatible conductive wires can heat. Must not contain ferrous braids	Gadolinium-filled balloon dilatation catheters. Non-braided angiography catheters. Polymer guidewires [40]
Active imaging catheters, incorporating MRI antenna	Highly conspicuous. Catheters can be depicted in color. Versatile imaging approaches including projection-mode	Complex expensive. Conductive wires can heat. Blurry profile compared with Xray catheters. Dipole designs have poor distal tip signal	Surgi Vision Intercept 0.030 dipole guidewire coil. Boston Scientific MRI Stilletto endomyocardial injection system
Active tracking catheters incorporating MRI antenna	Simple, inexpensive. Coils can be tracked without imaging, to increase speed, reduce heating	No real-time MRI. Catheter locations are computer-synthesize on image. Conductive wires can heat	MGH/General Electric electroanatomic mapping and MRI system [32]
Active catheters inducing susceptibility artifacts	Simple. Controlled artifacts confer specificity	No imaging. Heating of transmission lines when employed	Fiber-optic detune tracking coil [49]
Inductively-coupled devices	Requires no physical connection	Embeds electronics that might interfere with mechanical performance	Essen wireless stents [62] and catheters [48]
Magnetically-deflected devices	Harness magnetic field to steer device	May compromise imaging. May compromise mechanical capabilities	Untethered device navigation [63]

2. ACTIVE GUIDEWIRE DESIGN

2.1 Abstract

The field of interventional cardiovascular MRI is hampered by the unavailability of active guidewires that are both safe and conspicuous. Heating of conductive guidewires is difficult to predict in vivo and disruptive to measure using external probes. We describe a clinical-grade 0.035″ (0.89 mm) guidewire for MRI right and left heart catheterization at 1.5 T that has an internal probe to monitor temperature in real-time, and that has both tip and shaft visibility as well as suitable flexibility.

The design has an internal fiberoptic temperature probe, as well as a distal solenoid to enhance tip visibility on a loopless antenna. We tested different tip-solenoid configurations to balance heating and signal profiles. We tested mechanical performance in vitro and in vivo in comparison with a popular clinical nitinol guidewire.

The solenoid displaced the point of maximal heating (hot-spot) from the tip to a more proximal location where it can be measured without impairing guidewire flexion. Probe pullback allowed creation of lengthwise guidewire temperature maps that allowed rapid evaluation of design prototypes. Distal-only solenoid attachment offered the best compromise between tip visibility and heating among design candidates. When fixed at the hot spot, the internal probe consistently reflected the maximum temperature compared external probes.

Real-time temperature monitoring was performed during porcine left heart catheterization. Heating was negligible using normal operating parameters (flip angle, 45°; SAR, 1.01W/kg); the temperature increased by 4.2°C only during high RF power mode (flip angle, 90°; SAR, 3.96W/kg) and only when the guidewire was isolated from blood cooling effects by an introducer sheath. The tip flexibility and in vivo performance of the final guidewire design were similar to a popular commercial guidewire.

We integrated a fiberoptic temperature probe inside a 0.035″ MRI guidewire. Real-time monitoring helps detect deleterious heating during use, without impairing mechanical guidewire operation, and without impairing MRI visibility. We therefore need not rely on prediction to ensure safe clinical operation.

2.2 Background

Interventional cardiovascular MRI has potential as a radiation-free alternative to conventional X-ray guided catheterization, but has undergone only limited clinical investigation for lack of safe and conspicuous catheter devices [55]. A guidewire is a fundamental tool for catheter-based procedures. Engineering a safe and conspicuous MRI guidewire is especially challenging because of the combination of electrical and mechanical requirements and size constraints.

A key problem is radio frequency (RF) induced heating of guidewires that contain conductive materials [81, 86, 73, 68, 87]. The resonant length of the conductor is a main contributor to heating, but reported values at 1.5 T are inconsistent [72, 88]. Partial guidewire insertion from air into gel phantoms creates complex resonance patterns that are difficult to model. Insertion length also varies dynamically during clinical use as the operator moves the device. While detuning circuitry can mitigate inductive coupling between the guidewire and RF transmitter, capacitive coupling is more difficult to suppress. We propose a solution that allows the system or operator to recognize and respond to heating that is not suppressed by accompanying detuning circuitry.

A second problem is visibility. Commercial guidewires used in X-ray based procedures contain metal cores and radiopaque coils at the distal tip to increase fluoroscopic visibility. The interventionist needs to visualize the entire shaft and exact tip location in order to navigate vascular structures safely. Passively-visualized devices [43, 38] have poor contrast that is further dependent on the device orientation relative to the main magnetic field (B_0), and often create artifacts [39] that interfere with anatomic imaging. Actively-visualized devices incorporate receiver coils [51]. Active devices incorporating loopless antennas provide uniform shaft signal but poor tip visibility, impeding safe use. Qian and colleagues improved distal signal in a loopless guidewire by tapering distal insulation [52]. However, their approach provides indistinct tip signal. Another proposed solution combines a loopless antenna shaft with a solenoid antenna tip into a single guidewire [54] using two separate receiver channels. This approach suffers from coupling between channels and manufacturing complexity. Karmarkar and colleagues used coiled copper wire to improve tip visibility [53].

We introduce a novel active MRI guidewire design concept suitable for clinical application that balances mechanical, visualization and safety considerations. First, it incorporates a real-time temperature monitor to help ensure safe operation. Second, it provides a conspicuous tip having a unique image signature with simultaneous shaft profiling. This is achieved by combining a loopless antenna shaft with a tightly wound solenoid coil connected at the distal end. Finally, the implementation has mechanical characteristics similar to popular commercial cardiovascular guidewires.

2.3 Methods

2.3.1 Guidewire Design

The active guidewire was constructed using medical grade MRI compatible materials in an ISO class 7 cleanroom. The length was 1.28 m and diameter 0.89 mm (0.035″) for compatibility with conventional cardiovascular catheters, Figure 2.1A. The main shaft incorporated a modified loopless antenna with a tapered 0.25 mm diameter nitinol rod (Nitinol Devices and Components, Fremont, CA) serving as the inner conductor of the loopless antenna. Alongside this shaft was a hollow polyimide tube (0.28 mm outer diameter (OD) and 0.23 mm inner diameter (ID)) to accommodate a fiberoptic temperature probe. The distal end of the polyimide tube was closed using medical grade instant glue (Loctite, Rocky Hill, CT). Next, the nitinol rod and polyimide tube were insulated with thermoplastic elastomer polymer tubing (Pebax, Oscor Inc., FL) to ensure contact between polyimide tube and nitinol rod throughout

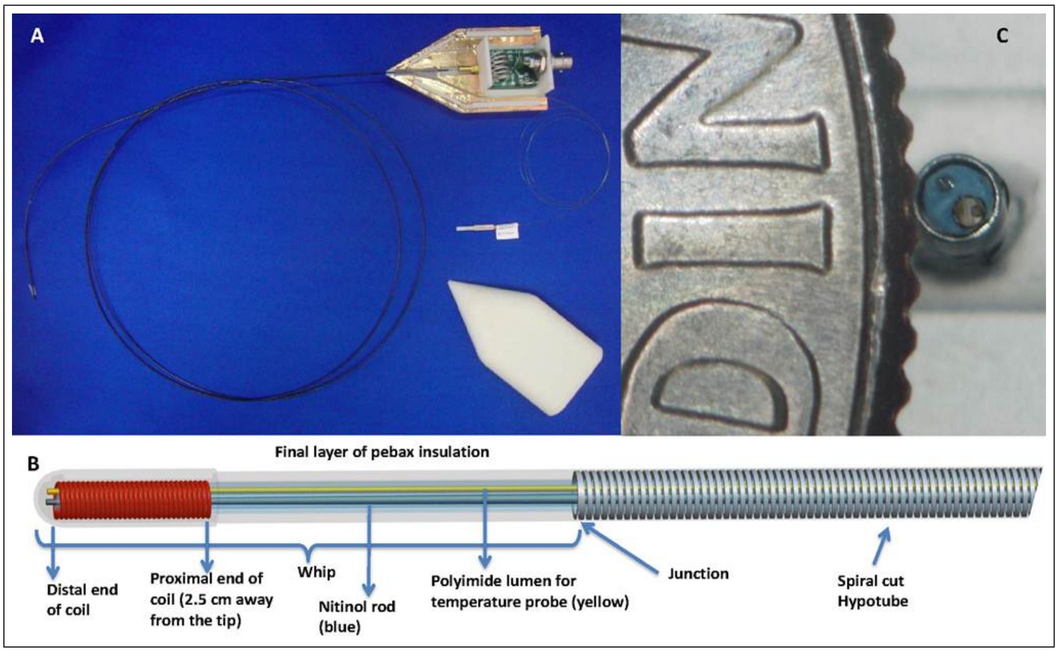

Figure 2.1 A-The 0.035″ guidewire has a modified loopless antenna with a tip solenoid, is 1.28 m long, and is connected to tune/match circuitry with an MMCX connector. A shielded box houses the circuitry and fiberoptic probe. B- The schematic depicts a 2.5 cm long tightly wound solenoid coil, a tapered nitinol rod, a polyimide lumen for the temperature probe, a spiral-cut nitinol hypotube for flexibility, Pebax insulation (blue) between the rod/polyimide assembly and hypotube, and a final outer layer of insulation (transparent). C- Cross-section view of the shaft.

the shaft. The sub-assembly was then inserted into a larger nitinol hypotube (0.81 mm OD , 0.66 mm ID) having a custom spiral-laser-cut pattern at the distal end to provide a smooth mechanical transition between the stiffer proximal shaft and softer distal shaft, as expected by physicians in a high performance clinical guidewire. The nitinol rod extended 12.5 cm beyond the nitinol hypotube to form a loopless antenna whip. A tightly wound copper solenoid coil (0.71 mm OD, 0.1 mm winding pitch, 25 mm long) was placed over the distal portion of the nitinol rod to manipulate current distribution on the whip. One end of the coil was electrically attached to the distal tip of the nitinol rod, and the other end was free. In effect, the whip of the loopless antenna was extended and coiled on itself. The whole guidewire assembly was insulated with a biocompatible final Pebax layer, Figure 2.1B. The proximal end of the guidewire connected via an MMCX type connector (Huber - Suhner, Switzerland) to matching and detuning electronics and thereafter to the MRI scanner receiver system. The active guidewire design, including the solenoid tip, was tuned to 63.67 MHz and matched to 50 ohms using a tune/match circuit connected to the guidewire at the proximal hub.

A PIN diode is activated during the RF excitation to detune the receive antenna by creating high impedance at the antenna junction where the nitinol rod extends beyond the hypotube.

2.3.2 Balancing Heating and Tip Visibility

Other investigators have characterized parameters affecting RF induced heating of medical devices, including length, diameter, and insulation thickness [86, 67, 89]. In this study, we focused on the heating implications of our enhanced-conspicuity distal tip.

First, we explored the attachment configuration of the solenoid coil to the distal end of nitinol rod. 25 mm long solenoid coils (0.71 mm OD, 0.61 mm ID) were soldered to the nitinol rods using a soldering alloy (Indium Corp., Utica, US). We considered four different solder attachment configurations of the solenoid to the rod: either the (1) distal or (2) proximal end of the solenoid attached leaving the other end unattached; (3) both ends attached; or (4) neither end attached. Unattached ends were suspended by insulation. We tested heating and imaging for each configuration. Next, we explored the impact of solenoid length and diameter. The inductance of a solenoid coil is known to depend on length, cross-sectional area and the number of turns per unit area, each of which impacts signal and heating performance. We tested solenoid lengths from 10 to 50 mm and solenoid outer diameters from 0.61 to 0.81 mm to assess signal strength and RF heating. The MR signal detected using candidate configurations was tested in a 20 x 15 x 10 cm water phantom. MRI at 1.5 T (Espree, Siemens, Erlangen, Germany) used a 3D balanced steady state free precession (bSSFP) sequence and the following typical parameters: repetition time (TR)/echo time (TE), 872.63/2.04 ms; flip angle, 45 °; slice thickness, 1 mm; field of view, 340x340 mm; matrix, 192x144. The ratio of the maximum tip signal to maximum shaft signal was calculated from regions of interest drawn on maximum intensity projection images.

2.3.3 Comparison of Internal and External Fiber-Optic Temperature Probes and In Vitro Heating Measurements

The guidewire incorporated a dedicated polyimide port for an internal 0.15 mm diameter fiberoptic temperature probe (OpSens, Quebec, Canada). The temperature measurement system has 0.3 °C system accuracy. The polyimide distal tip was sealed using acrylic glue (Loctite, Rocky Hill, CT). We also sought to establish this internal probe always reflected equal or higher values than temperature at the guidewire surface in contact with the patient. Therefore, we temporarily affixed an external polyimide tube (0.28 mm OD and 0.23 mm ID) to the surface of the guidewire using polyester heat shrink tubing (Advanced Polymers, Salem, NH), to accommodate a second moveable external temperature probe. The fiberoptic temperature probe first was advanced maximally into the polyimide tube. Temperature was recorded for 30 seconds before and after MRI begins, and then both internal and external fiberoptic probes were withdrawn manually to obtain a longitudinal heating profile. Locations of heating maxima were identified and compared for both inner and outer sensors. Once the hottest spot was located, the internal temperature probe was fixed to that location for further investigation. In vitro RF induced heating tests were performed in an acrylic phantom prepared according to the ASTM 2182 standard. Guidewires were aligned parallel to the main magnetic field and fixed in position at an insertion length of 35 cm, a horizontal offset of 12.7 cm lateral to the iso-center, and a vertical offset of 6 cm from the bottom of the phantom. The heating distribution of implants inside the ASTM phantom corresponds almost exactly to the phantom's electrical field distribution, which increases away from scanner iso-center. Therefore, we tested the guidewire temperature at many different positions: insertion lengths 15 cm, 30 cm, 45 cm and 60 cm; depths 2 cm, 4 cm and 6 cm from the bottom; horizontal offsets 12.7 cm, 7.6 cm, 5.1 cm laterally left and right from iso-center; and at iso-center. We used the following sequence parameters for heating experiments: bSSFP; TR/TE, 3.23/1.62 ms; flip angle, 45 °; slice thickness, 6 mm; field of view, 340x340 mm; matrix, 192x144; scanner reported SAR, 1.52 W/kg. For each map position, a 30 second baseline temperature recording was followed by a one minute scan, and maximum after one minute was subtracted from the baseline average.

2.3.4 In Vivo Experiments

Experiments were approved by the institutional animal care and use committee and followed contemporary NIH guidelines. Two naive Yorkshire swine (weight range 51-64 kg) underwent general anesthesia and transfemoral artery access using a 7 Fr x 12 cm (14 cm including the hub) introducer sheath (Fast-Cath, St. Jude, Minnesota). Both the inner and outer temperature probes were fixed at the longitudinal hot spot identified during phantom experiments. After a 30 second baseline measurement, temperature was recorded in real time as guidewires were advanced or withdrawn manually, from the iliac artery to the aortic arch, during bSSFP MRI with TR/TE, 3.23/1.62 ms; flip angle, 45 °; scanner reported SAR, 1.01 W/kg. To increase the dynamic range of heating beyond clinical use conditions, and to better assess the relationship between inner to outer temperature measurements, the experiment was repeated with TR/TE, 3.23/1.62 ms; flip angle, 45 °; scanner-reported SAR value, 3.96 W/kg. A worst-case insertion length was identified, and RF induced heating was measured during a one minute scan without moving the guidewire.

2.3.5 Mechanical Properties

The whip flexibility of the final device was compared to a commercial 0.035″ nitinol guidewire (Glidewire 035, Terumo, Tokyo, Japan). To assess the flexibility of the distal 12.5 cm whip, we measured the deflection force required to achieve a range of deflection angles on a fulcrum located 1 cm, 3 cm, or 5 cm from the tip using a load cell (IDTE, Machine Solutions, Arizona).

2.4 Results

2.4.1 Balancing Heating and Tip Conspicuity

Figure 2.2 and Table 2.1 show the signal profile of several candidate guidewire designs, comparing different solenoid solder configurations. A distal solenoid solder point assured a conspicuous tip signal, even if combined with a second proximal solder point. A distal-only solder point provided a maximal tip/shaft signal intensity ratio, reduced by half by soldering both the distal and proximal ends of coil, and abolished in other configurations. The distal-only design also had an image signature that best distinguished the tip from the shaft, having a signal null separating the shaft profile and the tip point (Figure 2.2A). Solder locations also impacted the position and intensity of maximum heating spot along the shaft. The highest heating was found when the solenoid was soldered proximally, less when soldered distally, still less with combined proximal and distal soldering and least when the solenoid was not soldered to the inner rod. The location of heating was spatially distributed near or between solder points. Overall, we found the best balance of distal-tip conspicuity and heating in the distal solder-point configuration.

Table 2.1

Relative signal and heating performance among guidewire designs. The four rows indicate four different solder configurations of the distal solenoid: distal, proximal, both, or free-floating. For each design, the table indicates the relative signal of the tip compared with the shaft; the maximum temperature increase normalized to the worst-case design; and the location of the point of maximum heating.

Solder Attachment Configuration	Tip/ Shaft Signal	Max. Heating Ratio	Max. Heated Point
Distal	0.97	0.63	2.5 cm away from tip
Proximal	0.12	1	2.5 cm away from tip
Distal and Proximal	0.52	0.32	1 cm away from tip
Not Connected	No tip signal	0.10	Junction, 12.5 cm from tip

Next, we empirically tested different solenoid lengths (10 to 50 mm) and diameters (0.61 to 0.81 mm) to optimize the tip signal strength and heating with the distal

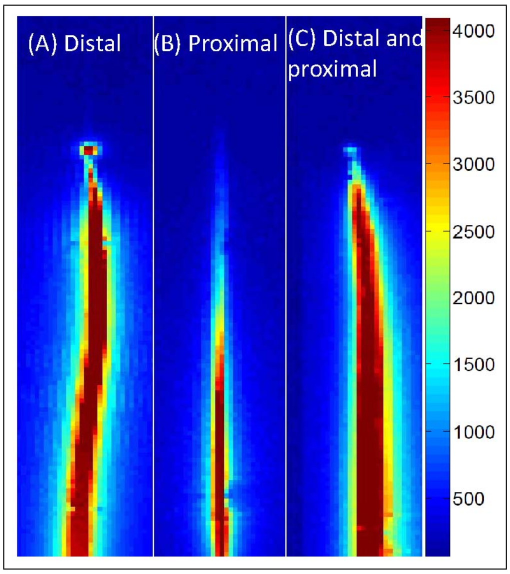

Figure 2.2 Three different soldering configurations of the distal guidewire solenoid. A tight-pitch solenoid coil (25 mm long, 0.71 mm outer diameter) is electrically connected (A) at the distal end only, (B) at the proximal end only, and (C) at both ends. The distal-only attachment creates a unique tip signal profile with a null separating it from the shaft.

connection. Table 2.2 shows tip signal normalized to shaft signal, also depicted in Figure 2.3. Table 2.3 shows maximum heating of prototypes normalized to maximum heated one. Overall we found the most attractive solenoid configuration to be 0.71 mm in diameter and 25 mm in length with inductance 745 uH for 63.67 MHz.

Table 2.2
Maximum tip to shaft signal intensity ratio are depicted among all soldering configurations

Length / Diameter	0.61 mm	0.71 mm	0.81 mm
1 cm	0.27	0.33	0.55
2.5 cm	0.53	0.74	0.69
5 cm	0.38	0.40	0.65

2.4.2 Inner and Outer Temperature Probe Comparison

Figure 2.4 shows a representative temperature profile along the shaft of the guidewire, obtained by continuous probe pullback during MRI in vitro. For each guidewire prototype, we identified a hot spot within the distal solenoid.

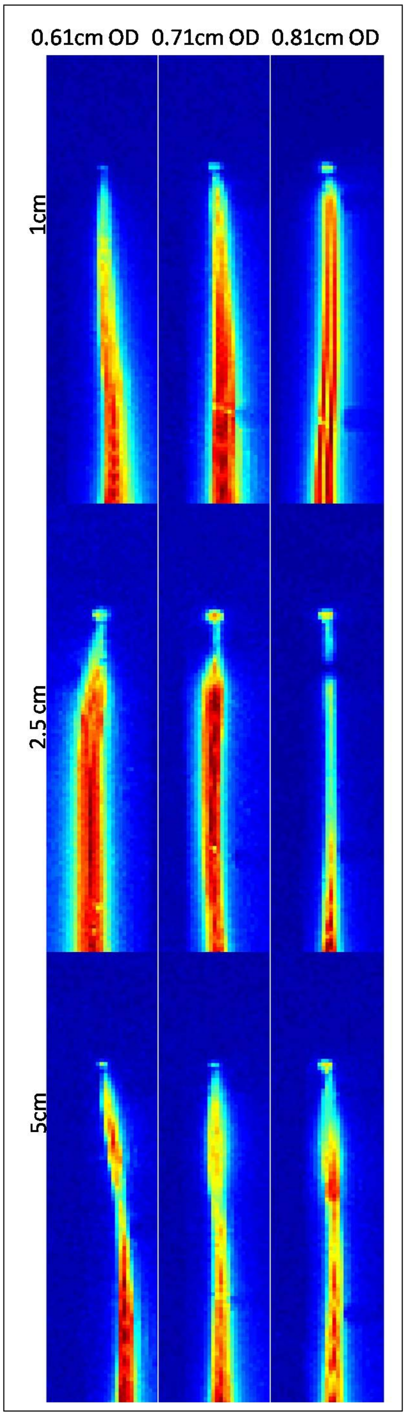

Figure 2.3 SNR maps of guidewire (distal tip solder) for 0.61 cm, 0.71 cm, 0.81 cm coil diameter and 1 cm, 2.5 cm, 5 cm coil length configurations. Increasing coil diameter results in brighter tip signal. Increasing coil length changes the shaft signal profile and tip signal intensity.

Table 2.3
Maximum heating are depicted among all soldering configurations. The heating values are normalized to the highest values achieved with the 1cm, 0.81mm design.

Length / Diameter	0.61 mm	0.71 mm	0.81 mm
1 cm	0.27	0.26	1
2.5 cm	0.55	0.59	0.25
5 cm	0.15	0.16	0.22

The inner temperature was consistently higher than the outer temperature measurement, which indicates that it can adequately represent potential heating hazard. The ratio of maximum outer to inner temperature is 0.81 ± 0.06.

The heating map of ASTM phantom was calculated by linearly interpolating sparsely acquired heating data, Figure 2.5. Temperature increase at the hot spot after a one minute scan was below 4 °C for guidewire configurations close to the center of the phantom where the E-field magnitude is minimal. However, the temperature increase reached 18 °C when the guidewire was placed at the edge of the phantom where the E-field is large.

2.4.3 In Vivo Imaging and Heating

No detectable *in vivo* temperature increase was observed during MRI using a 45 ° flip angle; rather, a flip angle of 90 ° was required clearly to detect a temperature increase. Figure 2.6 shows a representative temperature recording during manual guidewire pullback (with the temperature probe fixed at the hot spot), from the aortic arch to the iliac introducer sheath. The maximum temperature increase was observed at an insertion length of 14 cm, at which point the tip of the guidewire was just inside the tip of the sheath. In this condition, the hot spot remained 25 mm inside the sheath and was isolated from cooling blood flow. Pulling the guidewire further from 14 cm to the hub of the sheath caused a sudden temperature drop due to the temperature gradient inside the sheath, where the temperature approaches room temperature (22 °C)

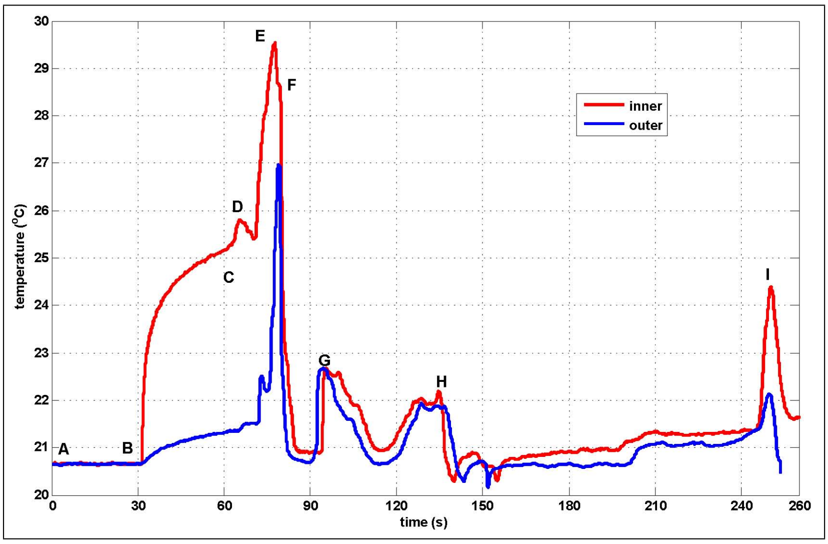

Figure 2.4 Temperature distribution on guidewire during MR scan. A heating profile is obtained by moving temperature sensors within (red) and on the surface of (blue) the guidewire. The probes begin beyond the guidewire distal tip. Segment A-B indicates a 30 second baseline recording; MRI begins at B; a relative steady-state is achieved at C, when probe pullback begins. Temperature peaks correspond to physical landmarks including: D, the distal end of the solenoid coil; E, the guidewire hot-spot; F, the proximal end of the solenoid coil; G, the inner rod-hypotube junction point; H, gel phantom entry point; H-I, air; I, hypotube-MMCX connector solder point.

near the hub. Figure 2.7 shows inner and outer temperature measurements on the guidewire at the worst-case insertion length of 14 cm and flip angle, 90 °; SAR, 3.96 W/kg, during a one minute scan. At baseline, the average inner and outer temperatures from the two animal experiments were $36.2 \pm 1.2\,^{\circ}$C and $35.7 \pm 1.5\,^{\circ}$C, respectively. At the worst-case insertion length, the temperature increased by $4.2 \pm 0.3\,^{\circ}$C (inner) and $3.4 \pm 0.2\,^{\circ}$C (outer) after one minute scans at the hot spot. The ratio of outer to inner temperature was 0.80 ± 0.03. With further advancement of the wire beyond the tip of the sheath, the temperature fell rapidly and remained within a maximum of $0.7 \pm 0.1\,^{\circ}$C over baseline, measured at the inner probe. Figure 2.8 shows real-time MRI of the guidewire inside a pig aorta. It is attached to a separate receiver channel and reconstructed in green. The guidewire tip appears as a distinct green point, and the guidewire shaft has a uniform signal distribution.

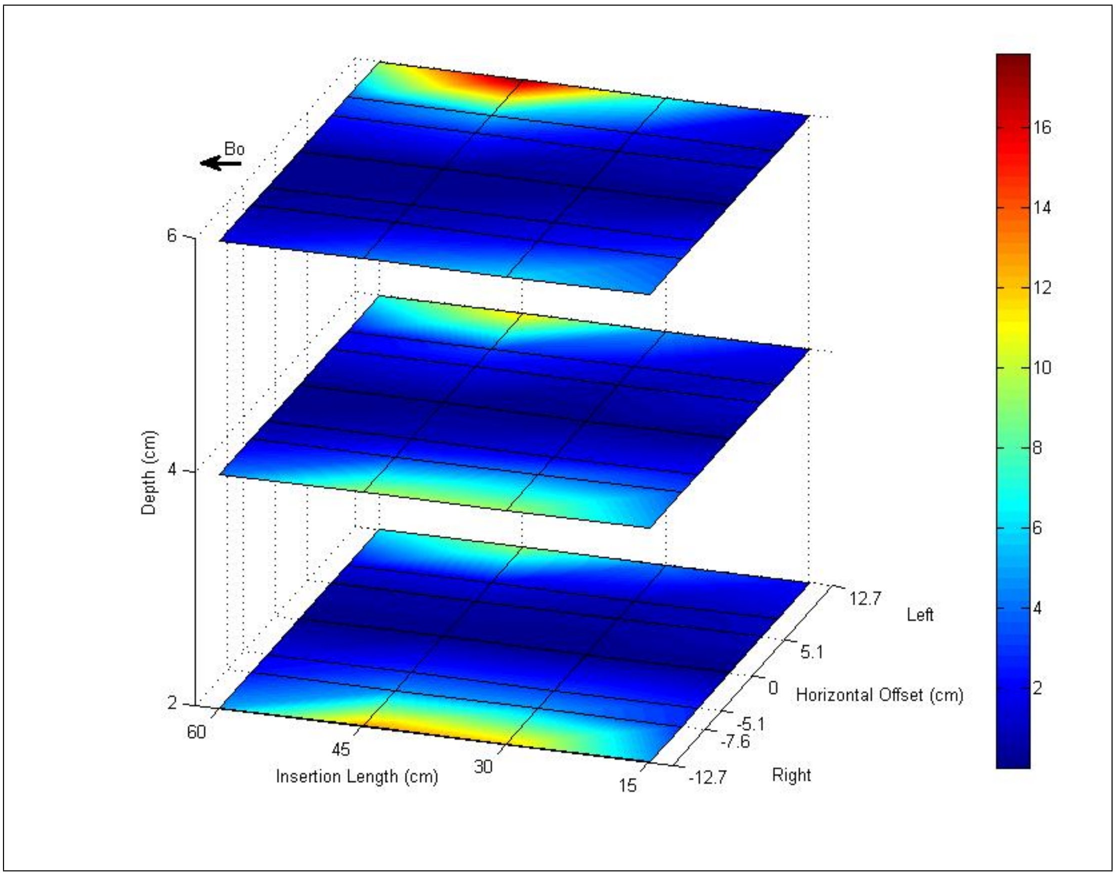

Figure 2.5 Heating distribution map of ASTM F2182 phantom. The heating distribution of the guidewire in the ASTM F2182 phantom agrees with previously reported E-field distributions in the ASTM phantom. Significant heating (18 °C) is observed when the guidewire is inserted into high E-fields.

Figure 2.6 A representative in vivo temperature recording during manual pullback. The flip angle is increased to 90 °; SAR, 3.96 W/kg to exaggerate heating. A temperature baseline is obtained before scanning begins. Scanning generates a small temperature rise. After a further interval, the guidewire is withdrawn from the aortic arch during bSSFP MRI. Noteworthy heating was observed just as the guidewire tip entered the tip of the vascular introducer sheath at an insertion length of 14 cm.

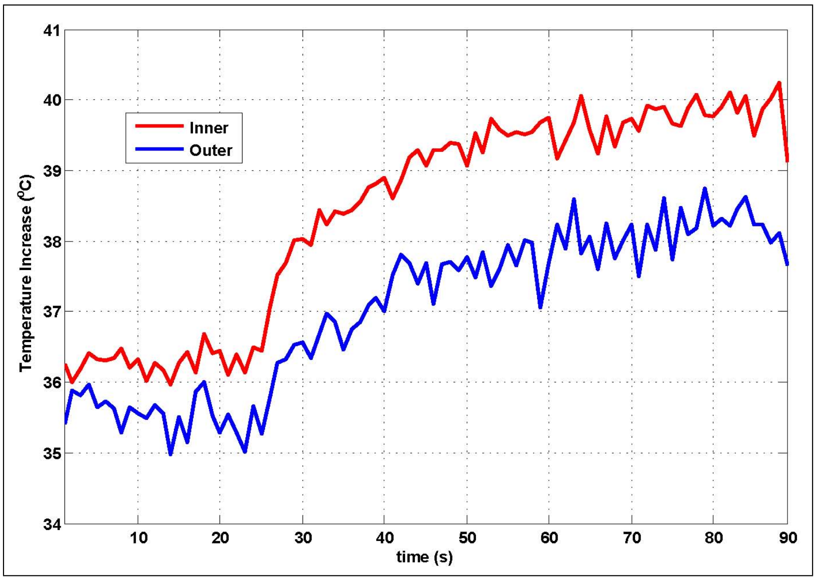

Figure 2.7 In vivo heating measurement. Inner (red) and outer (blue) temperature measurements of the hot spot at the worst-case (14 cm) insertion length, at which the guidewire remained inside the introducer sheath, using a 90 ° flip angle, SAR, 3.96 W/kg.

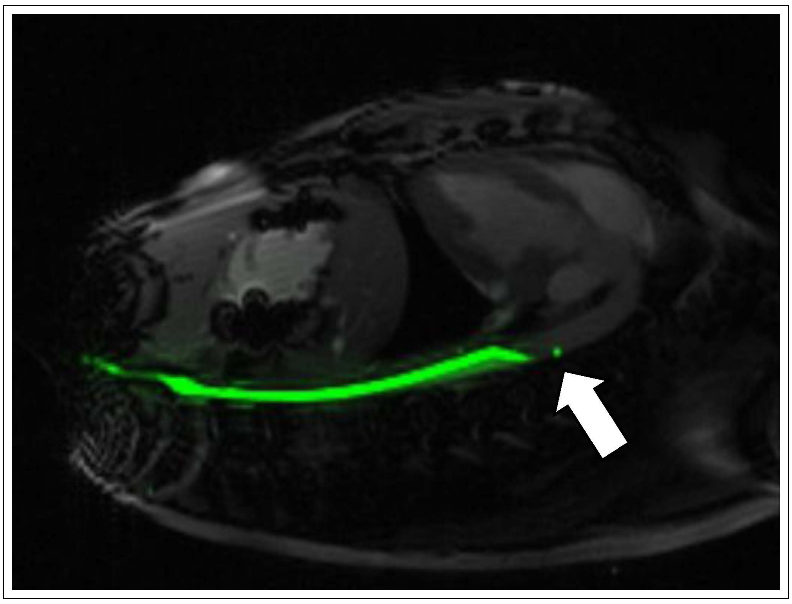

Figure 2.8 In vivo image of guidewire in aorta of swine. Guidewire has a conspicuous signal at the tip (white arrow).

2.4.4 Mechanical Properties

Figure 2.9 shows the results of tip flexibility testing. The distal 5 cm of the active guidewire has comparable flexibility to the commercial comparator PTFE-coated nitinol guidewire (Glidewire 035, Terumo, Somerset, NJ).

2.5 Discussion

We describe the integration of a fiberoptic temperature probe inside a compact and conspicuous guidewire that is mechanically suitable for invasive and interventional cardiovascular MRI procedures. The probe provides continuous monitoring to allow rapid detection of deleterious device heating during use, without impairing mechanical guidewire operation, and without impairing MRI visibility. Indeed the embedded fiberoptic probe, operated in pullback mode, also allowed rapid empirical testing of guidewire designs to balance heating and conspicuity. Using this real-time temperature monitoring system we developed a family of guidewire designs that have a single heating maximum along their length, typically near the tip, and consistently higher

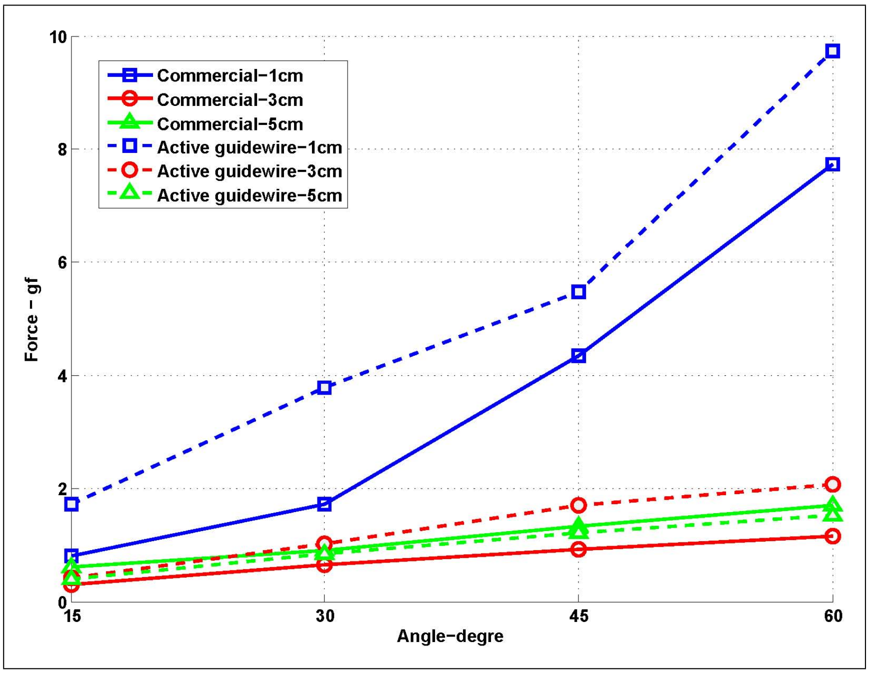

Figure 2.9 Tip flexibility results of commercial comparator (Terumo Glidewire 035) and the active guidewire. The active guidewire has similar flexibility characteristics to the commercial comparator. The force required to deflect the active guidewire is slightly higher than the force required to deflect the commercial guidewire.

internal than external temperature. We consider this as a significant advance in interventional cardiovascular MRI because we no longer need to rely on models of dubious predictive value to ensure safe clinical operation. Moreover, in the future we can modulate the input energy during MRI excitation based on temperature probe feedback.

Multi-channel RF coils with separate transmission lines have been used in many MRI compatible interventional devices to visualize separate components of the instruments. In this study we eliminated separate transmission lines and electrically attached one end of a solenoid coil directly to the inner conductor of a loopless antenna base to manipulate current distribution on the whip. Electrical attachment of the coil to the inner rod provided a distinct signal at the tip. The location of the solenoid attachment point impacted both device signal profile and heating. We found a balance of the two when we soldered the distal end of the solenoid to the inner rod. In this configuration, the hot spot was 2.5 cm proximal from the tip of the guidewire. During real-time temperature monitoring, the temperature probe is fixed at this hot spot. In the future, this will allow us to create different guidewire prototypes with curved tips or J tips, without impairing mechanical properties of the guidewire.

Assessment of RF-induced heating of medical devices typically is performed in gel phantoms using multiple fiberoptic temperature probes affixed at locations expected to have significant heating. Electromagnetic simulations can help identify candidate locations, but are not readily applied to more complex mechanical designs. We therefore introduced a fiberoptic temperature probe intended to operate during actual use conditions, and designed a guidewire incorporating a lumen specifically for temperature monitoring. Recordings during probe pullback allow rapid whole-device assessment, and efficient comparison of designs. In our experiments, we waited only 30 seconds before each pullback, which approached but did not achieve thermal equilibrium, but which was adequate to identify important heating points (Figure 2.4, point E). Alternative temperature monitoring approaches include infrared cameras [79], which do not detect this range of heating in gel phantoms or in vivo, and heat-sensitive liquid crystal paint [67], which is water soluble and therefore unsuitable for aqueous gel phantoms that attempt to load the RF excitation coils.

While we are able to detect a temperature rise when testing the guidewire in an industry standard gel phantom, the heat evidently is dissipated during normal operation (flip angle, 45 °; SAR, 1.01 W/kg) in vivo when exposed to flowing blood during left heart catheterization in pigs. Indeed, we were able to detect a temperature rise (4.2 °C) in vivo only by increasing the RF transmit power beyond expected operating conditions (flip angle 90 °; SAR 3.96, W/kg), and only when the hotspot was isolated from flowing blood inside the vascular introducer sheath. In general, vascular catheterization imposes favorable geometric constraints by confining the devices to relatively central body structures where the E-field magnitude is low. However, the temperature monitor provides a desirable and incremental margin of safety that can allow the operator or system to respond to unanticipated heating caused, for example, by unusual positioning or by device malfunction.

Finally, to suit the target application of MRI heart catheterization, we were able to manufacture a device with these additional features while retaining comparable tip/whip flexibility to a popular nitinol commercial guidewire. This was possible by employing several advanced material processing and manufacturing techniques including reduced stiffness Pebax coating, a flexible solenoid coil, a tapered nitinol rod, a spiral laser-cut nitinol hypotube, and a thin fiberoptic cable.

2.6 Conclusion

We designed an active guidewire with distinct tip signal, uniform shaft signal and embedded fiberoptic temperature probe fixed to shifted hot-spot location to monitor RF induced heating in real time without affecting the device functionality adversely. The embedded temperature monitoring system provides real time heating information to ensure safe operation while guidewire orientation and trajectory are dynamically changed within the vasculature.

3. SAFETY AND EFFECTIVENESS OF THE ACTIVE GUIDEWIRE: BENCH-TOP TESTS

In the previous chapter, an MRI active guidewire and a novel temperature measurement technique for acquiring a heating profile of the guidewire were introduced. In addition, mechanical, visualization and safety concerns were also briefly discussed. However, in order to have a clinical grade MRI active guidewire, the safety and effectiveness of the guidewire need to be comprehensively evaluated. Therefore, in this chapter, safety and effectiveness issues related to the guidewire were addressed. First, it was necessary to identify and ensure that the mechanical requirements of the guidewire were met. Next, the SNR of the guidewire was calculated and the image artifacts were measured. An extensive RF heating evaluation was performed in phantom experiments. Finally, a solution to ensure the electrical safety of the guidewire was proposed. In this regard, it should be noted that previous to this study, electrical safety issues were often not addressed by researchers studying active devices for MRI.

3.1 Mechanical Design and Tests

MRI active guidewires should meet the mechanical requirements for safe and effective intravascular procedures under MRI. During a right/left heart catheterization, the guidewire was advanced through a curvature vascular structure. To navigate the guidewire through narrow vessels, the guidewire should transmit the applied force and torque from the proximal end to the distal tip. The guidewire also should support the catheter and allow for the catheter to be inserted into the target tissue; therefore, a stiff shaft is required. In addition, the guidewire needs to have a soft tip in order not to damage or perforate vessels. Considering all these requirements the developing a guidewire requires a complex and unique design. In addition to the mechanical properties mentioned in Chapter 2, a curved tip was constructed to prevent vessel perforation. The distal part of the guidewire was angled at 1.5 cm from tip to create a 30° curve tip, Figure 3.1. In addition, a nitinol rod was tapered from $0.014''$ to $0.003''$

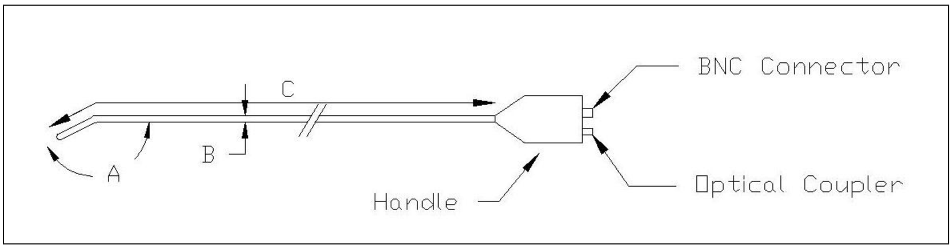

Figure 3.1 Schematic of guidewire. A, 1.5 cm 30 ° J curve tip; B, 0.035″ diameter; C, 128.5 cm long active guidewire.

at the whip to improve the tip flexibility.

Mechanical characteristic of the active guidewire was tested by comparing them with commercial counterparts. The following sections explains the test setups and results obtained.

3.1.1 Tip Flexibility Test

The aim of this test is to evaluate the force necessary to deflect the distal tip of the guidewire. The Interventional Device Testing Equipment (IDTE) 2000 (Machine Solutions Inc.) was prepared with an auxiliary force meter, an angle guide, a securing bolt, and an alignment fixture (Figure 3.2). The guidewire was tested by advancing the guidewire through the alignment fixture and securing bolt, and stabilizing the tip in the force meter. The angled tip was positioned such that the tip pointed in the direction of deflection. The distance between the securing bolt and force meter was adjusted to 5, 10, and 20 mm, and the force required to deflect the tip to 45 ° and 80 ° (the maximum deflection possible on the equipment) at each distance was measured. The process was repeated for 5 active Guidewires and 5 Terumo Glidewires. One each of 3 additional comparator devices was tested to provide a better idea of the range of acceptable flexibility performance.

Results are reported in Table 3.1 and Table 3.2.

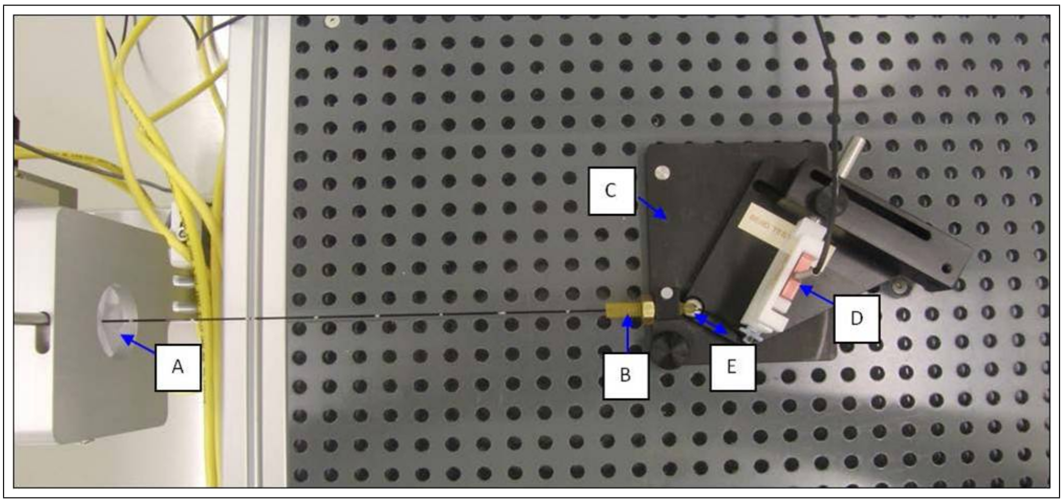

Figure 3.2 Test equipment set-up. (A) alignment fixture, (B) securing bolt, (C) angle guide with pre-marked 45 ° and 80 ° deflection points, (D) auxiliary force meter, (E) adjustable distance between bolt and guidewire tip.

Table 3.1
Force required to deflect the guidewire tip 45 ° when the guidewire is secured 5, 10, and 20 mm from the tip. Average (± standard deviation) force is given from 5 samples each of the active guidewire and the Terumo Glidewire. Units are gram-force.

Distance from guidewire tip	Active Guidewire	Terumo Glidewire
5 mm	3.52 (± 0.47)	3.45 (± 1.73)
10 mm	2.45 (± 0.43)	1.88 (± 0.34)
20 mm	1.22 (± 0.22)	1.74 (± 0.51)

Testing demonstrates that the active guidewire tip flexibility similar to the comparator device in all conditions.

3.1.2 Distal Tip Stiffness Test

Distal tip stiffness was evaluated by advancing the tip of the guidewire against a fixed load cell and measuring the resultant reaction force. The guidewire was placed in the IDTE2000 roller assembly and threaded through plastic tubing until the distal tip was flush against the distal load cell (Figure 3.3). The guidewire was then advanced using the roller assembly at a speed of 10 cm/min until the proximal end was advanced

Table 3.2
Force required to deflect the guidewire tip 80° when the guidewire is secured 5, 10, and 20 mm from the tip. Average (± standard deviation) force is given from 5 samples each of the active guidewire and the Terumo Glidewire. Units are gram-force.

Distance from guidewire tip	Active Guidewire	Terumo Glidewire
5 mm	7.23 (± 1.27)	12.57 (± 3.21)
10 mm	5.39 (± 0.85)	7.43 (± 1.94)
20 mm	2.61 (± 0.46)	3.30 (± 0.84)

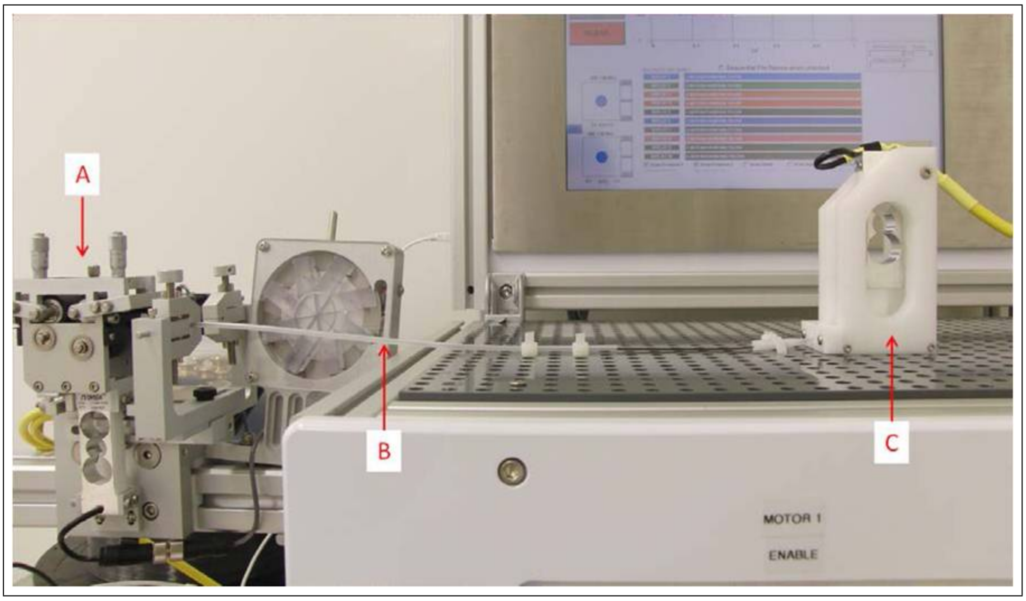

Figure 3.3 Distal tip stiffness set-up, showing the proximal end of the guidewire advanced at 10 cm/min using the roller assembly (A) through plastic tubing (B) such that the tip is pushed against a distal load cell (C).

3 cm. Force was recorded at the load cell throughout the experiment. 5 of active guidewire and 5 of Terumo Glidewire were used in the experiments.

The average (± standard deviation) maximum force at the distal tip was 12.89 ± 0.91 gf for the active guidewire and 22.90 ± 1.55 gf for the Terumo Glidewire. The average (± standard deviation) pushing force at the proximal end was 18.89 ± 3.50 gf for the active guidewire and 33.13 ± 2.06 gf for the Terumo Glidewire. Results show that the active guidewire has softer distal whip compare to Terumo Glidewire.

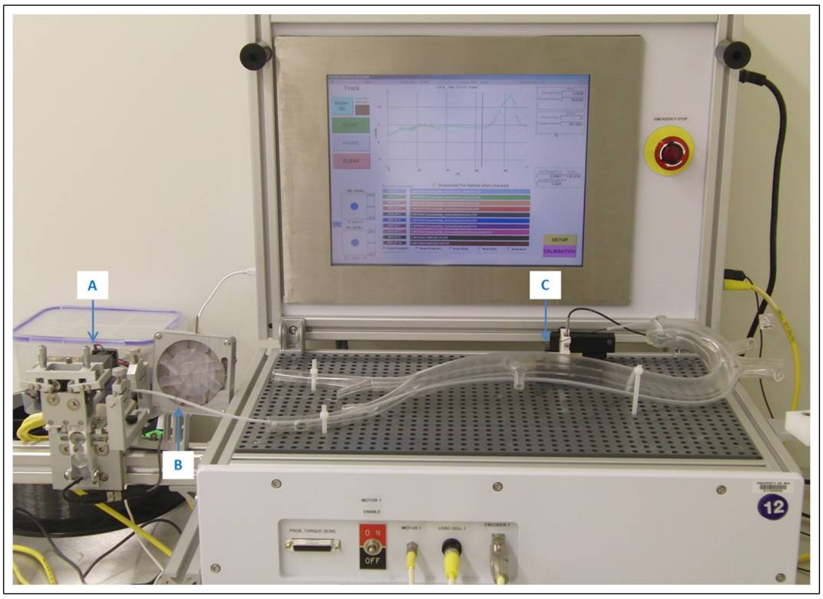

Figure 3.4 Test set-up for pushability, showing the anatomical model with plastic tubing delineating the guidewire track. The guidewire is advanced from the proximal end using a roller assembly (A). The guidewire tip starts at point (B) and ends at point (C).

3.1.3 Pushability Test

The aim of this test was to evaluate the force required to advance the guidewire in the vasculature trajectory representing the clinical target which is left/right ventricle. The test set-up was prepared on the IDTE2000 machine by securing an anatomic model to the peg board with cable ties and feeding plastic tubing through the model to direct guidewire movement through a repeatable track (Figure 3.4). The proximal end of the test sample was placed in the roller assembly including a motor, a distance encoder, and a proximal load cell. From a pre-set starting position, the guidewire was advanced through the anatomic model at a speed of 100 cm/min for a total of 95 cm. Force required to advance the wire through the system was recorded at the proximal load cell. Force was recorded over the entire advancement.

The average (± standard deviation) maximum force during advancement was 25.72 ± 1.61 gf for the active guidewire and 11.42 ± 1.87 gf for the Terumo Glidewire. Due to outer hypotube stiffness, more force was required to advance the active wire to the target area.

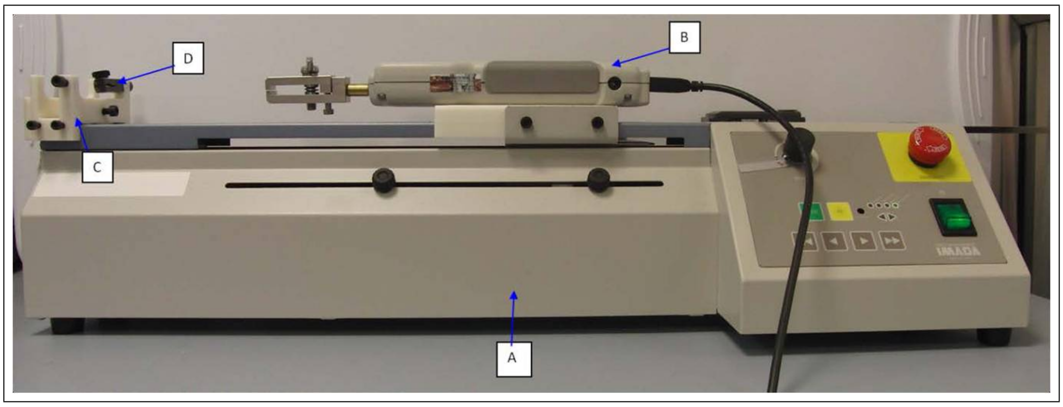

Figure 3.5 Tensile strength test set-up consisting of (A) a motorized horizontal test stand, (B) a digital force gauge, and (C) a support apparatus holding (D) a clamp.

3.1.4 Tensile Strength Test

We aimed to verify that all joints on the active guidewire are able to withstand normal tensile loading for the intended use (right/left heart catheterization). The motorized horizontal test stand (Imada, P/N MH-275S) was prepared with a digital force gauge connected to recorder software and a custom-design support holding a clamp, Figure 3.5. One end of the portion of the guidewire to be tested was clamped in the force gauge and the other end was gripped at the support. The two clamps began 15 cm apart for all test portions. A tensile force was applied at a rate of 10 mm/min in the direction of the main axis of the guidewire until the joint loosened or broke.

The following joints were tested: the distal tip strength, and the security of the guidewire handle to the guidewire shaft. The test setup was as in Figure 3.6. The average tensile load at breakages were 5.75 (± 1.12) and 41.52 (± 2.58) N for distal tip and handle-guidewire joints, respectively.

3.1.5 Torque Response Test

Aim of the test was to evaluate the amount of rotation achieved at the distal tip of the active guidewire compared to the degree of rotation applied at the proximal end of the guidewire. The guidewire was advanced through a7 Fr diagnostic catheter

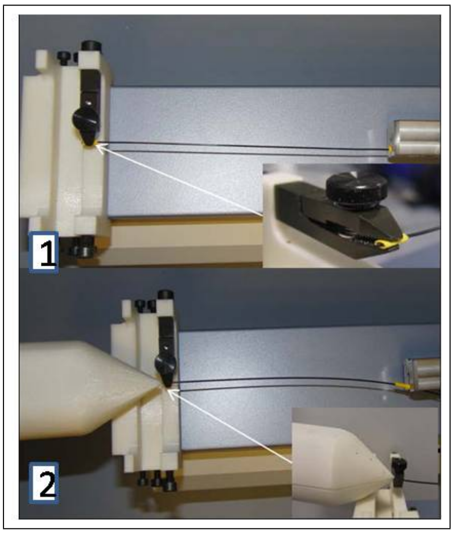

Figure 3.6 The distal tip strength (1), and the security of the guidewire handle to the guidewire shaft(2) were tested.

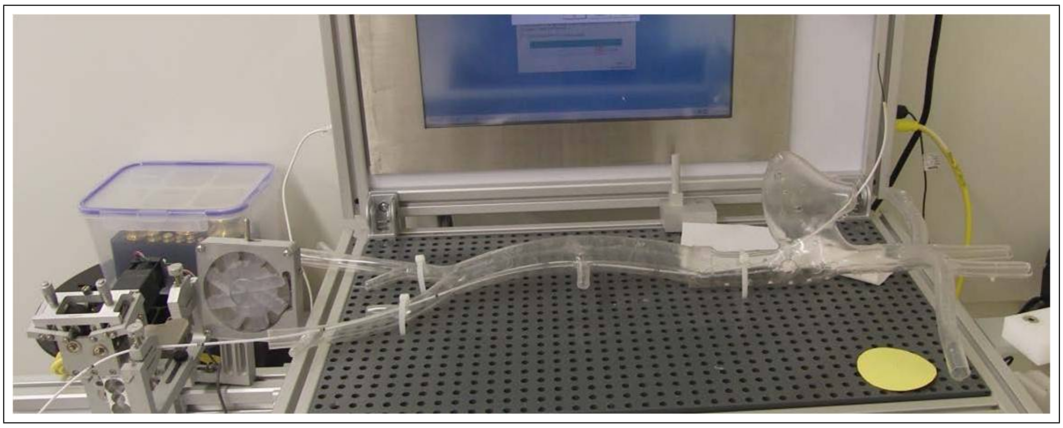

Figure 3.7 Experimental set-up, showing the diagnostic catheter and guidewire advanced through the anatomic model.

flushed with water such that the guidewire tip extended 2.5 cm beyond the catheter tip. The catheter-guidewire assembly was advanced from the left femoral vein of the anatomic model until the tip was in the location of the main pulmonary artery, Figure 3.7. Paper protractors were then attached to the proximal and distal ends of the guidewire, Figure 3.8. The proximal end was rotated counter-clockwise. The amount of proximal input rotation required to achieve distal tip rotation in 90 ° increments was recorded for a total of 5 rotations at the tip. Terumo Glidewire was used as a comparator.

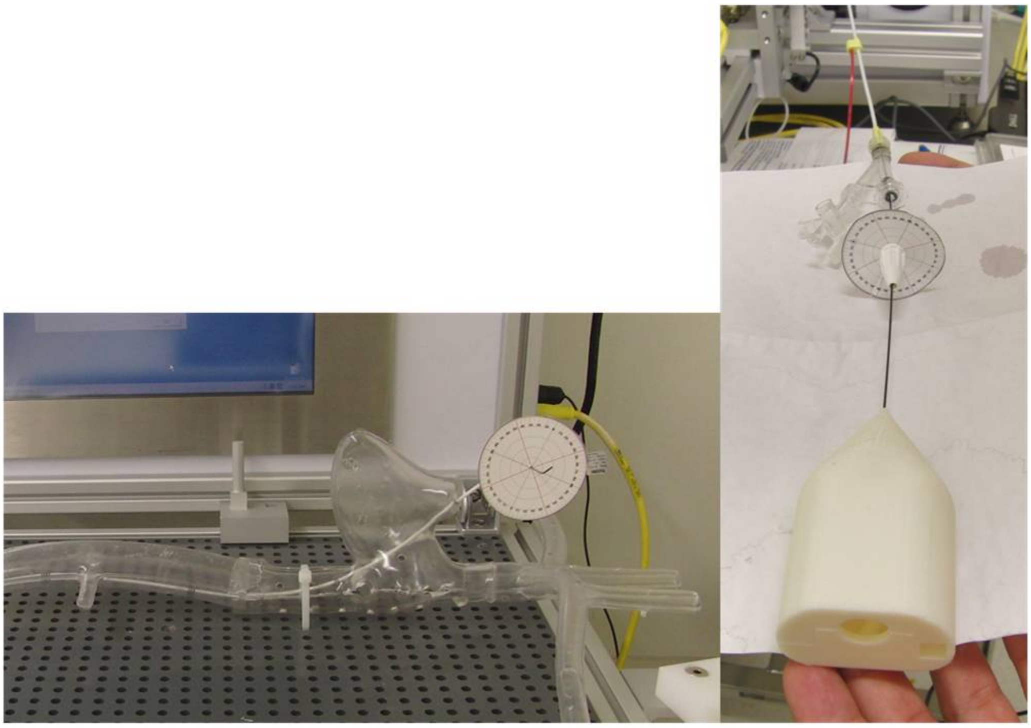

Figure 3.8 Protractors affixed to the distal tip (left) and proximal shaft (right).

Figure 3.9 shows rotation at the distal tip in 90° increments and required input at the proximal end to achieve the desired tip rotation, as a ratio of input rotation over distal tip rotation. Ratios greater than 1 indicate there was a lag between input rotation and 1:1 corresponding rotation at the tip. It was also observed that the distal tip did not always rotate continuously with proximal rotation. Rather, the proximal end would be rotated continuously while the tip remained stationary as the torque was transmitted over the guidewire.The tip would then catch up with the input rotation suddenly and quickly. The active guidewire has similar torque response to the Terumo Glidewire comparator. Both guidewires almost reach the 1:1 torque response after 5 turns.

3.1.6 Torque Strength Test

The aim of this test was to verify that the active guidewire and its joints can withstand normal rotational loading for the intended use. Following torque response

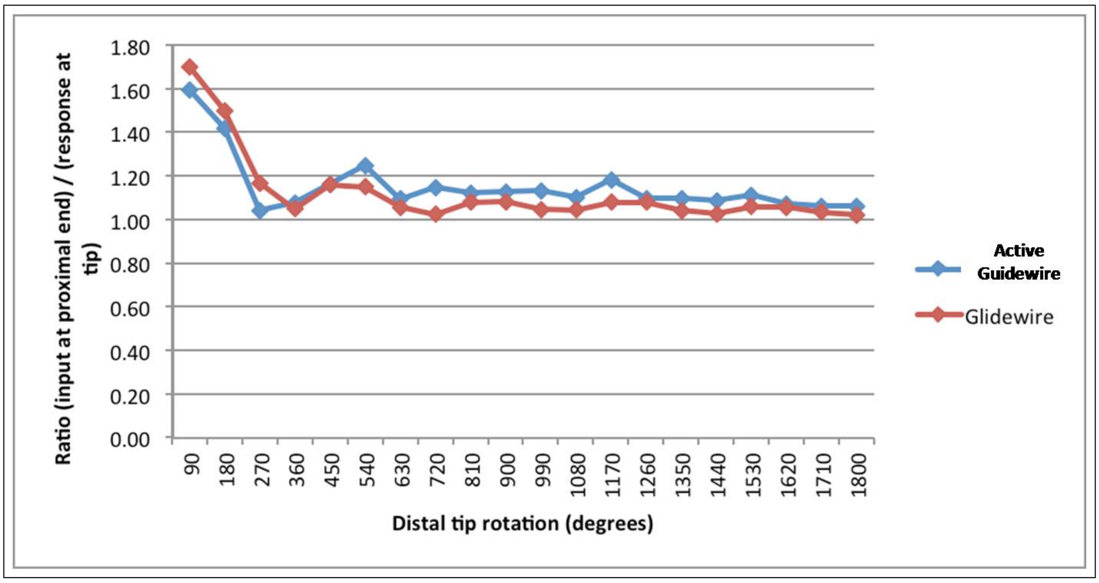

Figure 3.9 Average ratio of required input rotation at proximal end over resulting rotation at distal tip, in increments of 90 ° rotation at the tip.

testing, the tip of the guidewire was clamped in place. The proximal end was rotated in 360 ° turns counter-clockwise until signs of failure were observed, Figure 3.10. Short sections of electrical heat shrink were placed between the guidewire and the clamp to protect the Pebax insulation from being crushed by the clamp.

The average (± standard deviation) number of turns-to-failure for the Terumo Glidewire and the active guidewire were 20.8 ± 1 and 28.2 ± 5, respectively. The active guidewire had, on average, better torque strength than the Terumo Glidewire comparator.

3.2 Visualization of the Active Guidewire

In this section, we assessed the visualization characteristic of the guidewire. Signal-to-noise ratio and image artifacts of the guidewire were addressed in two separate study.

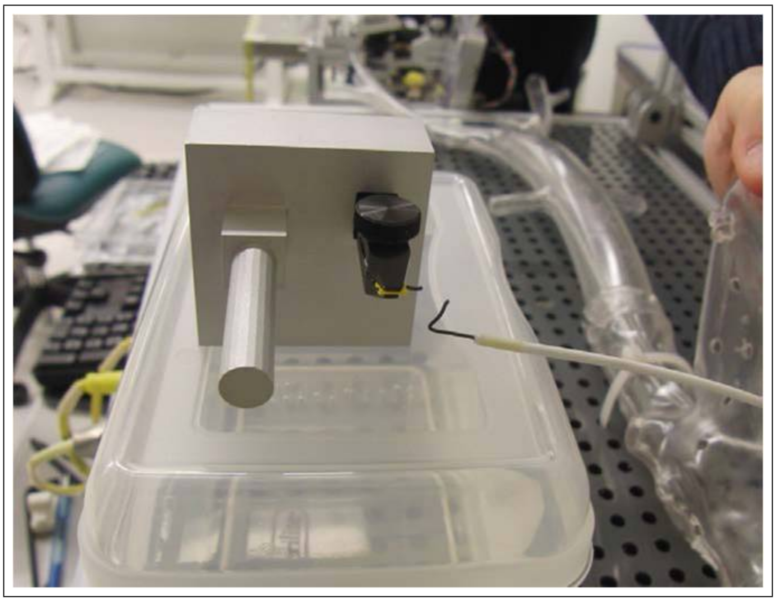

Figure 3.10 The distal tip of the guidewire was clamped in place following the Torque Response test. The proximal end was rotated until guidewire failure was observed.

3.2.1 Image Artifact of the Active Guidewire

The aim of the study was to characterize the distortion and signal loss artifact produced in an MR image by the active guidewire. Test method adapted from ASTM F2119-07 standard [90]. The test apparatus consisted of a 25 x 38 x 10 cm acrylic imaging phantom filled with a copper sulfate solution (8.27 g $CuSO_4$ in 8 L distilled water). The active guidewire was positioned in the phantom using a 5/16 inch diameter acrylic rod placed in a polypropylene peg board at the bottom of the phantom. A second 5/16 inch diameter acrylic rod was placed perpendicular to the guidewire distal to the tip such that its cross section appeared in the images. This second rod served as the reference object. Tests were performed on a 1.5 T MRI scanner (Espree, Siemens, Erlangen, Germany) using the parameters listed below:

Spin Echo	
TR	500 ms
TE	20 ms
Bandwidth	32 kHz
Field of View (Readout x Phase)	350 mm x 142 mm
Matrix (Readout x Phase)	256 x 104
Slice Thickness	3 mm
Gradient Echo	
TR	100 ms
TE	15 ms
Bandwidth	33 kHz
Field of View (Readout x Phase)	350 mm x 142 mm
Matrix (Readout x Phase)	256 x 104
Slice Thickness	3 mm
Flip Angle	30 °

Sagittal images were acquired through the device, with the device oriented along the main magnetic field. Images were acquired with the phase encode (PE) direction oriented anterior-posterior (A/P) and foot-head (F/H). Profiles were measured through the phantom with and without the device. The mean intensity through the phantom without the device was taken as the baseline signal intensity. For the profile through the device, pixels were classified as artifact if the signal intensity was decreased by at least 30%. Pixel positions were interpolated at the edge of the void. Because the device itself is quite small and appeared as a void within the dark artifact, the device itself was included in the calculation of artifact size.

Figure 3.11 , Figure 3.12 and Figure 3.13 show the spin echo images, gradient echo images and the plot of spin echo profiles, respectively. Artifact widths are reported in Table 3.3.

In conclusion, a maximum 6.5 mm artifact size was measured in SE images

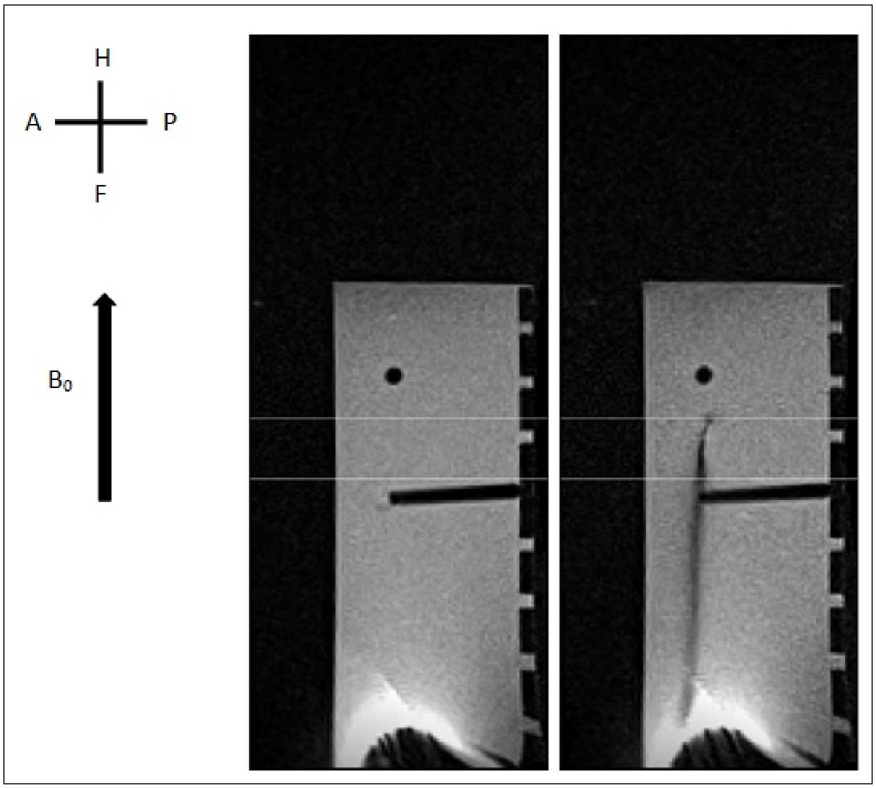

Figure 3.11 Spin echo images of phantom without (left) and with (right) device. Horizontal lines are profiles through tip coil (upper) and shaft (lower). Phase encode is A/P. Image orientation and direction of main magnetic field (B0) is shown at left of images.

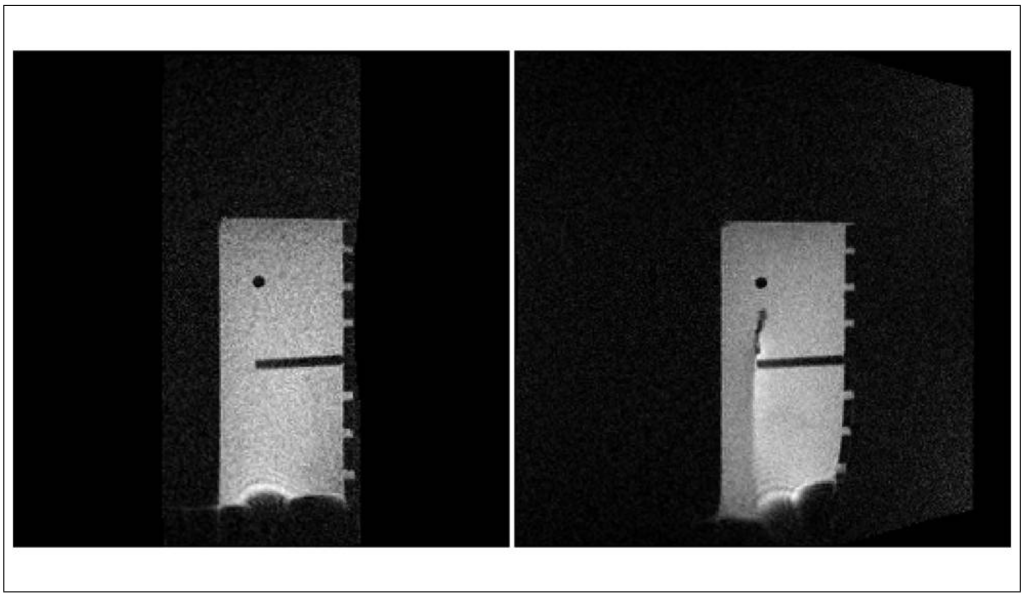

Figure 3.12 Gradient echo images of the phantom without (left) and with (right) device. Phase encode is H/F.

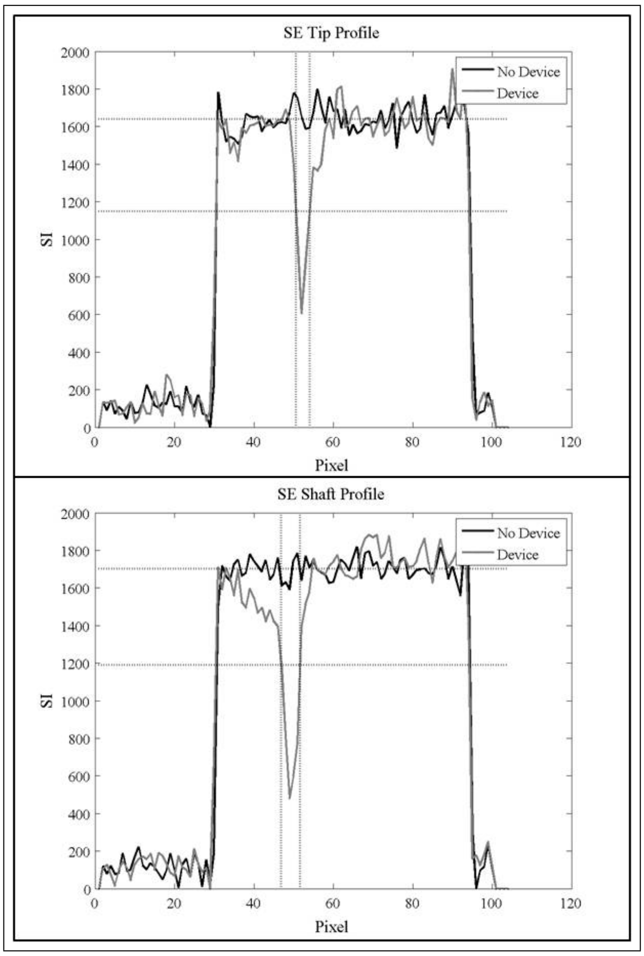

Figure 3.13 Plot of spin echo profiles through tip coil (top) and shaft (bottom). Top horizontal dashed line is mean of profile through phantom without device. Bottom horizontal line represents a 30% decrease from this value. Vertical lines represent width of artifact from device corresponding to 30% reduction in signal intensity.

Table 3.3
Artifact widths measured from spin echo (SE) and gradient echo (GRE) images.

Artifact	**Width (mm)**
SE Tip (PE: A/P)	4.8
SE Shaft (PE: A/P)	6.5
SE Tip (PE: H/F)	0
SE Shaft (PE: H/F)	6.3
GRE Tip (PE: A/P)	5.0
GRE Shaft (PE: A/P)	5.9
GRE Tip (PE: H/F)	5.0
GRE Shaft (PE: H/F)	6.2

(PE:A/P) at the shaft. This is a relatively small artifact and should not affect anatomical imaging significantly.

3.2.2 Signal to Noise Ratio Measurements

In this section, signal-to-noise ratio (SNR) of images acquired by the active guidewire was measured. One way to determine SNR from a single magnitude image is to take the average of the signal intensity (S) from a uniform region of interest (ROI) containing the object of interest and divide it by image noise, which is the standard deviation (SD) of the noise from an area containing no signal (noise only):

$$SNR = \frac{S}{ImageNoise} \tag{3.1}$$

For magnitude images in MRI, the image noise is not a Gaussian distribution but a Rician distribution. This change of noise distribution is compensated for in a single-channel system by a correction factor:

$$ImageNoise = \frac{SD}{0.66} \tag{3.2}$$

MR images of the active guidewires were acquired in a 1.5 T MRI (Espree, Siemens, Erlangen, Germany) using balanced steady-state free precession (bSSFP) sequence with following scan and data acquisition parameters:

Pixel bandwidth	698 Hz/px
Voxel dimensions	1.33 x1.33 x5 mm
Receiver channel	3dB bandwidth 178 kHz
Phantom filler specific conductance (or phantom filler composition)	0.8 g/L NaCl and 5.85 g/L polyacrylic acid into distilled water
Phantom dimensions	610 mm x 521 mm x 100 cm
Sequence repetition time (TR)	3.60 milliseconds
Echo delay time (TE)	1.80 milliseconds
Number of signals averaged (NSA)	1
Data acquisition matrix size	128x256
Field of view	170 x 340 millimeters
Pulse sequence name	ssfp
Software version	NUMARIS/4 syngo MR B17
Receive/Transmit coil(s) used	the active guidewire / Body coil
Statement of geometric distortion correction algorithm	2D syngo distortion correction
Statement of RF receive coil correction algorithm	n/a
Type of signal filters used (time and/or image domain)	n/a
Scan room temperature	19 °C
Phantom temperature	19 °C

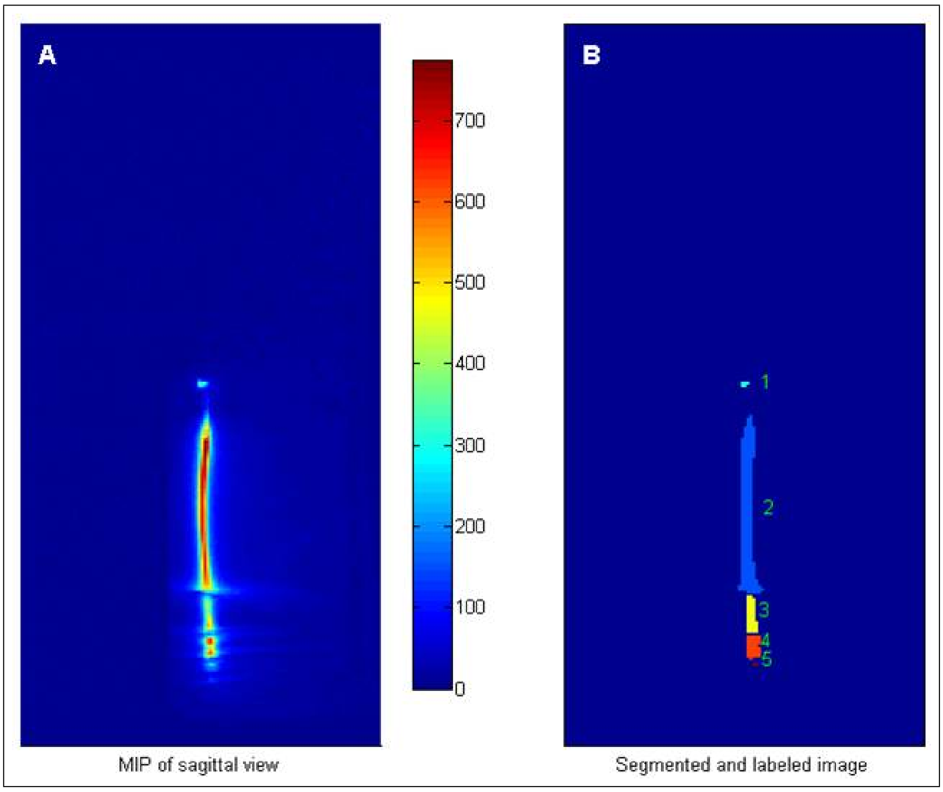

Figure 3.14 Maximum intensity projection image (A) of sagittal stack. Images were segmented and each segment was identified (B). Average pixel value for each segment was used for SNR calculation.

Guidewires were aligned parallel to the main magnetic field (B_0) and fixed in position at an insertion length of 45 cm, a horizontal offset of 12.7 cm lateral to the iso-center, and a vertical offset of 6 cm from the bottom and 2.5 cm from the top of the acrylic phantom prepared according to the ASTM F2182 standard [91]. The acrylic phantom was filled with gel made with 0.8 g/L NaCl and 5.85 g/L polyacrylic acid in distilled water. The center of 11 sagittal slices was aligned with the center of the guidewire. The distance between slices was 5 mm and the distance factor was -50%, which reduces the slice distance to 2.5 mm and overlaps two adjacent slices for 2.5 mm. Sagittal stacks of images acquired from only the device channel were used to calculate maximum intensity projection (MIP) images. MIP images were used to capture the maximum signal from the guidewire and to simplify data processing. MIP images were then segmented and both tip and shaft regions of interest (ROI) were determined, Figure 3.14. The mean value of the pixels of each ROI was calculated. Noise SD was calculated from a single, central slice for the area in the field of view without any MRI signal, in this case the air, Figure 3.15.

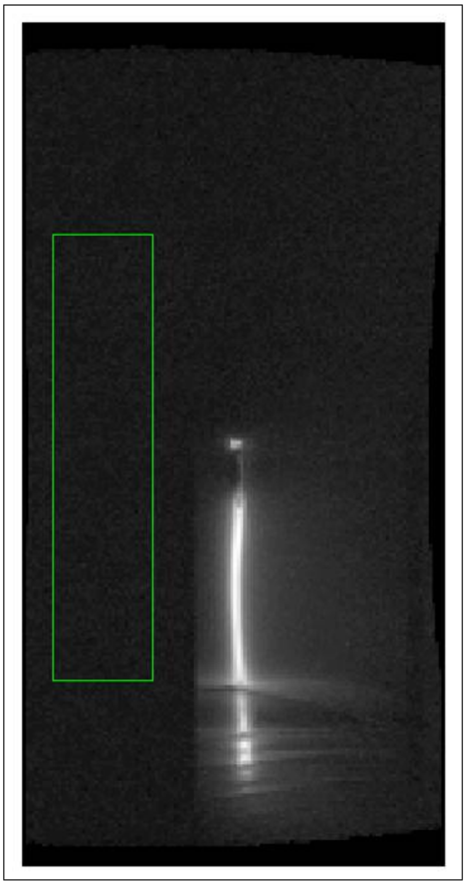

Figure 3.15 The green rectangle represents area selection where there is no signal. Noise is determined by calculating the standard deviation of the pixel values within the area.

SNR of tip and shaft of the active guidewires are given in Table 3.4.

Table 3.4
SNR values at the tip and shaft of the active guidewire

Guidewire #	SNR at Tip	SNR at Shaft	Tip/shaft SNR ratio
1	105	163	0.64
2	78	116	0.67
3	69	117	0.59
4	70	133	0.53
5	87	141	0.62
6	68	113	0.60
7	72	141	0.51
8	62	110	0.56
9	82	129	0.64
10	73	134	0.54
11	65	107	0.61
Average (Standard deviation)	76 (12)	128 (17)	0.59 (0.05)

NEMA Standards Publication MS 1-2008 [92] was used as a guidance for this test. There were some deviations from this standard because the active guidewire is an internal receiver. For example, the region of interest was determined from the area surrounding the guidewire. A rectangular acrylic phantom (ASTM F2182) was used instead of a cylindrical phantom. Images were acquired immediately before the in vitro heating test to assure that the guidewire had uniform shaft signal and conspicuous tip signal.

These data show the guidewire has acceptable shaft and tip conspicuity in vitro, with acceptable signal-to-noise ratio. The guidewire tip SNR is lower than the shaft SNR, but the qualitative image appearance (image signature) allows the two to be distinguished even though both are acquired on the same receiver channel.

3.3 RF Heating in Phantom

3.3.1 Comparison of Inner and Outer Temperature Measurement

In this section, we compared temperature measurements from the inner (embedded temperature probe) and a temporary external temperature probes positioned at the same longitudinal location on the guidewire. To compare inner and outer temperature readings at discrete locations, identical temperature sensors must be placed at the same exact longitudinal position on the guidewire. It is difficult to visualize the inner temperature probe position on the guidewire because it is hidden under the final layer of opaque black Pebax polymer. Therefore, for the purpose of this experiment, before we placed the final layer of Pebax during manufacturing, we aligned the sensor at the tip of the temperature probe with the end of the solenoid coil and marked both the temperature probe and its polyimide port housing the probe in such a way that the markers are aligned when the tip of temperature probe and the end of the solenoid coil are aligned, Figure 3.16. We called this position the *reference point*. Setting our reference point to the end of the solenoid coil allowed us to interpret the point positions of heating with respect to end of the solenoid coil. On the polyimide, a ±1 cm range was marked in 1 mm increments around the reference point mark. Heating at different positions around the reference point could be evaluated in 1 mm resolution by aligning the red mark on the probe with these tick marks on the polyimide.

To position the external temperature probe, a polyimide tube (0.011 inch OD x 0.009 inch ID) was glued to outer surface of the guidewire without an interposed gap, Figure 3.17(A). The tube extends from the proximal end of the guidewire, Figure 3.17(B), to 5 mm beyond the tip of the guidewire, Figure 3.17(C). The extension beyond the tip of the wire allows measurement of heating in the close vicinity of the guidewire tip. Note that the inner, embedded polyimide tube ends 1.5 cm proximal to the guidewire tip to preserve tip flexibility.

The external temperature probe and outer polyimide tube were marked similarly to the inner temperature probe and polyimide. When the red marking on the external

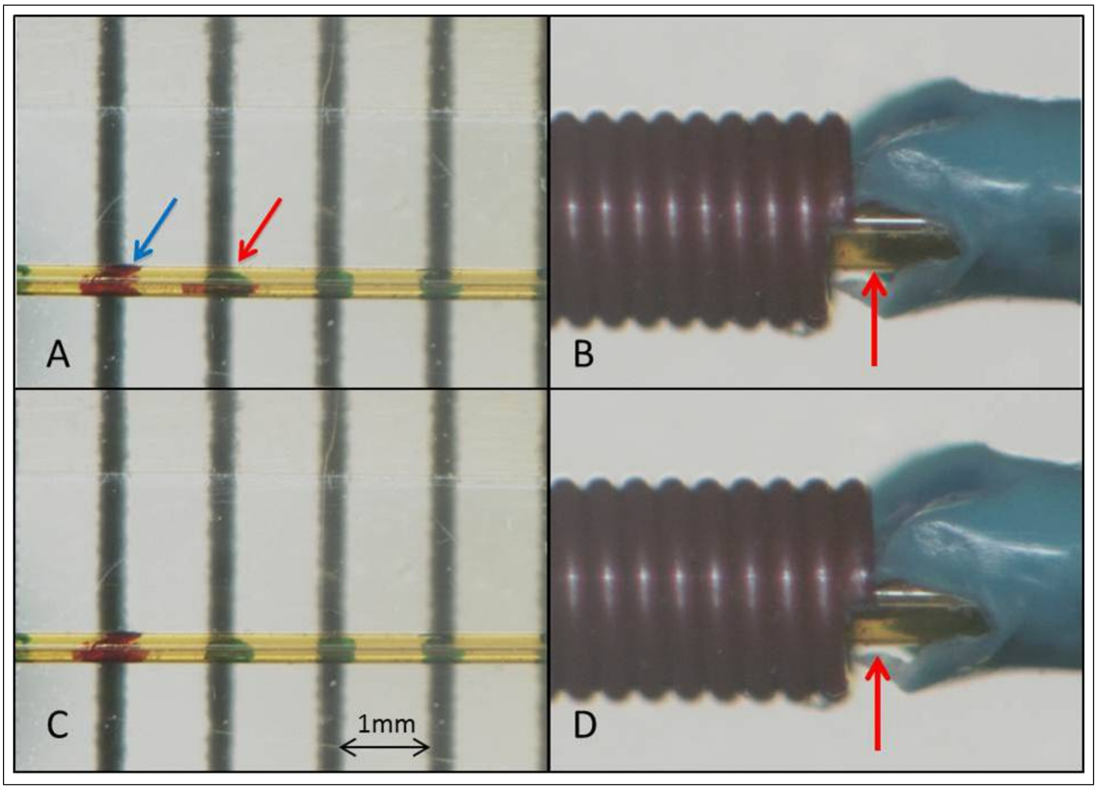

Figure 3.16 Inner temperature probe alignment with the proximal end of the solenoid coil. All images magnified X50. (A) The red mark on the polyimide (blue arrow) and the red mark on the temperature probe (red arrow) are not aligned. They are 1 mm apart. (B) Correspondingly, the sensor at the tip of the temperature probe is 1 mm proximal of the end of the solenoid coil. (C) The temperature probe was advanced 1 mm so that the red marks on the polyimide and probe align. (D) Correspondingly, the sensor at the tip of the temperature probe is aligned with the proximal end of the solenoid coil.

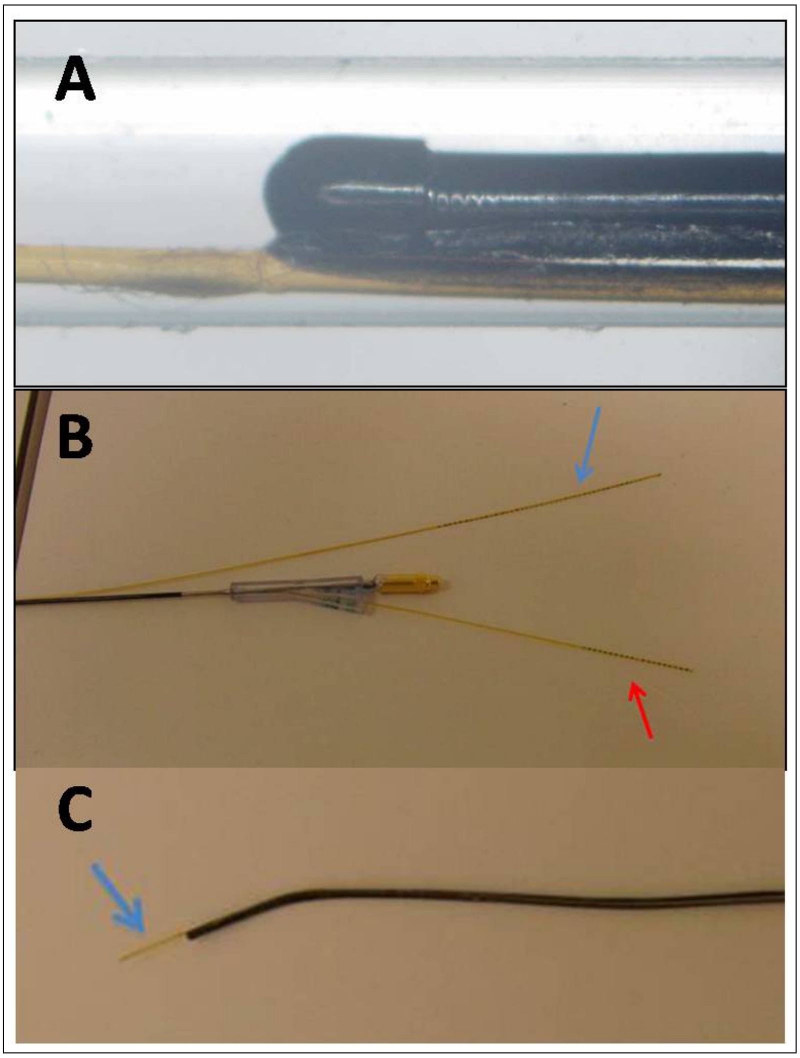

Figure 3.17 (A) The outer polyimide is fixed to the outer surface of the guidewire using in instant-cure glue without leaving a gap (X50 magnification).(B) At the proximal end of the guidewire, there are two polyimide ports, one for the inner temperature probe (red arrow) and one for the outer temperature probe (blue arrow).(C) The external polyimide tube extends 5mm beyond the curved tip of the guidewire (blue arrow) to measure heating around the tip.

temperature probe aligned with the red marking on the outer polyimide, the probe sensor was 2.5 cm proximal of the guidewire tip (at the end of the solenoid coil). This point was used as the *reference point* for the outer temperature probe. The guidewire was placed into an acrylic phantom prepared according to ASTM F2182-11a standard. The guidewire was aligned parallel to the main magnetic field and fixed in position at an insertion length of 45 cm, a horizontal offset of 12.7 cm lateral to the iso-center, and a vertical offset of 6 cm from the bottom of the acrylic phantom. A balanced steady state free precession (bSSFP) sequence was used in 1.5T MRI (Espree, Siemens, Erlangen, Germany) with the following scan parameters: repetition time (TR)/echo time (TE), 3.04/1.52 ms; flip angle, 50 °; slice thickness, 6 mm; field of view, 300x300 mm; matrix, 192x144. A 30 second baseline temperature recording was followed by a one minute static scan on each marked location. Baseline average temperature was subtracted from maximum temperature after one minute of scanning to obtain maximum temperature increase.

Maximum temperature increases from the embedded and external temperature probes at each location were calculated and plotted in Figure 3.18. Maximum temperature increases for the embedded probe and the external probe were 19.9 °C and 16.5 °C, respectively, at 2.2 cm proximal from the tip. The ratio of maximum external temperature probe increase to maximum embedded probe temperature increase at 2.2 cm is 0.83.

The temperature measured at the internal probe of the guidewire is consistently 20% higher than the temperature on the corresponding outer surface of the guidewire. Because only the outer surface of the guidewire may contact patient blood or body tissue, we believe this provides a margin of safety for real-time in vivo temperature measurements.

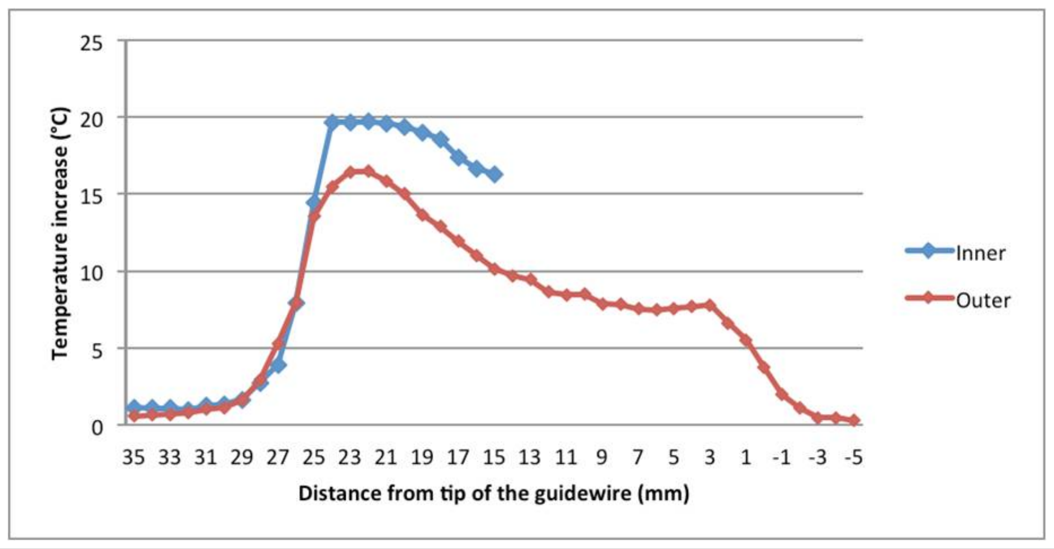

Figure 3.18 Inner and outer temperature increase on the guidewire. Positive values indicate proximal distance from the tip of the guidewire, and negative values indicate distal distance. The reference point (the proximal end of the solenoid coil) corresponds to 25 mm on the graph.

3.3.2 Physical Location of the Heat Distribution in the Active Guidewire

The purpose of this test to determine the physical location of heat distribution along the active guidewire, with regard to a geometric reference point. The reference point is the proximal end of the solenoid coil.

Guidewire preparation and experiment setup resembles the methodology used in the previous section - Comparison of inner and outer temperature measurement. We aligned the sensor at the tip of the temperature probe with the proximal end of the solenoid coil and marked both the temperature probe and its polyimide port housing the probe in such a way that the markers are aligned when the tip of temperature probe and the proximal end of the solenoid coil are aligned, Figure 3.16. Now, this position was the *reference point.*

Setting our reference point to the end of the solenoid coil allowed us to interpret the point positions of heating with respect to end of the solenoid coil. On the polyimide, a ±10 mm range was marked in 1 mm increments around the reference point mark. Heating at different positions around the reference point could be evaluated in 1 mm resolution by aligning the red mark on the probe with these tick marks on the polyimide. 10 guidewires were placed into an acrylic phantom prepared according to ASTM F2182-11a. The guidewire was aligned parallel to the main magnetic field and fixed in position at an insertion length of 45 cm, a horizontal offset of 12.7 cm lateral to the iso-center, and a vertical offset of 6 cm from the bottom of the acrylic phantom. A bSSFP sequence was used in 1.5 T MRI (Espree, Siemens, Erlangen, Germany) with the following scan parameters: repetition time (TR)/echo time (TE), 3.04/1.52 ms; flip angle, 50°; slice thickness, 6 mm; field of view, 300x300 mm; matrix, 192x144. A 30 second baseline temperature recording was followed by a one minute static scan on each marked location. Baseline average temperature was subtracted from maximum temperature after one minute of scanning to obtain maximum temperature increase. We determined the average slope of 10 heating curves to determine the characteristic heat distribution of the guidewire.

Maximum temperature increases from the inner temperature probe at each location were calculated and plotted in Figure 3.19. We were able to advance temperature probe at least 8 mm distally from proximal end of the solenoid coil for 8 guidewires. In two guidewires, the temperature probe could only be advanced 2 and 3 mm distally. We observed a sharp change in heating profile around the distal end of the coil (reference point, 0). The temperature reaches highest values 2 mm distal to the reference point (which is the proximal edge of the solenoid coil).

The physical location of the hot zone is similar for all 10 guidewires tested. A sharp deflection is observed at the reference point (proximal solenoid edge) of the temperature-position profiles, Figure 3.20. These findings inform proper positioning of the temperature probe with respect to the reference point during preparation for use. We used these findings to analyze prior study 2 experiments to register heating profiles obtained in vivo (study 2) to physical reference points.

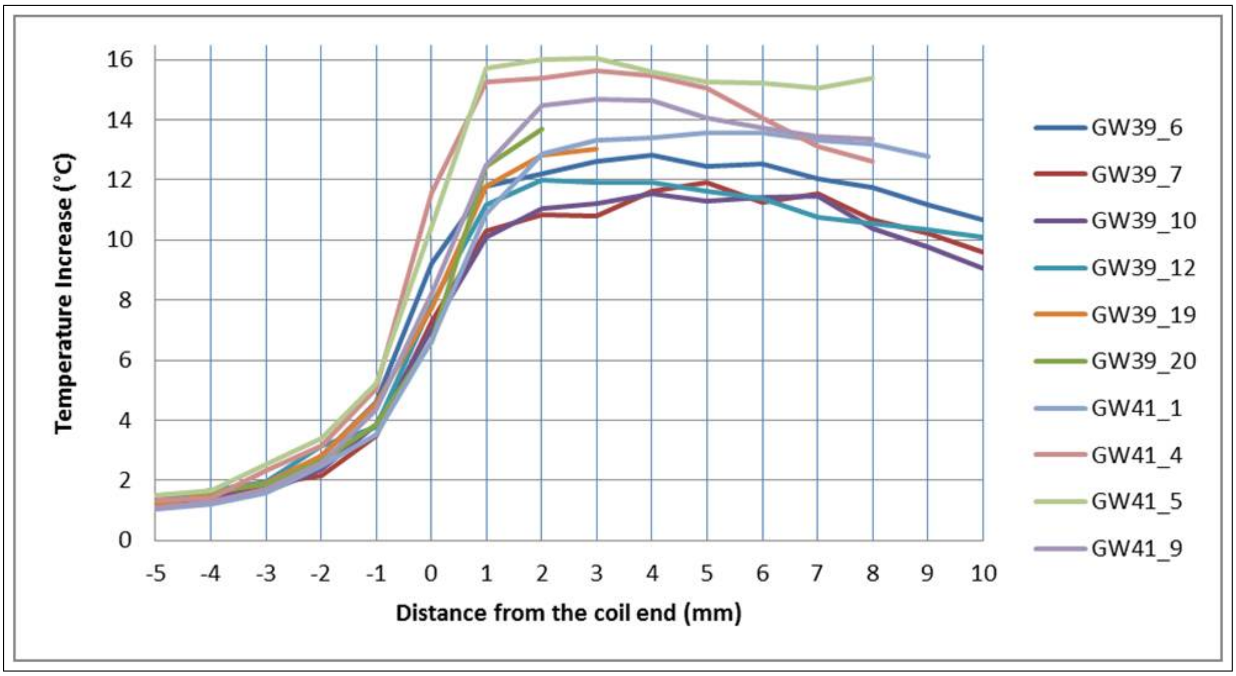

Figure 3.19 In vitro temperature-position curves of 10 guidewire samples. 0 on the X-axis indicates the proximal edge of the solenoid, which serves as the reference point. Positive numbers are distal and negative numbers are proximal to the reference point. There is a consistent inflection point on the curve that corresponds to the proximal solenoid edge.

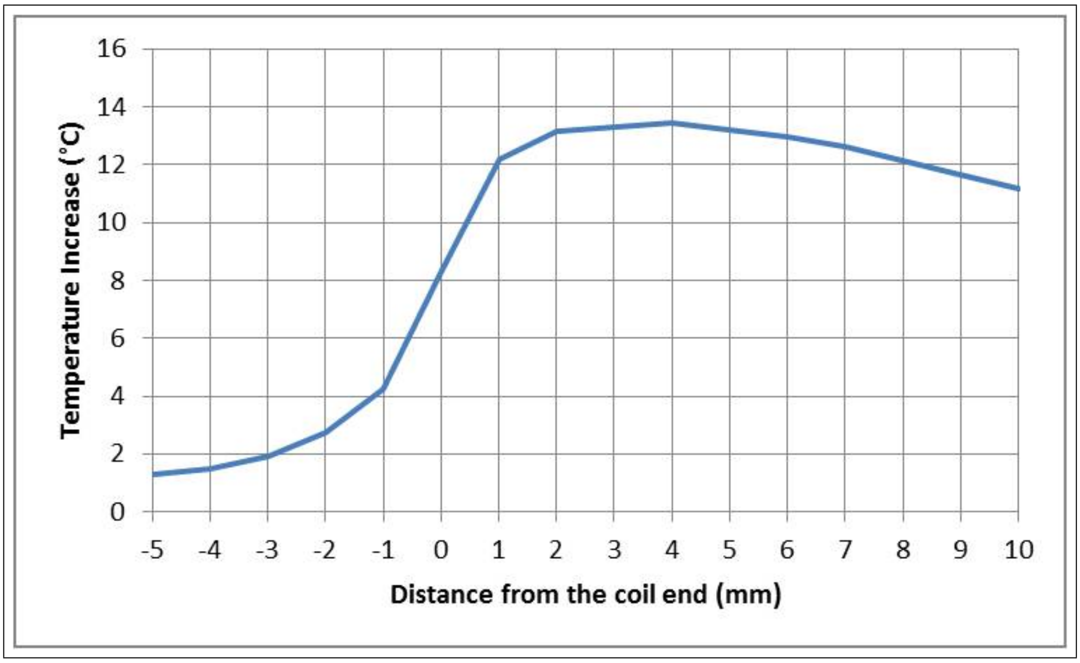

Figure 3.20 A representative graph of heat distribution on a guidewire. 0 is proximal edge of solenoid coil.

3.3.3 RF-Induced Heating Distribution in Close Vicinity of the Active Guidewire

We obtained the in vitro RF-induced heating distribution in the horizontal (XZ) and vertical (YZ) planes crossing the long (Z) dimension of the active guidewire placed in an acrylic phantom prepared according to ASTM 2182 standard.

Straight lines, 1 mm apart from each other, were drawn on a thin, rigid board (0.035 inch thick, HDPE, Manger Inc.) using red and green permanent marker. The guidewire was aligned with the center red line and fixed in place using instant-cure glue. Four polyimide tubes on each side of the guidewire were aligned with the green lines and fixed to the board, Figure 3.21. The polyimide tubes extended 5 mm beyond the tip of the guidewire. The proximal ends of the polyimide tubes were marked with red and green markings 2 mm apart. Temperature probes were correspondingly marked such that a marking on the proximal end of the probe could be aligned with the tick marks on the proximal end of the polyimide tubes to precisely place the sensors at the tips of the probes relative to the guidewire tip.

The proximal ends of the polyimide tubes were marked with red and green markings 2 mm apart. Temperature probes were correspondingly marked such that a marking on the proximal end of the probe could be aligned with the tick marks on the proximal end of the polyimide tubes to precisely place the sensors at the tips of the probes relative to the guidewire tip.

The temperature probes were advanced from the proximal end of the polyimide tubes toward the sealed distal ends. At each marked point on the polyimide, a 30 second baseline temperature recording was followed by a one minute scan at the following scan parameters: bSSFP; TR/TE, 3.04/1.52 ms; flip angle, 50°; slice thickness, 6 mm; field of view, 300x300 mm; matrix, 192x144. Maximum temperature increase was calculated for each temperature probe by subtracting the average baseline temperature from the maximum temperature during the scan. The guidewire was positioned in a gel phantom prepared according to the ASTM 2182 standard 12.7 cm left from iso-center with a

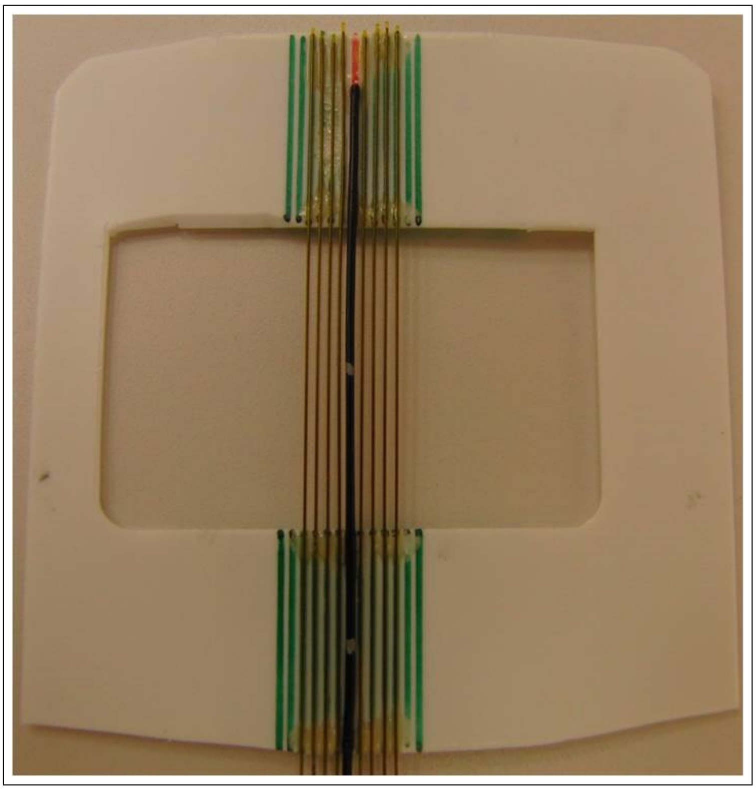

Figure 3.21 Polyimide tubes for external temperature probe advancement are aligned parallel to the guidewire, each 1 mm apart from each other. The proximal end of the solenoid coil (gray marking, red arrow) is used as a reference point for both internal and external temperature probes.

45 cm insertion length. When the orientation of the board was horizontal (parallel to the bottom surface of the phantom), the guidewire was 6 cm from the bottom of the phantom. When the board orientation was vertical (parallel to the side surface of the phantom), the guidewire was 8 cm from the bottom of the phantom. Because the signal conditioner in the temperature monitoring system has only four ports for temperature recording, one probe was inserted into the embedded polyimide port of the guidewire and the three other probes were placed in the polyimide tubes 1 mm, 2 mm and 3 mm away from the guidewire. The two sides of the guidewire (left/top, right/bottom) were tested separately. Because the inner measurement was obtained twice, we report the average temperature of the two measurements for each location of the inner probe. One measurement was taken at each point away from the guidewire.

Maximum temperature increase at each location in two planes was calculated. Heating maps were plotted by interpolating these values, Figure 3.22. Differences in maximum temperature increases between the two planes may be due in part to differences in guidewire positioning in the phantom relative to the bottom.

We found no at-a-distance hot spots in the horizontal (XZ) and vertical (YZ) planes around the guidewire. Temperature rises were higher close to the wire, and lower farther from the wire. The probe embedded inside the guidewire consistently reported the highest temperatures.

3.4 Electrical Safety

3.4.1 Background

Medical instruments powered by electricity has a potential to injure either the patient or the medical staff. Failure of protection systems may cause electric current to flow through the human body. When current is introduced between two point of the body, only a small fraction of it passes through the heart, this is called macroshocks, Figure 3.23(a) [93]. The magnitude of this current usually significantly small to cause

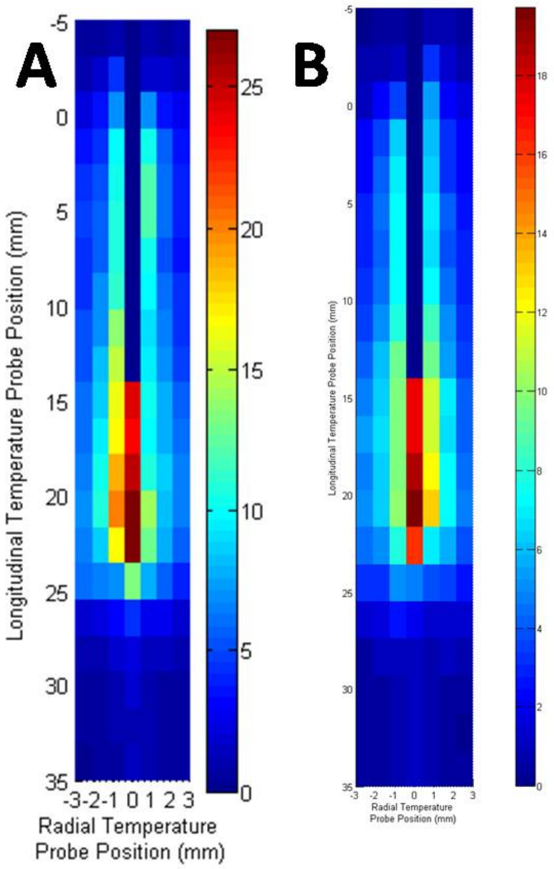

Figure 3.22 (A) Heat distribution along the YZ plane crossing the guidewire vertically and (B) heat distribution along the XZ plane crossing the guidewire horizontally. The color scale indicates the temperature increase in degrees Celsius. The longitudinal temperature probe position is indicated in millimeters from the tip of the guidewire. Negative values indicate probe positions distal of the guidewire tip. Note that the temperature probe embedded in the guidewire (radial position 0) does not extend to the tip of the guidewire. Positive values in the radial position indicate probe positions to the left of the guidewire.

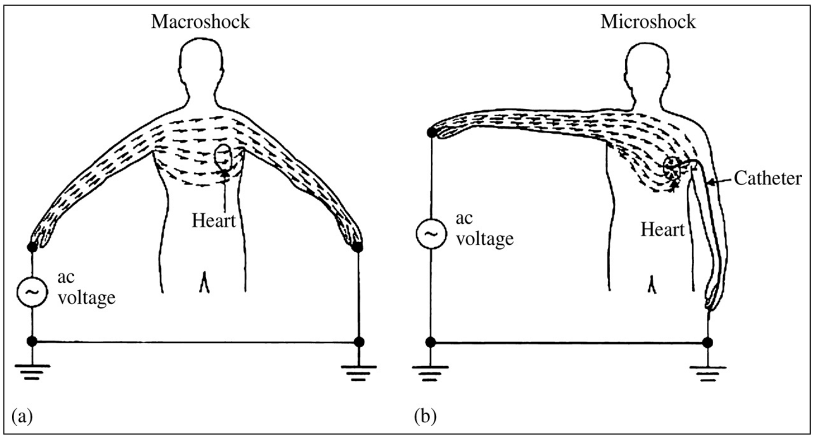

Figure 3.23 (a)Macroshock: electric current is not concentrated at heart but rather is spread throughout the body. (b) Microshock: all the current flows through the heart due to conductive catheter [93].

heart fibrilation. However, invasive devices placed in direct contact with heart may provide a conductive path to current, microshocks [94], Figure 3.23(b). These currents may result in significant tissue damage and even death. One of the main source of microshocks is leakage currents of medical devices. In this chapter, we addressed the electrical safety of guidewire mainly focusing on leakage currents.

The active guidewire incorporates a conductive outer tube and a conductive inner rod along the shaft. The inner rod extends beyond the outer tube to create a dipole antenna. Signals received by the antenna are transferred through the shaft and conducted to the tune/match/detune circuit. The tune/match/detune circuit has components to tune and match the guidewire to 50 ohm at 64MHz. A detuning component (pin diode) detunes the antenna during RF transmission.The tune/match/detune circuit is then connected to a Siemens 1.5 T 4Ch Interface (pre-amplifier), which amplifies the received MRI signal. Finally, the Siemens pre-amplifier is connected to the MRI scanner plug located on patient table. During the RF transmit a 15V detune voltage is transmitted to tune/match/detune circuit from MRI scanner through the 1.5 T 4Ch Interface. Additionally, a -30V is transmitted during the MRI signal receive. These voltages are generated from power supply located at scanner patient table and feeded through patient table plug which is rated as type B plug. Leakage current limits for type B applied part are 100 μA and 500 μA in the normal and single fault conditions, respectively. However, the active guidewire touches the heart during the intended use (right and left heart catheterization). Due to its direct contact with the heart, the active guidewire should be specified as a type CF applied part according to the IEC 60601-1 (ed.2) standard [95]. Leakage current limits for a type CF applied part are 10 μA and 50 μA in the normal and single fault conditions, respectively. Table 3.5 shows the leakage current limits for B, BF and CF applied parts. To use the active guidewire with a type B classified plug, the leakage current on that plug must be limited to 10 μA and 50 μA in the normal condition and single fault conditions. In this section, we designed and implemented a leakage current block circuit to reduce the leakage current by at least 10 fold to meet the requirements for a type CF applied part.

Table 3.5
Allowable values of patient leakage currents under normal condition and single fault condition for direct current(d.c) and alternating current(a.c) (IEC60601-1 ed.2). Unit of leakage current is in μA.

	Normal Condition		Single Fault Condition	
	d.c	a.c	d.c	a.c
TYPE B APPLIED PART	10	100	50	500
TYPE BF APPLIED PART	10	100	50	500
TYPE CF APPLIED PART	10	10	50	50

3.4.2 Methods

A leakage current block circuit was incorporated into the tune/match/detune circuit. The leakage block circuit consists of high-value capacitors to block DC and low frequency current, 60 Hz, and to pass relatively high frequencies, i.e. 64MHz, which is the Larmor frequency for a 1.5 T MRI scanner, Figure 3.24. A resistor (10kOhm ±5%, Multicomp Inc.) and two anti-parallel diodes (Voltronics Corp, MD) are placed between the signal line and the ground line to prevent possible arcing due to charge accumulation on the capacitors. We prepared a test set-up to evaluate the performance of the leakage current block circuit by comparing the leakage currents before and after the leakage current block circuit. Capacitors values tested were 620 pF, 820 pF, 1000 pF, 3000 pF, and 5100 pF. Leakage currents were measured for the normal condition

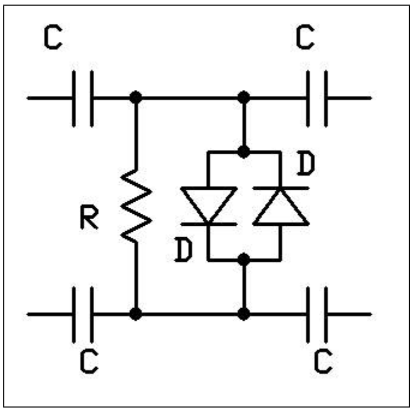

Figure 3.24 The leakage current block circuit consists of two serial capacitors on both the ground line and the signal line. A resistor and two anti-parallel diodes were used to dissipate voltage accumulations between the ground and the signal line.

and the single fault condition (disconnecting the ground line). Additionally, the double fault condition (disconnecting the ground line and the neutral line) was tested to reach the higher leakage current values.

Because the MRI scanner room is not suitable for performing the leakage current test, an MRI scanner simulator was built to replicate the current and voltage at the plug located on the scanner patient table of the Siemens 1.5 T Espree. A power supply (Vega 650, TDK-Lambda, UK) used in the Siemens 1.5 T Espree scanner is integrated into our scanner simulator to simulate the conditions of the Siemens 1.5 T Espree. Resistors were chosen to provide 100 mA current to activate the detune pin diode in the tune/match/detune circuit, Figure 3.25. The scanner simulator provides the required currents and voltages through its front panel interface to the Siemens 1.5 T 4Ch Interface and the tune/match/detune circuit, Figure 3.26. A power switch on the front panel turns the simulator on and off. Switches below the LEDs allow the operator to switch the voltage between +15V (detune state) and -30.5V (tune state). A blue LED is activated when the system is in tune mode, a red LED indicates when the system is in detune mode, and a green LED indicates that the pin diode is active and on. The MRI scanner simulator can drive 8 receive channels, but for this test we used only one channel.

The 1.5 T 4Ch Interface is connected to the MRI scanner simulator at the

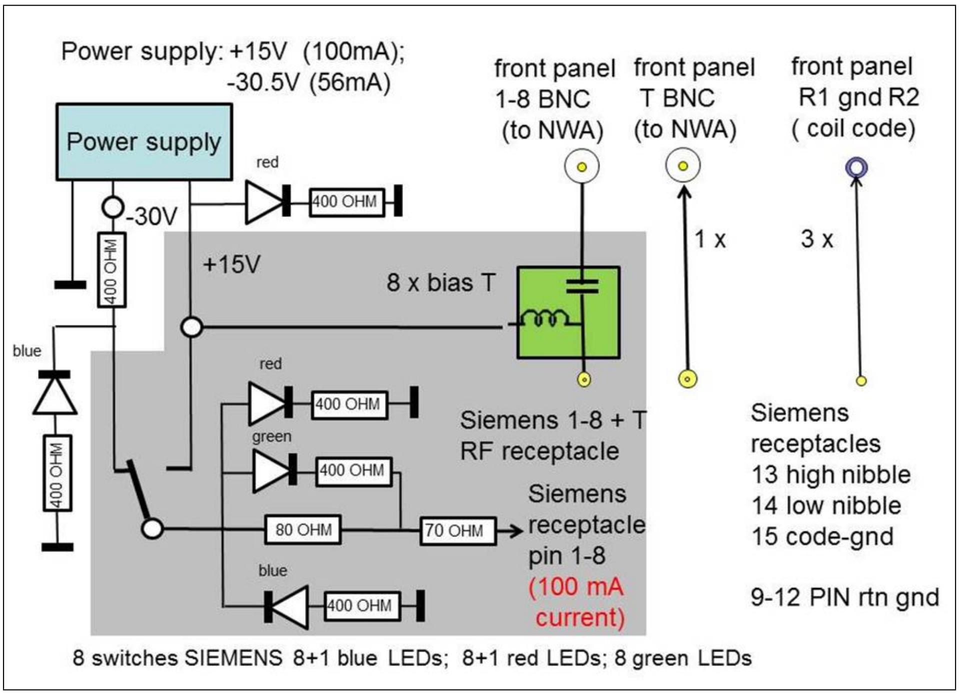

Figure 3.25 Schematic of MRI scanner simulator.

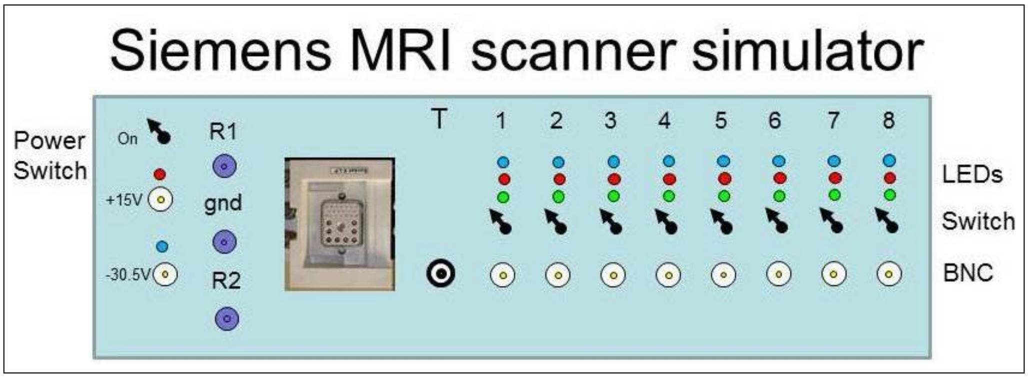

Figure 3.26 Schematic of the front panel of the MRI scanner simulator.

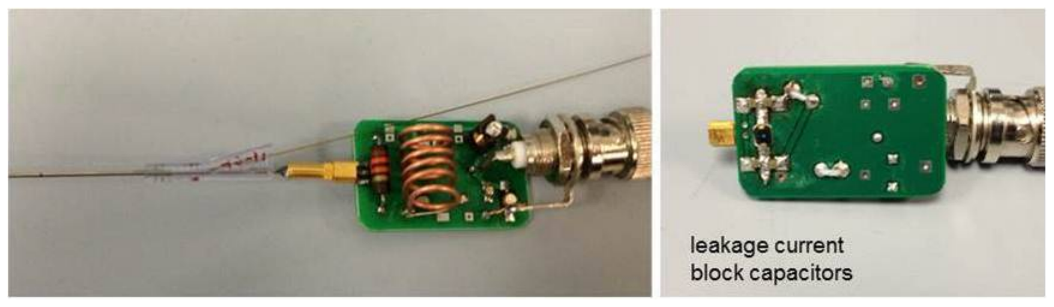

Figure 3.27 Connection between the tune/match/detune circuit and the guidewire (left), and location of leakage current block components in the circuit (right).

interface plug. The tune/match/detune circuit is connected to the 1.5 T 4Ch Interface through a BNC connector. This configuration simulates use of the 1.5 T 4Ch Interface and the tune/match/detune circuit during the clinical procedure. The tune/match/detune circuit incorporates leakage current block components before the MMCX connector, which connects the tune/match/detune circuit and the active guidewire, Figure 3.27.

To measure the leakage current before and after the leakage current block circuit, the *surface to reference* measurement was performed using the LT-601HC (ED&D Inc., NC, US) leakage current tester, Figure 3.28. The probe first was connected to the ground of the BNC connector (before leakage current block circuit) and then to the ground of the MMCX connector (after leakage current block circuit).

3.4.3 Results

Leakage current measurements were reported in Table 3.6.

3.4.4 Discussion

Lower capacitor values led to higher circuit impedances and subsequently lower leakage currents. Therefore, it is preferable to use a lower- value capacitor to block

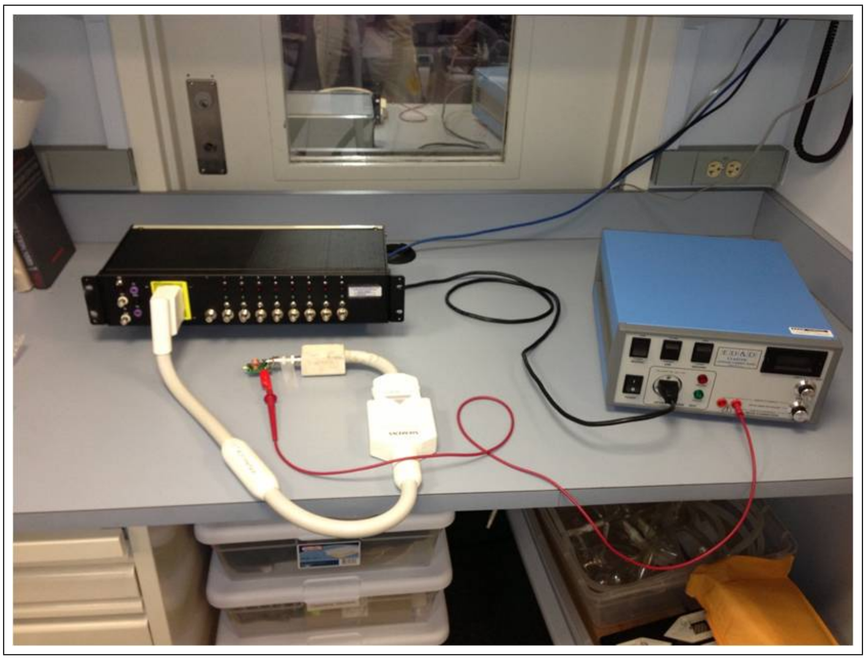

Figure 3.28 Leakage current measurement test setup. The tune/match/detune circuit and 1.5 T 4Ch Interface were connected to and powered by scanner simulator. A probe (red) from leakage current tester was used to measure leakage current on the tune/match/detune circuit.

leakage currents. However, reducing the capacitor value affects the performance of the tune/match/detune circuit components, which range between 20 pF and 47 pF. A 1000 pF value was selected as the best compromise. It provided a 21 fold reduction in leakage current. In the worst case scenario, 500 μA leakage current from type B classified table plug is reduced to 24 μA that changes the classification of guidewire to type CF. S21 measurements were performed to assess the isolation of the leakage block circuit at 63.66 MHz and 300 kHz, Figure 3.29. 300 kHz was the minimum frequency that could be measured with the network analyzer. A leakage block circuit with C = 1000 pF caused a 0.04 dB degradation at 63.66 MHz and a 20.45 dB degradation at 300 KHz. A 0.04 dB reduction at 63.66 MHz was negligible and did not affect the SNR of the signal received by the active guidewire.

```
Tr1 S11 Log Mag 10.00dB/ Ref 0.000dB [F2]
Tr2 S21 Log Mag 10.00dB/ Ref 0.000dB [F2]
Tr3 S22 Log Mag 10.00dB/ Ref 0.000dB [F2]
```

```
 1  6.3119100 MHz -0.1044 dB
 2  300.00000 kHz -20.453 dB
>3  63.660000 MHz -0.0412 dB
```

```
1 Start 300 kHz          IFBW 30 kHz          Stop 100 MHz
```

Figure 3.29 S21 measurements of leakage block circuit using 1000 pF capacitors at 63.66 MHz and 300 kHz.

Table 3.6

Leakage current (LC) was measured under normal condition,single fault condition and double fault condition using capacitor values of 620 pF, 820 pF, 1000 pF, 3000 pF, and 5100 pF. Leakage current was measured before and after the leakage current block circuit (LCBC). The ratio of the leakage current before leakage block to after leakage block is calculated for fault conditions. Unit of leakage current is in μA.

Capacitor value	Test condition	LC before LCBC	LC after LCBC	Ratio
620 pF	Normal condition	0.2	0.2	
	Single fault condition	465	17	27
	Double fault condition	898	32	28
820 pF	Normal condition	0.2	0.2	
	Single fault condition	466	19	25
	Double fault condition	899	36	25
1000 pF	Normal condition	0.2	0.2	
	Single fault condition	466	22	21
	Double fault condition	900	42	21
3000 pF	Normal condition	0.2	0.2	
	Single fault condition	468	76	6
	Double fault condition	898	150	6
5100 pF	Normal condition	0.2	0.2	
	Single fault condition	468	102	5
	Double fault condition	900	202	5

4. PRECLINICAL IN VIVO STUDY UNDER MRI: RIGHT / LEFT HEARTH CATHETERIZATION USING THE ACTIVE GUIDEWIRE

4.1 Background

In vitro heating of a conductive long wire was investigated in detailed by many groups [96, 97, 98, 99]. Even though, absolute results for heating were not coincide among the studies, authors were identified some items such as critical insertion length, high heating at the tip and correlation between absolute heating and E-field distribution. Unlike in vitro heating testing, there are quite few studies that investigated in vivo heating of conductive wire. Luechinger et al. [100] tested the temperature increase at the tip of pacemaker lead during in vivo MRI scan. Group attached a thermocouple to the tip of the leads. They measured 20 °C temperature increase during MR scan of the heart. However they did not find any histologic and pathologic change on tissue. On the other hand, Roguin et al. [101] measured no in vivo heating on the leads inserted into the right ventricle. This can be due to the blood flow effect and heat regulatory mechanism in body. In both these studies authors could not exam the in vivo heating in detail.

In this study, by using a novel temperature probe placement system, we investigated the safety and effectiveness of the active guidewire. Pre-clinical animal experiments were conducted to evaluated the MR safety, visibility and mechanical performance of the active guidewire. The main objectives of the in vivo experiments were to assure that the active guidewire system accurately reported its maximum temperature in real-time, and to assure this temperature remained within an acceptable range during various expected operating conditions. Additional aims were to assess the visibility of the guidewire tip and shaft during navigation through the vasculature, and mechanical performance during simulation of the proposed clinical procedure.

4.2 Method

Two studies of six animals each were performed in naive Yorkshire swine. Pigs were the selected model and species because their heart and arteries closely resemble human in caliber and morphology. Average weight on day of experiment was 41.7 ± 1.6 kg. Weight was limited to less than approximately 50 kg due to size constraints within the scanner bore. Experiments were open-label, non-randomized, non-blinded, observational studies. Experiments adhered to Good Laboratory Practice (GLP), and were audited by a quality assurance auditor.

The pigs in this study were sedated with 25 mg/kg Ketamine; 0.5 mg/kg Midazolam and 0.01 mg/kg Glycopyrrolate IM. A venous catheter was placed in the lateral vein and the pig was intubated. Once on the ventilator/anesthesia machine, 1.5-2% isoflurane was used throughout the procedure.

Prior to each experiment, animals were assigned to either venous or arterial femoral access to achieve three of each per study. In study 1, animals were assigned to left or right side access evenly. In study 2, all experiments were performed with left side access because it was observed in study 1 that heating was typically greater on the left. Access was obtained using a modified Seldinger technique using B-mode ultrasound assisted percutaneous access. A 6 Fr, 23 cm long introducer sheath (Fast-Cath Hemostasis Introducer, St. Jude Medical, St. Paul, Minnesota) was placed in the femoral artery and an 8 Fr, 23 cm introducer sheath (Fast-Cath Hemostasis Introducer, St. Jude Medical, St. Paul, Minnesota) was placed into the femoral vein. After vascular access was obtained, heparin 150 units/kg was administered one time to achieve an activated clotting time $>$ 200s. Supplemental heparin was given as needed to exceed this threshold. All animal experiments were performed under Siemens Espree 1.5 T MRI scanner using a balanced steady state free precession (bSSFP) MRI pulse sequence, with following scan parameters:

Parameter	**Value**
Repetition Time (TR)	2.88 ms
Echo Time (TE)	1.44 ms
Matrix	192 (X) x 144 (Y)
Field of View	350-400 mm (X and Y)
Slice Thickness	6 mm
Slices	3
Acceleration	GRAPPA, rate 2, 24 reference lines
RF Pulse Width	600 microseconds
Flip Angle	20 ° - 70 ° (Flip angle was adjusted as desired)

During the first six experiments (study 1), we observed a *zone* of relatively similar heating, rather than a single point of maximum heating data. There was also an apparent shift in the singular point of maximum heating on the guidewire between in vitro and in vivo measurement. This prompted modification of the protocol and an additional six experiments (study 2) to probe this *zone* in greater detail and with more precision. Due to time constraints of a single day per experiment, steps related to aims sufficiently answered in study 1 were eliminated and steps to probe the hot zone were added. In study 2, our primary aim was to characterize the spatial profile of the zone of heating. Secondary objectives were to confirm no other location on the guidewire heats more, and to measure with more detail temperature during an animal (simulated clinical) catheterization.

4.2.1 Experimental Design

Three stations (S1, S2 and S3) were defined as imaging windows centered at specified longitudinal distances from the femoral access point to thorax, Figure 4.1. Station 1 was approximately centered at the femoral access point. Station 3 was centered over the heart, and station 2 was placed midway between S1 and S3. The table position was moved to obtain the different stations.

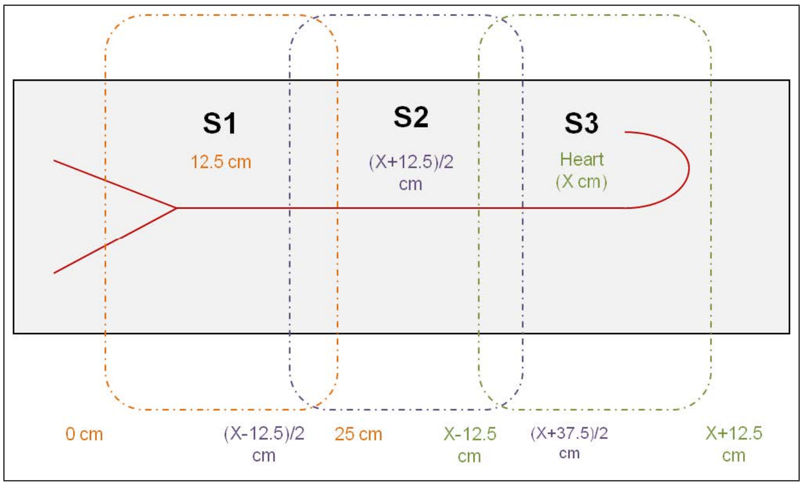

Figure 4.1 The three anatomical stations defined in the study protocol. Longitudinal distances are from femoral access point.

Static and dynamic heating tests and imaging tests were performed for each animal. Static and dynamic heating tests and imaging tests were performed for each animal. Clinical simulations and other tests (catheter advancement, user-interactive parameters, and gradient induced heating) were performed if time allowed. A scan evaluating the effect on temperature of flushing room-temperature saline through the coaxial catheter was added partway through study 1.

4.2.2 Dynamic Heating Scans

A typical dynamic heating scan consisted of a 30 second temperature baseline without MR scanning, an additional 30 seconds of MR scanning without moving the guidewire, and then guidewire advancement or pullback. Once the target was reached, the temperature monitoring and MR scanning were stopped simultaneously.

In study 1, the guidewire was advanced and withdrawn within the confines of each station to locate a station-specific critical insertion length or insertion length causing the most heating. Static scans were performed at the critical insertion length. In study 2, the guidewire was advanced from the femoral access point (station 1) or proximal edge of the field of view (stations 2 and 3) to the center of the station. Critical insertion lengths did not vary greatly among animals in study 1, and was approximately at the center of each station.

4.2.3 Static Heating Scans

Static scans were performed while the guidewire was positioned at the station-specific critical insertion length (study 1) or at the center of the imaging station (study 2). A typical static scan consisted of a 30 second temperature baseline without MR scanning followed by 60 seconds of MR scanning at flip angle 50 °. The flip angle was reduced (down to 35 °) when the temperature increase exceeded 4 °C during (study 1) or absolute temperature exceeded 43 °C; conversely the flip angle was increased (up to 70 °) if the temperature increase was low. The temperature probe was initially located at the point of maximum heating measured in vitro -in vitro hot spot-. A single static scan was first performed. Next, static scans were performed by moving the temperature probe in 1 mm increments around the in vitro hot spot. In study 1, two measurements were performed distal and proximal of the in vitro hot spot, while in study 2 the number of measurements was increased to at least five on each side. In study 1, one set of data was obtained for this range in stations 1 and 2. Data was not obtained in station 3. In study 2, three sets of data were obtained for this range in station 1 to increase the number of data points. One set was obtained in stations 2 and 3. Due to time constraints during some experiments, only the points exhibiting the highest heating in station 1 were further examined in stations 2 and 3.

4.2.4 Clinical Simulation

Either venous or arterial catheterization was performed on a given animal. Catheterization started in station 1 (femoral access point). From a venous approach, the guidewire and coaxial catheter were used to engage the superior vena cava, right atrium, right ventricle, main pulmonary artery, and left and/or right pulmonary arteries under continuous temperature monitoring at flip angle 50 ° (as default value, lowered or increased depending on heating during prior scans). From an arterial approach, the guidewire and catheter were advanced retrograde from the femoral artery, through the aortic arch, and then used to enter the left ventricle across the aortic valve. In study 2, 60 second static scans were performed at each anatomical landmark. Simulated clinical procedures were performed by an experienced interventional cardiologist.

After the simulated catheterization in study 2, the guidewire was withdrawn in 2.5 cm increments every 20 seconds from the final anatomical landmark until it was totally removed from the body. Temperature was recorded but no MR scanning was performed in order to observe any temperature gradients in the body unrelated to MR scanning.

In study 1, catheterizations were performed with the temperature probe placed at the in vivo hot spot determined during the static scans, if applicable; otherwise, the probe was placed at the in vitro hot spot. In study 2, catheterizations were performed with the temperature probe placed at the in vitro hot spot, and then, when applicable, repeated with the probe moved to the in vivo hot spot.

4.2.5 Catheter Advancement Over Guidewire

The guidewire was placed in the descending aorta or superior vena cava such that it was relatively straight. The initial coaxial catheter position was as far proximal as possible on the guidewire. The starting catheter tip position was 12.5 cm proximal to the guidewire tip when the Cook Gensini catheter was used, and 5 cm proximal to the guidewire tip when the Arrow Balloon Wedge catheter was used. While scanning, the catheter was advanced in 2.5 cm increments every 20 seconds until the catheter tip moved beyond the guidewire tip by 5 cm. The catheter was then repositioned to the catheter-guidewire tip offset causing the most heating, and a static scan was performed.

4.2.6 Temperature Profile Along the Guidewire

The guidewire was placed in the descending aorta or superior vena cava such that it was relatively straight. Starting with the temperature probe at the distal tip of the guidewire, the temperature profile along the full length of the guidewire was obtained by pulling the temperature probe manually at a relatively constant speed between the locations of maximum heating recorded during in vitro testing. At each peak, the probe was fixed stationary, and a static scan was performed. If any additional peaks not recorded in vitro were observed in vivo, the temperature probe position was noted and a static scan was performed. The probe was pulled in this manner until it exited either the animal body (indicated by a clear temperature drop below body temperature) or the guidewire.

4.2.7 In Vivo Imaging

In study 1, images acquired during the in vivo experiments were initially saved as videos. ImageJ was used to scroll through the video frames. Frames were visually evaluated, and the frame which had the most conspicuous guidewire tip was selected and evaluated.

4.3 Results

4.3.1 Study 1

The maximum measured temperature and maximum temperature rise for each station during a static scans in study 1 were summarized in Table 4.1.

Table 4.2 reports the maximum measured temperature and maximum temperature rise for each station during a dynamic scans in study 1.

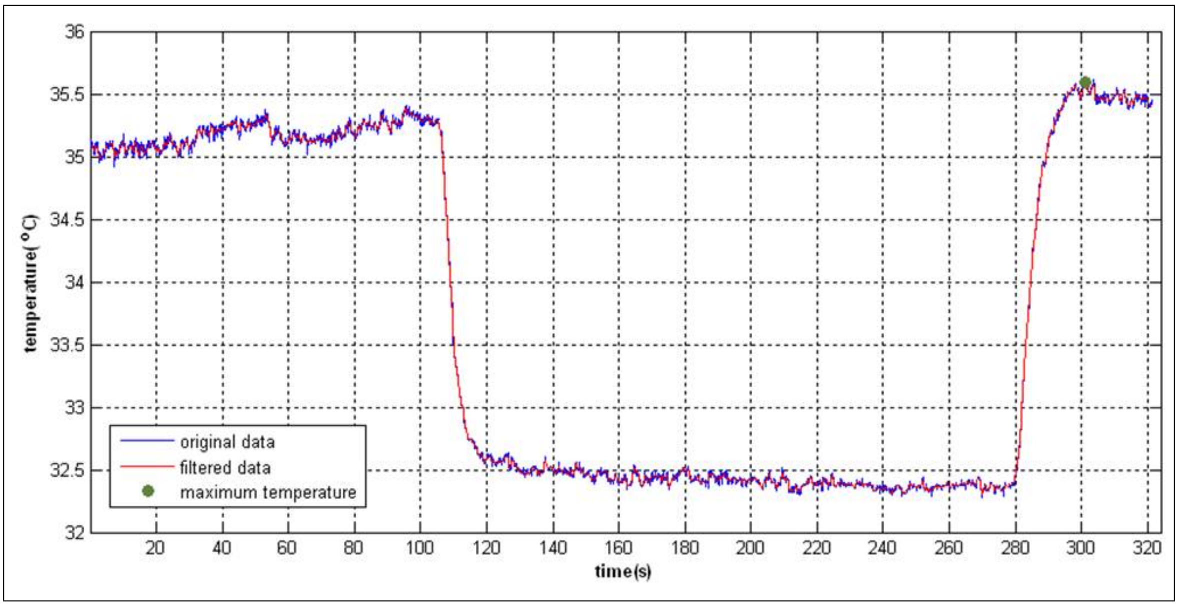

Figure 4.2 Automated continuous, low-flow saline flush through catheter. 18mL total volume saline delivered, at a rate of 0.1mL/s, 300psi pressure. Guidewire was at the station 1 critical insertion length, catheter pulled maximally back on wire, flip angle 70 °. Maximum temperature drop is 2.96 °C.

Continuous temperature monitoring was successful during a simulated clinical catheterization procedure. Sudden and unexpected temperature rises were observed when the guidewire was outside the imaging plane (due to operator error), in undesired anatomy, or when the guidewire tip was prolapsed. The Table 4.3 summarizes the experimental findings.

We tested the impact of room-temperature saline infusion via a coaxial catheter on the guidewire temperature during MRI. We used either manual or automated injection. The automated flush caused a consistent temperature drop throughout saline delivery; manual flow rate was less consistent and therefore did not lead to sustained temperature drops throughout the flush. The results show that even very low-volume saline infusion was adequate to reduce or control the temperature, Figure 4.2 shows the temperature data obtained during a 18 mL saline flush with injection rate of 0.1 mL/s. Table 4.4 shows the results of 3 experiments.

Coaxial relative movement of catheters over the guidewire impacted RF induced heating. We advanced catheters incrementally by one inch, pausing 20 seconds between

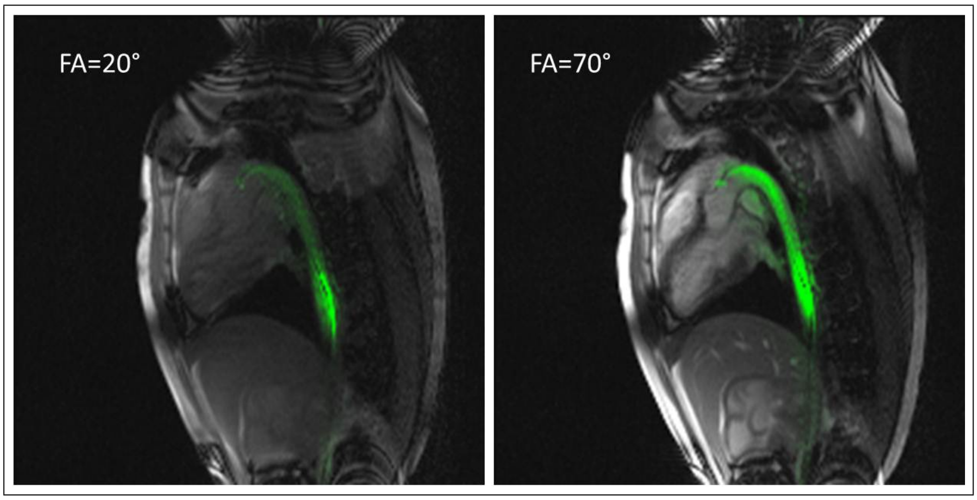

Figure 4.3 Images of guidewire positioned in aortic arch of swine. The tip and shaft of the guidewire were visible even at flip angle 20 °. Heart tissue contract was significantly lower at flip angle 20 ° compare to contrast at flip angle 70 °

moves, until the catheter extended beyond the guidewire by two inches.Findings are summarized in the Table 4.5. The maximum temperature rise was found when the catheter extended beyond the guidewire (corresponding to withdrawing the guidewire inside the tip of the catheter). We hypothesize this increased temperature rise reflects protection from the cooling effect of flowing blood. Also, under these conditions the guidewire is no longer in direct contact with the patient.

During all experiments both guidewire tip and shaft exhibited adequate conspicuity scores, even at the lowest MRI flip angle (20 °), Figure 4.3. This suggests MRI visibility is adequate for the proposed catheter procedure even at low flip angles that correspond to low MRI signal-noise ratio (SNR).

Mechanical performance of the active guidewire was evaluated by experienced interventional cardiologists during the proposed clinical procedure, but performed in healthy swine. The below table shows that mechanical performance of the guidewire was rated as adequate.

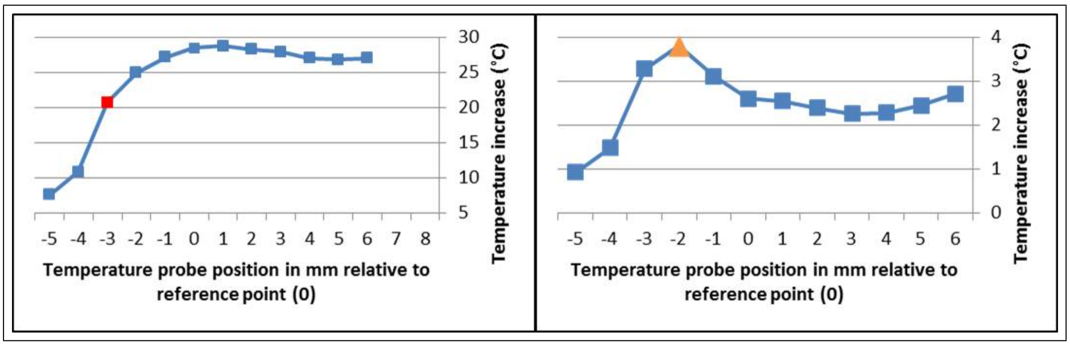

Figure 4.4 In vitro (left) and in vivo (right) heat distributions.

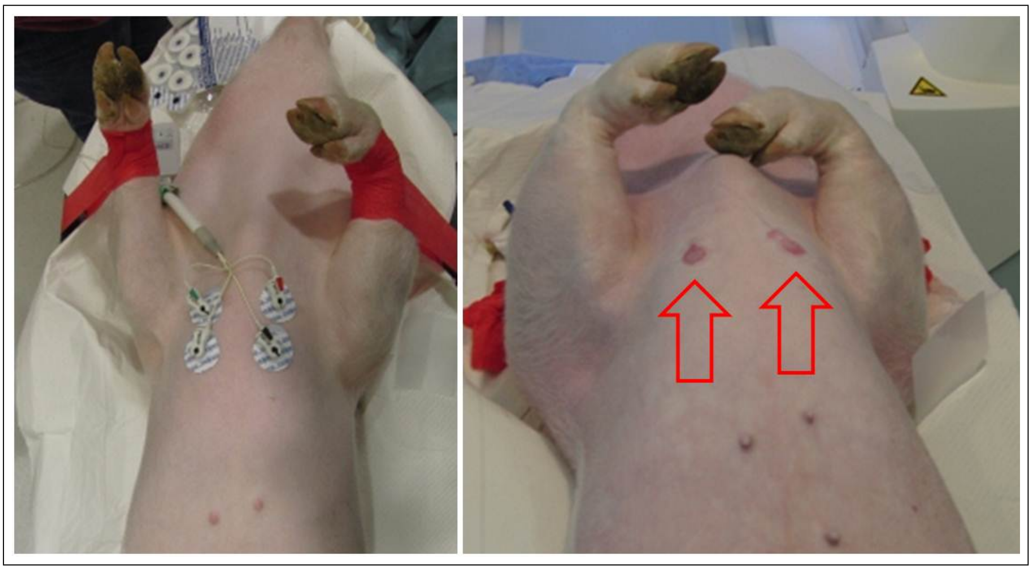

Figure 4.5 Skin photos of the animal were taken before (A) the experiment and after (B) the experiment. Metal ECG leads caused skin burn (red arrows) due to RF-induced heating.

4.3.2 Study 2

We combined the in vivo and phantom experiments to characterize the spatial heating profile of the hottest spot the active guidewire. A spatial temperature map in 1 mm increments around a reference point were acquired both for phantom and for in vivo test , Figure 4.4.

In one case, we observed a skin burn related to ECG leads, Figure 4.5.

4.4 Discussion

In study 1, at all three stations, we were able to perform MRI at a flip angle of up to 70 ° without exceeding the 4 °C temperature threshold increase at all three imaging stations. We consistently observed the highest temperature increase in station 1 compared to other stations. This observation is consistent with the high intensity E-field distribution predicted over the animal body that is in a superficial guidewire position within vasculature and the groin area. During static and dynamic scans, the maximum temperature values were all below 43 °C.

During simulated clinical catheterization, transient temperature rises were observed when the guidewire was outside the imaging plane, in undesired anatomy, or when the guidewire tip was prolapsed. These suggest the value of continuous temperature monitoring.Coaxial relative movement of catheters over the guidewire impacted RF induced heating, especially when the guidewire tip is retracted inside a coaxial catheter. We hypothesize this increased temperature rise reflects protection from the cooling effect of flowing blood. Under these conditions the guidewire is no longer in direct contact with the patient.

Even low-volume infusion of room-temperature saline significantly reduced the temperature of the guidewire during MRI operation. A possible solution to decreasing RF heating during catheterization can be a saline flush, which is a standard procedure in many catheterization laboratories used to prevent blood clots [102].

Guidewire tip and shaft exhibited adequate conspicuity even at the lowest MRI flip angle (20 °). This suggests MRI visibility is adequate for the proposed catheter procedure even at low flip angles that correspond to low MRI SNR. Of note, physicians prefer higher flip angles to provide higher SNR of the target organs.

Mechanical performance of the guidewire was rated as adequate, by experienced interventional cardiologists during the proposed clinical procedure simulation in healthy swine.

In study 2, we found a close correlation between the in vivo heating peak and end of solenoid coil. In vivo hot-spot was 1 mm distal from the proximal end of the coil. That allowed us to place temperature probe without performing phantom heating test. That means guidewire doesn't need to leave cleanroom that decreases the risk of contamination of guidewire.

Heating in vivo was found to be greatest in the pelvic location (station 1) compared with other anatomic regions. We attribute this heating to positioning in a superficial location near the groin, where the electrical field induced by RF excitation is predicted to be high.

Conducting an in vivo study complying with GLP, enable us to perform a uniform, consistent, reliable and reproductive research. All the data were recorded, processed and stored according to GLP standard. This high standards allowed use to identify the adverse events during the procedure. For example, skin burn related to ECG probes was identified.

In conclusion, we validated the temperature measurement system's accuracy and efficiency by conduction comprehensive in vivo studies. We believe these experience will lead us to perform safe and effective clinical right/left heart catheterization.

Table 4.1
Maximum temperature and maximum temperature difference recorded during a **static** scan at each station. (LV=Left vein, LA=Left artery, RV=Right vein, RA=Right artery, FA= Flip angle, IL= Insertion length)

Animal ID	Access	Station	Max T(°C)	Max ΔT(°C)	FA(°)	Probe position at Max ΔT	IL (cm)
1	LV	1	39.92	1.26	70	2mm proximal to phantom hot spot	12.5
	LV	2	40.31	0.37	70	18.2cm proximal to phantom hot spot	35
	LV	3	40.29	0.37	70	phantom hot spot	47.5
2	LV	1	37.22	2.66	70	In vivo hot spot	7.5
	LV	2	37.48	1.58	70	2mm distal of in vivo hot spot	42.5
	LV	3	35.78	0.16	70	In vivo hot spot	72.5
3	LA	1	41.14	3.69	70	Phantom hot spot	20
	LA	2	39.01	0.30	70	19.7cm proximal to the in vivo hot spot	35
	LA	3	39.19	0.24	70	In vivo hot spot	67.5
4	RA	1	35.94	0.52	70	Phantom hot spot	25
	RA	2	39.37	0.292	70	11.1cm proximal to phantom hot spot	42.5
	RA	3	39.29	0.23	70	Phantom hot spot	75
5	RA	1	37.59	1.47	70	1mm distal to in vivo hot spot	17.5
	RA	2	38.40	1.30	70	1mm distal to in vivo hot spot	25
	RA	3	40.65	0.09	70	In vivo hot spot	62.5
6	RV	1	36.92	0.51	70	2mm proximal to phantom hot spot	0.51
	LV	2	39.83	0.28	70	Phantom hot spot	37.5
	RV	3	38.43	0.38	70	Phantom hot spot	75

Table 4.2
Maximum temperature and maximum temperature difference recorded during a **dynamic** scan at each station. (LV=Left vein, LA=Left artery, RV=Right vein, RA=Right artery, CIL=Critical insertion length, FA= Flip angle).

Animal ID	Access	Station	Max T(°C)	Max ΔT(°C)	Probe position at Max ΔT	FA	Protocol
1	LV	1	40.52	2.12	Phantom hot spot	70	Locating CIL
	LV	2	40.30	1.10	Phantom hot spot	70	Locating CIL
	LV	3	40.13	0.45	Phantom hot spot	70	Locating CIL
2	LV	1	36.96	2.88	Phantom hot spot	70	Locating CIL
	LV	2	38.47	3.89	In vivo hot spot	70	Locating CIL
	LV	3	36.28	0.63	In vivo hot spot	70	Locating CIL
3	LA	1	39.76	2.75	Phantom hot spot	70	Locating CIL
	LA	2	38.39	0.28	In vivo hot spot	70	Dynamic guidewire pullback
	LA	3	39.21	1.09	In vivo hot spot	70	Attempting to pass over aortic arch
4	RA	1	36.62	0.8	Phantom hot spot	50	Guidewire advancement at station
	RA	2	39.26	2.27	Phantom hot spot	50	Guidewire advancement at station
	RA	3	39.84	0.21	Phantom hot spot	70	Dynamic guidewire pullback
5	RA	1	37.13	1.08	Phantom hot spot	70	Dynamic guidewire pullback
	RA	2	37.68	0.85	In vivo hot spot	70	Locating CIL
	RA	3	40.62	0.72	In vivo hot spot	70	Dynamic guidewire pullback
6	RV	1	36.12	0.58	Phantom hot spot	50	Guidewire advancement at station
	LV	2	38.45	0.89	Phantom hot spot	50	Guidewire advancement at station
	RV	3	39.29	1.14	Phantom hot spot	70	Dynamic guidewire pullback

Table 4.3
Maximum temperature and maximum temperature increase during clinical protocol simulation. (LHC = Left heart catheterization, RHC = Right heart catheterization, FA= Flip angle)

Animal ID	LHC or RHC	Max T(°C)	Max ΔT(°C)	FA	Probe position at Max ΔT	Notes
2	RHC	38.07	2.15	70	In vivo hot spot	Maximum temperature increase occurred while attempting to navigate from left pulmonary artery to right pulmonary artery.
3	LHC	39.88	0.81	70	In vivo hot spot	Maximum temperature increase occurred when the guidewire was in a coronary artery.
4	LHC	39.92	1.23	70	Phantom hot spot	Maximum temperature increase occurred when the guidewire was prolapsed.
5	LHC	41.02	1.05	70 (max T), 50 (maxΔT)	In vivo hot spot	Maximum temperature increase occurred in the left ventricle, possibly touching endocardium.
6	RHC	39.03	1.20	70 (max T), 40 (maxΔT)	Phantom hot spot	Maximum temperature increase occurred deep in the left pulmonary artery.

Table 4.4

Effect of room-temperature saline (0.9% sodium chloride) flush during in vivo experiments. Flush was injected either manually using a syringe or via an automated power injector (MEDRAD Spectris MR Injector System). Temperature drop was calculated as the difference between the minimum temperature in the heating scan after flushing started and the starting temperature.

Animal ID	Station	Volume	Rate (ml/s) or Time(s)	ΔT drop (°C)	FA	IL (cm)	Catheter guidewire configuration
4	1	18	0.1 mL/s	2.96	70	25	Catheter tip 10 cm proximal of guidewire tip
	3	8	0.1 mL/s	0.12	70	75	Catheter tip 2.5 cm proximal of guidewire tip
	3	4	0.1 mL/s	0.55	70	75	Catheter and guidewire tips aligned
5	1	1	over 33s	1.46	70	17.5	Catheter tip 12.5 cm proximal of guidewire tip
	2	1.6	over 30s	1.88	70	25	Catheter tip 12.5 cm proximal of guidewire tip
	3	2	over 30s	0.49	70	62.5	Catheter and guidewire tips aligned
6	1	1.5	over 65s	2.74	70	12.5	Catheter tip 10 cm proximal of guidewire tip
	2	4	over 55s	0.21	70	37.5	Catheter tip 10 cm proximal of guidewire tip
	3	4	over 37s	2.53	70	75	Catheter tip 2.5 cm proximal of guidewire tip

Table 4.5
Temperature increase at the critical catheter-guidewire configuration (configuration causing the most heating.) When the catheter tip completely covers the guidewire tip or beyond, observed heating increases. (FA= Flip angle, IL= Insertion Length)

Animal ID	Critical catheter-guidewire configuration	ΔT (°C)	FA	IL	Probe Position
2	Catheter tip 2.5 cm beyond guidewire tip	0.23	70	NA	In vivo hot spot
3	Catheter tip 2.5 cm beyond guidewire tip	1.19	70	67.5	In vivo hot spot
4	Catheter tip 2.5 cm behind guidewire tip	0.86	70	75	Phantom hot spot
5	Tips aligned	0.43	70	62.5	In vivo hot spot
6	Catheter tip 2.5 cm beyond guidewire tip	0.97	70	75	Phantom hot spot

Table 4.6
Operator scoring of guidewire mechanical performance during simulated clinical catheterization in vivo. Score: (1)=Not adequate for catheterization; (2)=Adequate for catheterization; (3)=Excellent.

Animal ID	LHC / LHC	Torquability	Catheter compatibility	Ease of navigation in vasculature	Ability to engage target
2	RHC	2	2	2	2
3	LHC	2	3	2	2
4	LHC	2	3	2	3
5	LHC	2	3	2	2
6	RHC	2	2	2	2

5. FEEDBACK CONTROL SYSTEM TO ADJUST MRI SCAN PARAMETERS

5.1 Background

Interventional devices used for MRI-guided intravascular procedures may incorporate a conductive metal shaft to provide mechanical support [51, 54]. Excessive heating at the tip of the wire has been reported for long conductive wires, which electrically couple to the RF transmit coil during MRI scans [67, 80]. In these studies, heating tests were conducted in gel phantoms, which may not represent in vivo conditions. Luechinger and his group reported up to 20 °C temperature increase during MRI at the tip of a pacing lead implanted in swine heart [100]. However, pathology and histology did not show heat-related damage in scar tissue around the lead tip. Roguin *et.al.*, on the other hand, published only a 0.5 °C temperature increase in vivo at the tip of a pacemaker lead [101]. Histological results also showed no significant necrosis or fibrosis around the tip of the lead. Our group performed an extensive in vivo heating test and reported non-significant temperature increases during normal device use. However, we observed a 20 °C temperature increase during high-power RF excitation (flip angle 90 °) [103]. In some rare and unpredictable conditions temperature can reach biologically unsafe values. Identifying these conditions and responding by changing the scan parameters in real-time can be crucial to perform safe procedures. One of the factors determining the amount of RF-induced heating of long conductive wires is RF pulse shape. A general RF pulse shape is given in Figure 5.1. The RF pulse produces a B1 magnetic field perpendicular to B_0 and an electric field parallel to B_0. The B_1 magnetic field excites the rotating spins and creates flip angle. The magnitude of the flip angle is calculated by:

$$\theta = \gamma \int_0^T B_1(t)\, dt \tag{5.1}$$

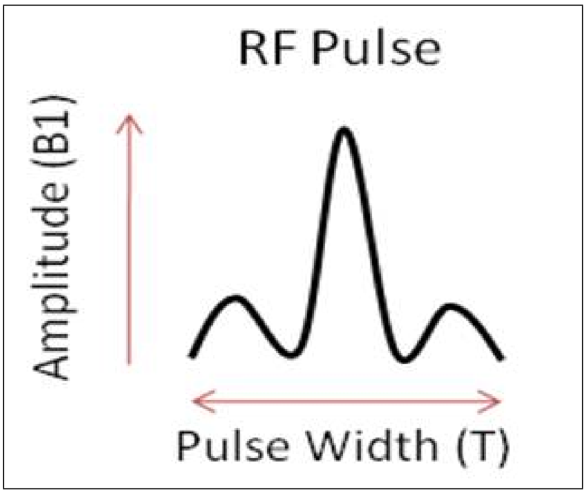

Figure 5.1 Diagram of an RF pulse. Amplitude B_1 and width (T) determine the magnitude of flip angle.

where θ is flip angle, γ is gyromagnetic ratio, and T is pulse width. Therefore, flip angle is proportional to B_1 magnitude and pulse width.

Specific absorption rate (SAR), on the other hand, is a measure of absorbed energy by unit volume in a unit time when the body is exposed to the RF field. SAR is calculated from the electric field within the tissue by:

$$SAR = \frac{1}{2}\frac{\sigma}{\rho}E^2\left(r\right) \tag{5.2}$$

Where ρ is conductivity and σ is density.Because the electric field is orthogonal and directly proportional to the B_1 field, any changes in flip angle result in an SAR change in tissue. Therefore, RF pulse amplitude (B_1) and width can be adjusted to control SAR, which results in heating in tissue. To control the scan parameters, we developed a PID based feedback control system that utilizes real-time temperature data sent by a fiber optic sensor positioned at the hottest spot of a guidewire. The aim is to detect unexpected temperature increases and respond by changing the flip angle or RF pulse width.

5.2 Methods

5.2.1 Temperature Feedback System to Control Scan Parameters

An MRI active guidewire incorporating a fiber optic temperature probe in the shaft was manufactured. The hottest spot on the guidewire was identified and the temperature probe was positioned to this point according to methods described previously[8]. The effect of flip angle and RF pulse width on device heating was evaluated both in a phantom and in vivo. In vitro, the guidewire was aligned parallel to the main magnetic field and fixed in position at an insertion length of 35 cm,a horizontal offset of 12.7 cm lateral to the iso-center, and a depth 6 cm from the bottom of an acrylic box filled with a polyacrylic acid gel prepared according to the ASTM-2082 standard. In vivo experiments were performed in a Yorkshire swine (50kg). An 8 Fr x 23 cm introducer sheath (St.Jude, Minnesota) was used for transfemoral vein access in the left side, and the guidewire was inserted 15 cm. Heating tests were performed in a 1.5 T Siemens Espree scanner using a bSSFP sequence with the following scan parameters: repetition time (TR)/echo time (TE), 2.88/1.44 ms; slice thickness, 6 mm; field of view, 340x340 mm; matrix, 192x192. Heating data was acquired for flip angles 50 °, 45 °, and 30 ° and RF pulse widths 600 μsec, 1800 μsec,and 3000 μsec. After a 30 second baseline measurement, temperature was recorded for 60 seconds during MRI. Maximum temperature increase was calculating by subtracting average baseline temperature from maximum recorded temperature. In addition to the device heating, flip angle and RF pulse width also affect the SNR of an MR image. To evaluate the effect of flip angle and RF pulse width on SNR, healthy volunteers were scanned with real-time bSSFP sequences and heart images were acquired. SNR of the heart tissue and blood was calculated and compared for flip angles 50 °, 45 °, and 30 ° and RF pulse widths 600 μsec, 1800 μsec, and 3000 μsec. To perform safe interventional procedures, anatomical structures and device location in the patient body should be visible to the operator. Because higher flip angles are preferred for higher SNR but lower flip angles are preferred for RF-safe procedures, the flip angle needs to be optimized in real-time during an MRI scan. Likewise, RF pulse width affects the heating of the device and SNR of the image,and should be adjusted in real-time as well.Real-time flip angle and

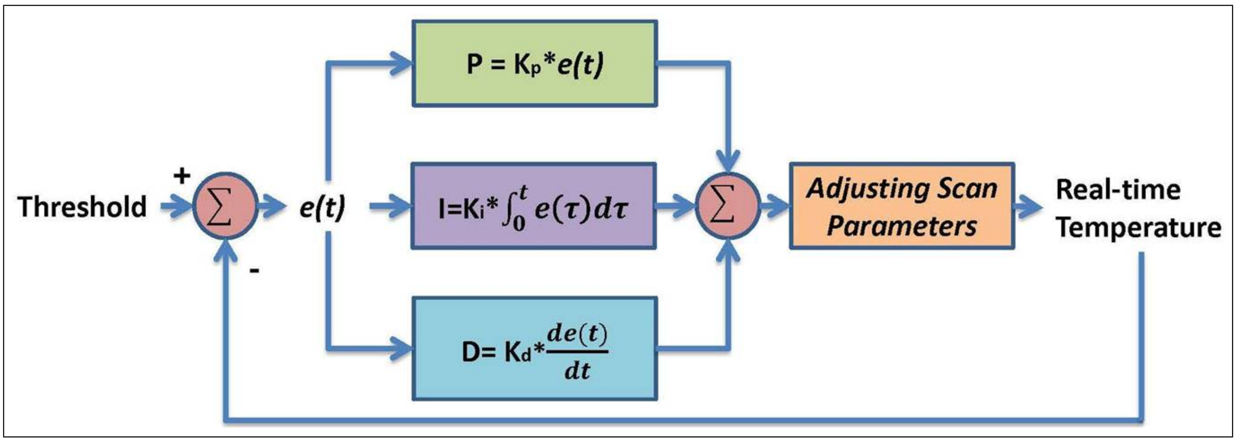

Figure 5.2 Block diagram of a PID controller.

RF pulse width optimization would allow immediate response to temperature increases and return to more desirable imaging parameters once heating subsides.

5.2.2 PID Controller

A proportional -integral -derivative (PID) controller was implemented and tested to control and optimize flip angle and RF pulse width in real-time during MRI. The PID controller calculates the difference (error) between real-time temperature on the device and a set temperature and changes the scan parameters to minimize the difference. The three components of the PID controller - a proportional element, an integral element, and a derivative element - use errors as input to calculate the present error ($e(t)$), accumulation of past errors ($\int_0^T e(\tau)d\tau$) and prediction of future errors based on current rate of change ($(de(\tau))/d\tau$). These values are multiplied with gain constants Kp, Ki and Kd, Figure 5.2.

The proportional term changes the scan parameters by the current error multiplied by the gain constant Kp. Kp, determines how quickly the system reaches the set value. The system reaches the set value more quickly with a higher value of Kp. However, this causes large oscillations in the output. In contrast, the output has less oscillation with a smaller Kp, but the system stabilizes more slowly. The contribution

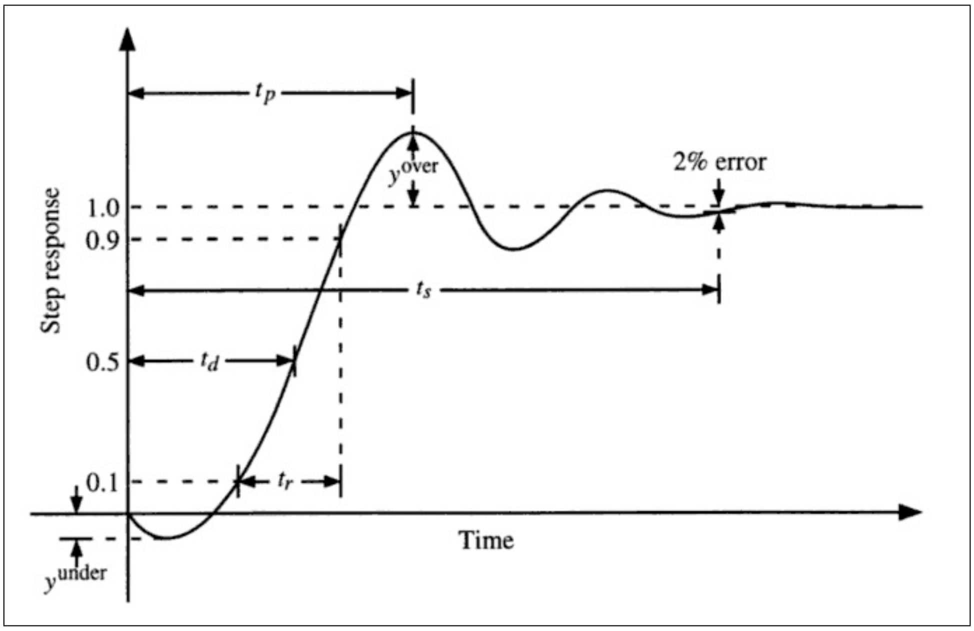

Figure 5.3 Transient specifications of the step response.(From Tay, Teng-Tiow; Iven Mareels, John B. Moore (1997). High performance control. p.93)

of the integral term is proportional to the magnitude and duration of the error. The integral term accelerates system stabilization. The derivative term predicts system behavior by calculating the current changes in error. The derivative term improves stability of the system and helps the system reach the set point more quickly. Choosing the right gain constants is crucial to optimal system response. To find the optimal gain constants Kp, Ki and Kd, we conducted phantom and in vivo experiments. Kp, Ki and Kd values were changed empirically. Heating tests were performed for each set of Kp, Ki and Kd. Rise time, over-shooting and settling time of each set were calculated to assess the performance of the PID control system, Figure 5.3. Rise time (t_r) is the time required for response to rise from 0% to 100%; maximum overshoot is maximum value of the response from threshold value; settling time is the time required for response to reach and stay within a range of threshold value, usually between 2% and 5%.

Tests were performed in 1.5 T Siemens Espree scanner using bSSFP sequence with the following scan parameters: TR/TE, 2.54/1.27 ms; flip angle, 45 °; slice thickness, 6 mm; field of view, 340x340 mm; matrix, 192x192. Change in flip angle and RF pulse with was reported as percentage. As a precaution, not to reach high temperature values at beginning of scan, MRI started with 50% of flip angle (22.5 °) and adjusted by PID control to reach the preset threshold value.

5.2.3 RF Feedback System

Incorporating a fiber optic temperature probe prevented exchanging catheters over the guidewire because of fiber optic connector size. Therefore an alternative method was implemented to measure RF induced heating on the guidewire. Since RF induced heating is correlated with RF coupling between guidewire and RF transmitter of MRI scanner, measuring the RF coupled power on the guidewire allowed us to predict heating on the guidewire.

A directional coupler was used to direct RF coupled power into RF power meter (logarithmic amplifier) then it is converted in to a DC voltage. DC current is then converted to optic signal and transferred outside the MRI room, Figure 5.4. In control room, optic signal is converted back to DC voltage and displayed on monitor. After preliminary experiment, measured DC voltages were compared to RF induced heating on the guidewire for various flip angles.

5.3 Results

Increasing RF pulse width resulted in increased TR, Table 5.1. Increasing the TR reduces the number of RF pulses per second and subsequently reduces the SAR and heating.

Table 5.2 summarizes the combined effect of flip angle and RF pulse width on guidewire heating both in phantom and in vivo.

SNR of blood and heart tissue was calculated from images acquired in healthy

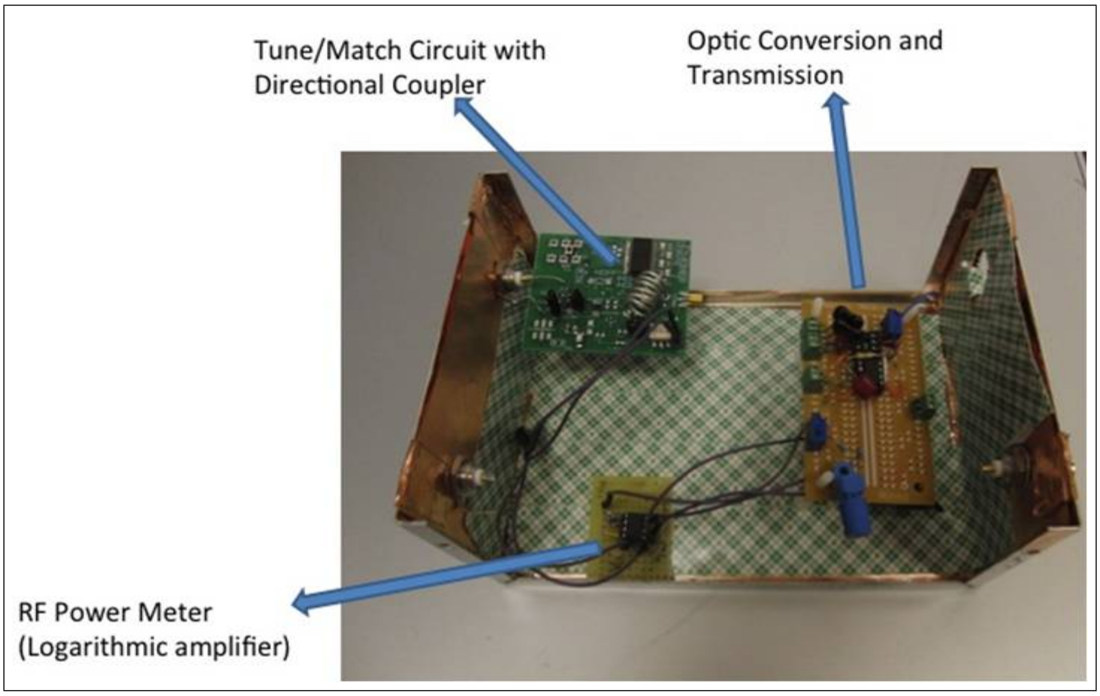

Figure 5.4 Tune/match circuitry with directional coupler, RF power meter and optic coupler is shielded with box to prevent external RF interaction with circuitries.

Table 5.1
Increase in RF pulse width results in increase of TR.

FR Pulse Width(μ)	TR (msec)
600	2.88
1800	4.08
3000	5.28

volunteers, Figure 5.5 Table 5.3 .

5.3.1 Temperature Feedback System to Control Scan Parameters : A PID Controller

First guidewire was tested without feedback control in phantom. Baseline temperature was 18.2 °C before the scan and maximum temperature was 36 °C at the hottest spot of the guidewire after a one minute scan, Figure 5.6. Next, temperature measurements were obtained for the test setup with feedback control system which

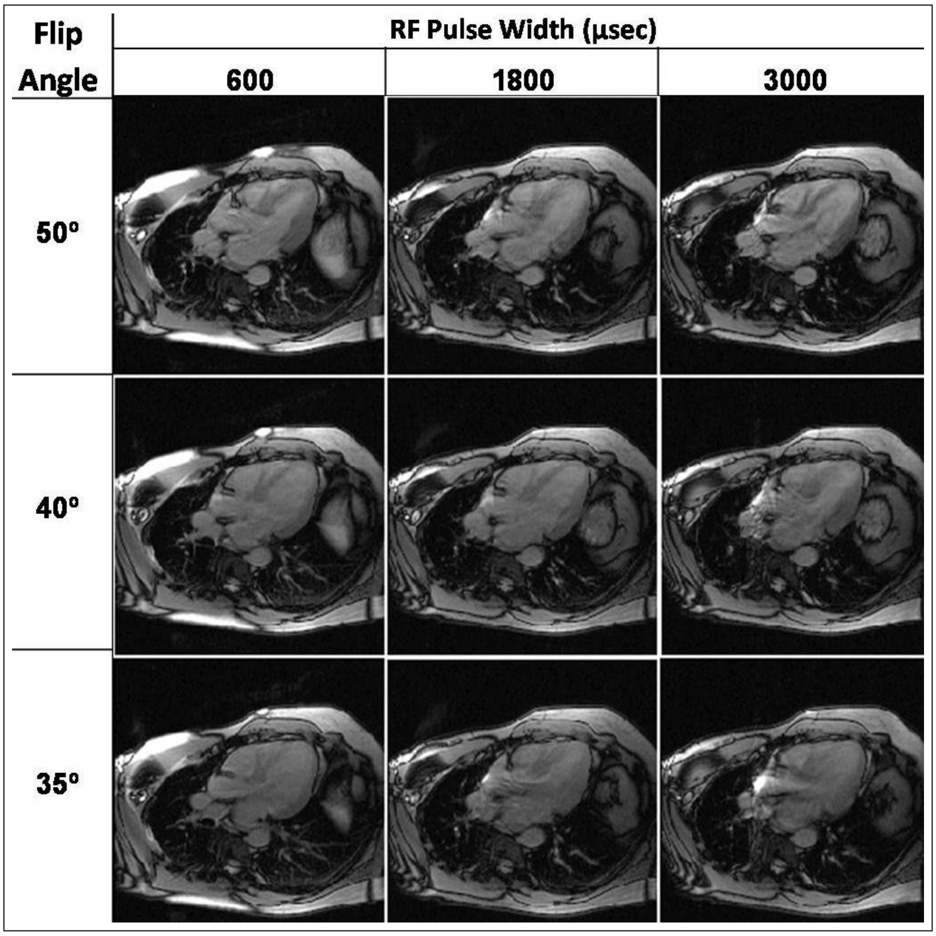

Figure 5.5 MRI heart images of healthy volunteers were acquired using a bSSFP sequence with flip angle 50,40, and 35 and RF pulse width 600 μsec, 1800 μsec, and 3000 μsec.

Table 5.2

Normalized RF-heating results for flip angle 50 °, 45 °, and 30 ° and RF pulse widths 600 μsec, 1800 μsec, and 3000 μsec. Results are normalized within the phantom set and within the in vivo set.

Phantom	FR Pulse Width(μ)		
Flip angle	600	1800	3000
50	100%	21%	9%
40	69%	14%	6%
35	50%	11%	4%
In Vivo	FR Pulse Width(μ)		
Flip angle	600	1800	3000
50	100%	27%	12%
40	69%	14%	7%
35	46%	13%	4%

adjusted the flip angle in real-time. Threshold temperature was set to 25 °C. Table 5.4 shows the rise time, overshoot and settling time with respect to the gain constants Kp, Ki, Kd. Figure 5.7 shows an example graph of temperature and flip angle changes for Kp=1, Ki=0.1, Kd=0.1.

In vivo heating tests results showed a 4 °C temperature increase, Figure 5.8. Baseline and maximum temperatures were 34.5 °C and 38.5 °C, respectively. Threshold was set to 36 °C to test the feedback control system. The rise time, overshoot and settling time with respect to the gain constants Kp, Ki, Kd were presented in Table 5.4. Figure 5.9 shows an example graph of temperature and flip angle changes for Kp=1, Ki=0.1, Kd=0.1. Ki component caused a significant oscillation in temperature, therefore we eliminated its contribution and tested the system with Kp=1, Ki=0, Kd=1 which yield the response in Figure 5.10. Oscillations are eliminated but still temperature overshoots beyond the desired threshold value that may cause heat damage in tissue. Thus, we modified the algorithm of PID controller. The Kp value was set to 0.5 for the temperature values below the threshold temperature and set to 4 for the temperature values above the threshold temperature. This modification prevent the overshooting but increased the undershooting, Figure 5.11. This settings was then testing during guidewire manipulation. Operator advanced and withdrew the guidewire

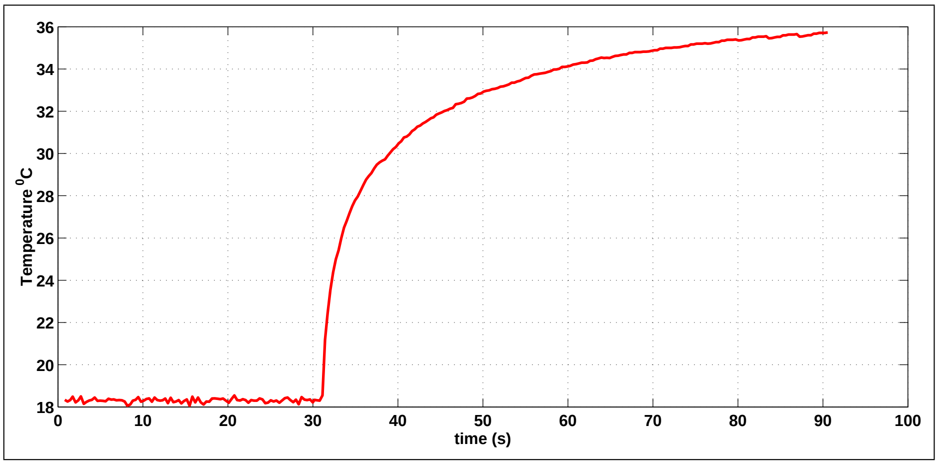

Figure 5.6 After a 30 second baseline temperature recording, a one minute MRI scan was performed to measure temperature increase of guidewire in phantom.

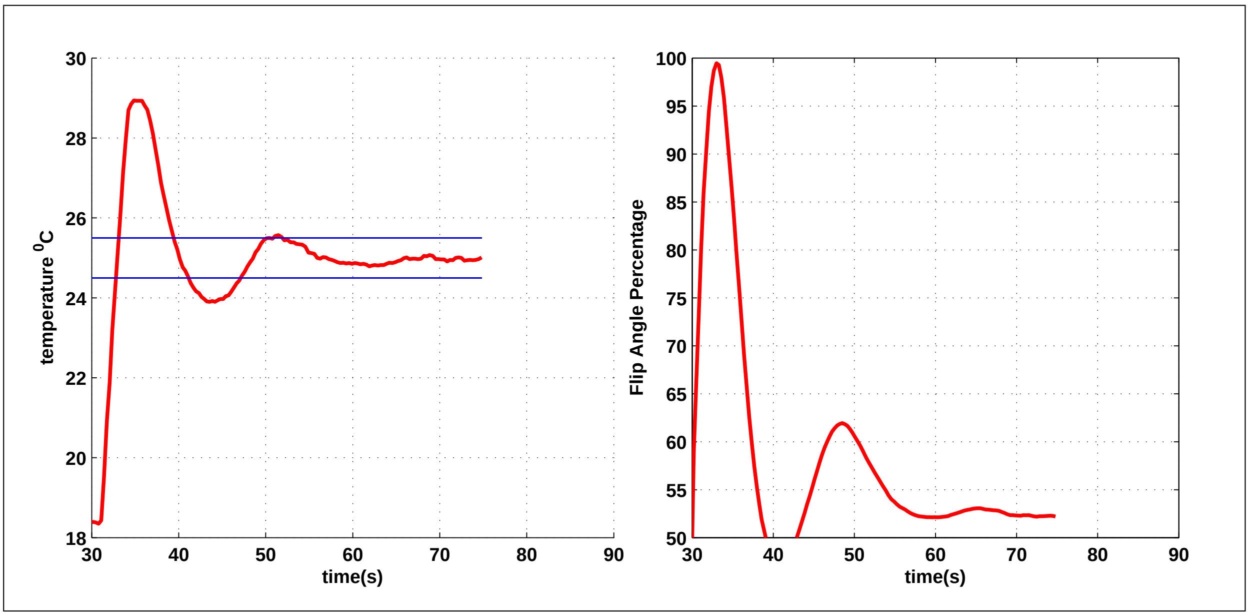

Figure 5.7 Controlling the flip angle using the following gain constants Kp=1, Ki=0.1, Kd=0.1, in phantom.

Table 5.3
SNR values of blood and heart tissue for varying flip angle and RF pulse width.

Blood SNR	FR Pulse Width(μ)		
Flip angle	600	1800	3000
50	108	105	105
40	77	86	65
35	81	81	65
Tissue SNR	FR Pulse Width(μ)		
Flip angle	600	1800	3000
50	65	76	76
40	54	70	53
35	59	66	60

within 5 cm insertion length; temperature and flip angle percentages were recorded, Figure 5.12. The system responded quickly for temperature increases to prevent high heating.

5.3.2 RF Feedback System

There is a correlation between heating and measured RF power, Figure 5.13. Reducing the flip angle which means reduction in RF transmitted power resulted in decrease of DC voltage.

5.4 Discussion

In this study, we evaluated effects RF pulse width and flip angle on imaging and heating. Changing the RF pulse with resulted in higher TR values and heat reduction. For flip angle 50°, three times and five times longer RF pulse widths reduced the RF heating 5 fold and 10 fold respectively, while no significant reduction was observed in blood and tissue SNR. Even though time resolution is reduced, this is a significant

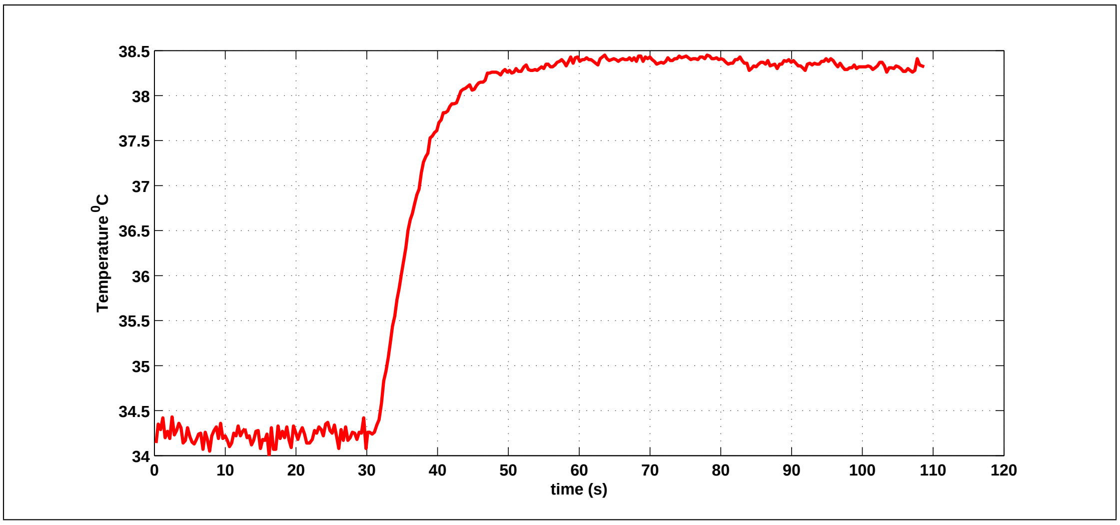

Figure 5.8 No feedback control in vivo heating test.

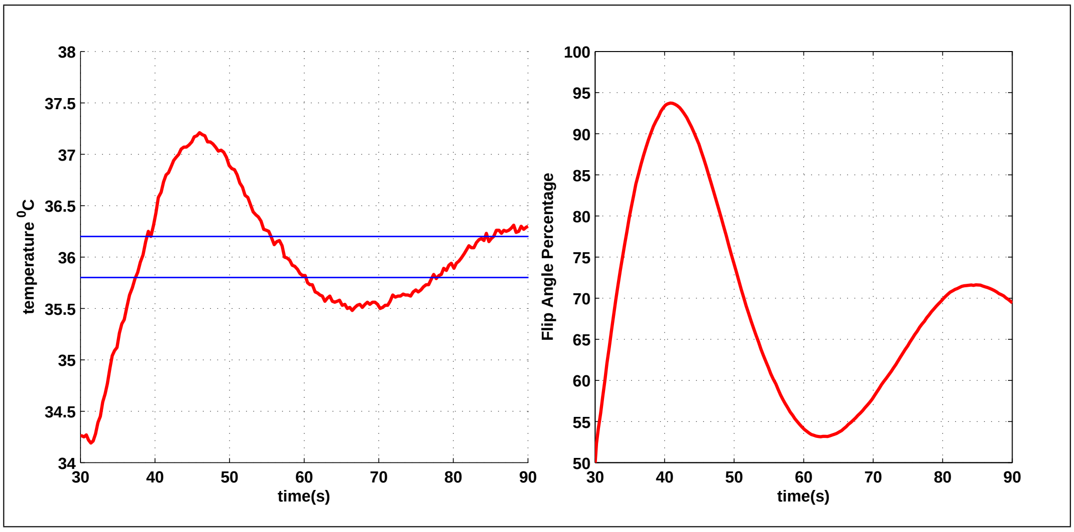

Figure 5.9 Controlling the flip angle using the following gain constants Kp=1, Ki=0.1, Kd=0.1. Integral gain constant (Ki) introduced an osculations and increased the settling time drastically.

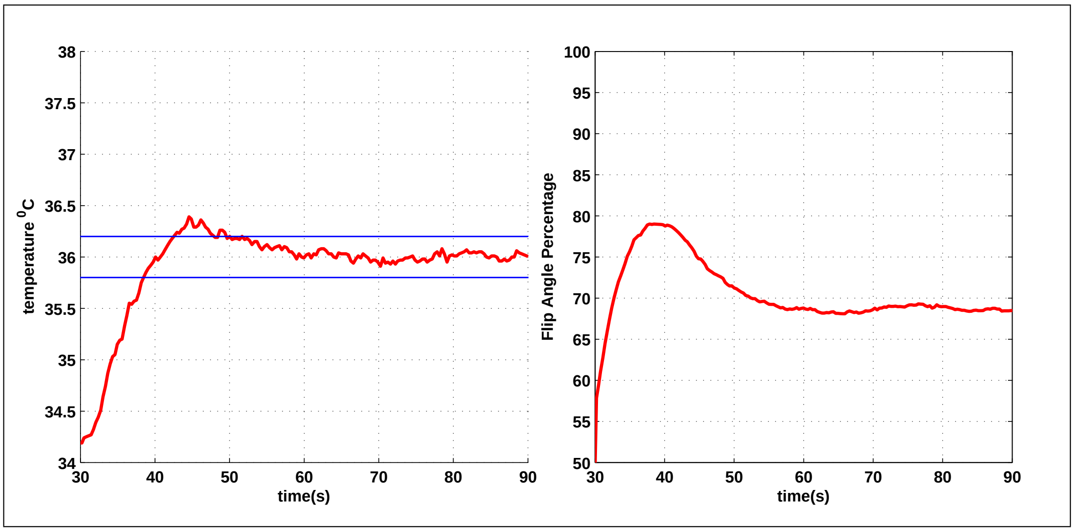

Figure 5.10 Temperature and flip angle percentage using the following gain constants Kp=1, Ki=0, Kd=1. Oscillations are eliminated but still there is a temperature overshoot.

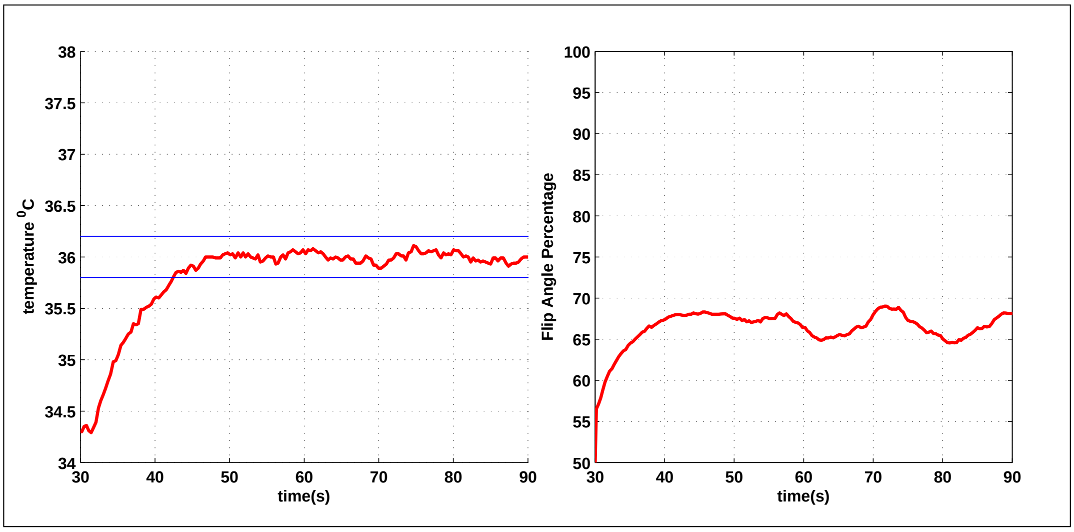

Figure 5.11 Temperature and flip angle percentage using fix Kd=1 and adoptive Kd (0.5 for temperature values below the threshold and 4 for the values above the threshold). The settling time is longer but on overshooting is observed.

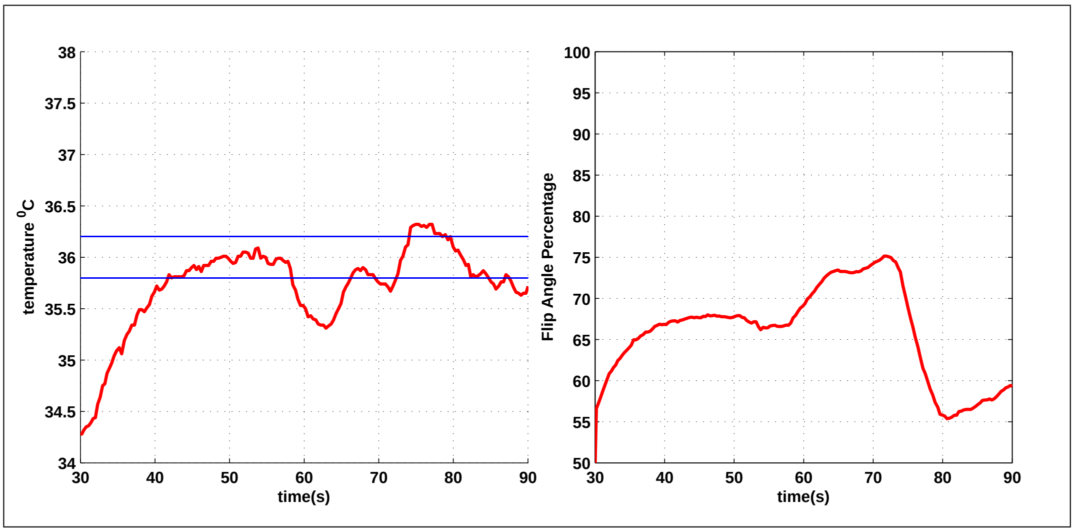

Figure 5.12 Kp=0.5/4, Kd=1 was tested in vivo. Operator manipulated guidewire during in vivo MRI scan.

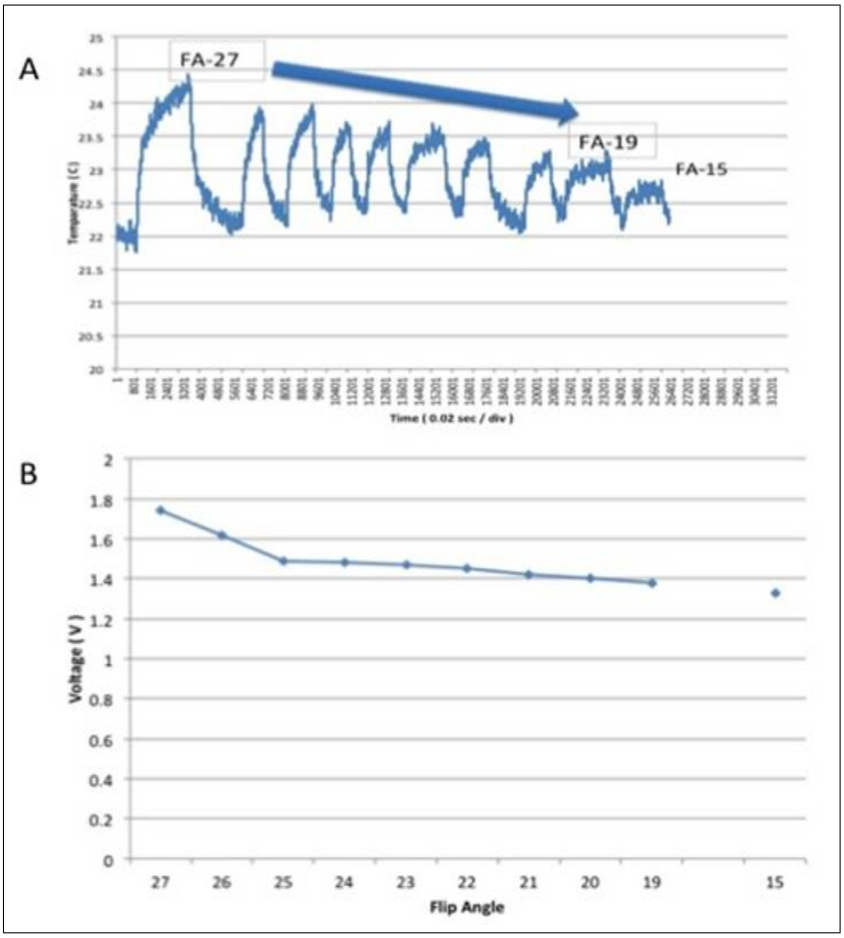

Figure 5.13 RF controlled scan parameters. (A) Real time temperature was recorded during a consecutive MRI scan by decreasing flip angle from 27° to 15°. (B) RF power was measured and converted to DC voltage and DC voltage for each flip angle excitation is plotted.

Table 5.4
The rise time, overshoot and settling time with respect to the various gain constants Kp, Ki, Kd.

Gain constants			Phantom			In Vivo		
Kp	Ki	Kd	Rise time (s)	Over-shoot (C)	Settling time (s)	Rise time (s)	Over-shoot (C)	Settling time (s)
1	0	0	4.2	2.2	11.1	9.7	0.45	21.5
0.5	0	0	7.1	1.5	10.9	10.7	0.37	20.5
0.1	0	0	23.8	0.7	over 60	over 60	0	over 60
1	0	1	3.6	0.8	11.1	11	0.39	19.6
1	0	0.1	3.7	2.6	9.8	10.7	0.38	22.8
1	0.1	1	3.3	1.79	12.7	7.9	1.1	60
1	0.1	0.1	3	3.94	22.2	8.4	1.2	60
0.5/2	0	1				8.8	0.39	21.6
0.5/4	0	1				16.8	0.1	12.5

improvement in terms of RF safety. Likewise, reducing the flip angle from resulted in significant heat reduction while SNR of blood and tissue didn't changed significantly. In overall, 25 fold temperature reduction can be achieved by increasing the RF pulse width and decreasing the flip angle while meeting the SNR requirement for safe procedures.

Next, we implemented a PID controller altering the flip angle to optimize scan parameters in real-time. Gain constants Kp, Ki, Kd were changed and performance of the each configuration was evaluated by calculating the output response characteristics (rise time, overshooting temperature and settling time). Integral (I) component of PID caused oscillations and increased the settling time, thus we eliminated the I component. Gain constant of proportional component determined how quickly output reaches to the threshold value. The higher Kp values resulted in short rise time but higher overshooting. Derivative component prevented the higher overshooting while still keeping the short rise time. Kp and Kd gain constants were used for final controller which is a PD-controller. For the safety of the patient we would like to have undershooting system instead of overshooting systems. Kp parameter was adjusted based on the real-time temperature value; it was set to 0.5 for the temperature values below threshold that increase the rise time but reduce the overshoot and it was switched to 4 to bring the higher temperatures down quickly. This configuration ensured the patient safety during MRI scan.

Finally, we proposed and alternative method as a feedback to PID controller. For the devices which is impossible to place a temperature probe in, RF power coupled with interventional device can be measured and used as a feedback. In our study, we used a RF directional coupler and RF power meter to measure the RF power coupled with guidewire. RF power measurements were closely correlated with the heating measurements of the device. Other alternatives could be imaging based device safety monitoring [104] or measuring eddy current on the wire [84].

In conclusion, a control system is introduced that dynamically adjusts scan parameters for patient safety. Control system was tested and validated for flip angle adjustment using temperature values in real-time. Also, beside the temperature and RF power measurements, any other parameters, such as device imaging to measure the eddy currents, can be used as a feedback.

6. CONCLUSION

This dissertation introduces a clinical grade active guidewire design for MRI-guided interventional procedures. Comprehensive bench-top and in vivo testing were performed to evaluate the safety and effectiveness of the guidewire. A PID controller using real-time temperature data of the guidewire to dynamically adjust scan parameters was also implemented in order to ensure patient safety.

The first part of the dissertation discusses the design of a guidewire based on a loopless antenna. A miniature fiberoptic temperature probe was integrated into the guidewire design for real-time temperature monitoring during the MRI-guided interventional procedure. The addition of the fiber-optic probe into the design did not compromise the mechanical integrity of the guidewire or affect device visualization. Advancing and withdrawing the temperature probe in a lumen allowed for a heat distribution of the entire guidewire to be obtained, which enabled rapid testing of guidewire prototypes. A solenoid coil attachment at the distal tip manipulated the current distribution at the tip and created a distinct tip signal. The solenoid coil changed the hotspot location of the guidewire from the tip to 2.5 cm proximal of the tip, which corresponds to the proximal end of the solenoid coil. That modification allowed for the creation of a curved tip and the ability to position the temperature probe at the hotspot, without compromising the mechanical integrity of the guidewire. The initial heating and imaging tests conducted in swine models to assess the feasibility of the use of the guidewire in clinical applications were promising.

The second part of this dissertation discusses the bench-top testing that was performed to evaluate the safety and effectiveness of the guidewire. A series of mechanical tests were conducted on both MRI active guidewire and its commercial counterparts. The results were within the acceptance criteria for all of the tests that were conducted. The tapered inner nitinol rod, the spiral-cut hypotube, and thermoplastic materials were the key components of the design that improved the mechanical integrity of the guidewire. Next, image artifacts and distortion caused by using the active guidewire in MRI were characterized in a phantom. The maximum artifact size was 6.5 mm, which was a relatively small artifact that should not significantly distort the anatomical image. The SNR of the image obtained by the active guidewire was calculated from signal magnitude images. Both the tip and shaft had acceptable SNR and conspicuity. RF heating testing was conducted in a gel phantom prepared according to the ASTM-2182 standard. The inner and outer temperature measurements were compared; the inner temperature measurement was higher than the outer temperature measurement. The physical location of the heat distribution was identified by marking the temperature probe during guidewire manufacturing. In phantom experiments, maximum heating was observed within a couple of millimeters distally from the proximal end of solenoid coil. The heat distribution around the close vicinity of the guidewire was acquired, and the results showed that there were not any other heated points in the phantom. Based on the comprehensive RF heating tests conducted, crucial RF problem of the active guidewire was identified and addressed. These methods can be adapted and used for any active device testing. Finally, the electrical safety of the active guidewire was also studied and electrical safety concerns were addressed.

In this part of the dissertation, a feasibility study complying with GLP standard was conducted in a swine model to evaluate RF safety, imaging and mechanical performance of the guidewire. During the intended use, significant temperature increases were observed only when the guidewire tip was positioned around the groin area. One reason for high heating could be the configuration of the guidewire with respect to the sheath that prevents the blood cooling effect. Another reason could be the superficial position of the guidewire, which increased E-field coupling [105]. The guidewire position on the table also dramatically impacted heating. Therefore, the guidewire position during right/left heart catheterization must be carefully monitored. A possible solution to decreasing RF heating during catheterization is a saline flush, which is a standard procedure in many catheterization laboratories used to prevent blood clots. Precise heating measurements around the hottest spot of the guidewire helped to identify the exact physical location of the hot spot. The image quality of the guidewire was sufficient to navigate the guidewire through the vascular structure. Furthermore, the mechanical characteristics of the guidewire were found to be adequate by experienced interventional cardiologists. Overall, the findings of the in vivo study provided valuable insight for the safe use of guidewires in humans. In our group at NHLBI, Ratnayaka [33] conducted right heart catheterization in humans using a passive catheter without a guidewire and showed the feasibility of cardiovascular interventional MRI in clinic. Combination of Ratnayaka's study, together with the findings of our study detailed in this dissertation will enable us to conduct the first right/left heart catheterization using the active guidewire in human.

The final part of the dissertation discusses another safety measure which controls the RF deposit power and consequently controls the RF heating. Since RF heating is directly correlated with the magnitude and shape of the flip angle, the effect of flip angle manipulation on heating and imaging was investigated. The results showed that without significantly compromising image quality, a dramatic heat decrease (25-fold) can be achieved by changing the flip angle and the RF pulse width. This significant reduction in heating ensures patient safety during the MRI procedure. Because higher flip angles results in higher SNR, but lower flip angles are necessary for RF safety, it was necessary to conduct flip angle optimization in real time. A PID controller using real-time temperature data of the guidewire to adjust the flip angle dynamically was implemented. Proper gain constants for controller and an adoptive algorithm yielded a balanced combination of heating and imaging quality during animal experiments. In addition to the temperature feedback that requires insertion of fiberoptic probe into the guidewire, the feasibility of RF power measurement as an alternative feedback mechanism was also tested.

In conclusion, for this study, an active guidewire for MRI-guided intravascular procedures was designed and tested. The RF safety of the guidewire was ensured by identifying and monitoring the hottest spot of the guidewire in real-time. A feasibility study complying with the GLP standard showed the safety and effectiveness of the guidewire use in right and left heart catheterization.

REFERENCES

1. Pruessmann, K. P., M. Weiger, M. B. Scheidegger, and P. Boesiger, "Sense: sensitivity encoding for fast mri," *Magn Reson Med*, Vol. 42, pp. 952–62, Nov 1999.

2. Griswold, M. A., P. M. Jakob, R. M. Heidemann, M. Nittka, V. Jellus, J. Wang, B. Kiefer, and A. Haase, "Generalized autocalibrating partially parallel acquisitions (grappa)," *Magn Reson Med*, Vol. 47, pp. 1202–10, Jun 2002.

3. Guttman, M. A., C. Ozturk, A. N. Raval, V. K. Raman, A. J. Dick, R. DeSilva, P. Karmarkar, R. J. Lederman, and E. R. McVeigh, "Interventional cardiovascular procedures guided by real-time mr imaging: an interactive interface using multiple slices, adaptive projection modes and live 3d renderings," *J Magn Reson Imaging*, Vol. 26, pp. 1429–35, Dec 2007.

4. Busch, M., A. Bornstedt, M. Wendt, J. L. Duerk, J. S. Lewin, and D. Gronemeyer, "Fast "real time" imaging with different k-space update strategies for interventional procedures," *Jmri-Journal of Magnetic Resonance Imaging*, Vol. 8, pp. 944–954, Jul-Aug 1998.

5. Almen, T., "The etiology of contrast medium reactions," *Investigative radiology*, Vol. 29 Suppl 1, pp. S37–45, May 1994.

6. Modan, B., L. Keinan, T. Blumstein, and S. Sadetzki, "Cancer following cardiac catheterization in childhood," *Int J Epidemiol*, Vol. 29, pp. 424–8, Jun 2000.

7. Kleinerman, R. A., "Cancer risks following diagnostic and therapeutic radiation exposure in children," *Pediatr Radiol*, Vol. 36 Suppl 14, pp. 121–5, Sep 2006.

8. Andreassi, M. G., L. Ait-Ali, N. Botto, S. Manfredi, G. Mottola, and E. Picano, "Cardiac catheterization and long-term chromosomal damage in children with congenital heart disease," *Eur Heart J*, Vol. 27, pp. 2703–8, Nov 2006.

9. Bartels, L. W., and C. J. Bakker, "Endovascular interventional magnetic resonance imaging," *Phys Med Biol*, Vol. 48, pp. R37–64, Jul 21 2003.

10. Ratnayaka, K., C. E. Saikus, A. Z. Faranesh, J. A. Bell, I. M. Barbash, O. Kocaturk, C. A. Reyes, M. Sonmez, W. H. Schenke, V. J. Wright, M. S. Hansen, M. C. Slack, and R. J. Lederman, "Closed-chest transthoracic magnetic resonance imaging-guided ventricular septal defect closure in swine," *J Am Coll Cardiol Intv*, Vol. 4, pp. 1326–1334, December 1, 2011 2011.

11. Rickers, C., R. T. Seethamraju, M. Jerosch-Herold, and N. M. Wilke, "Magnetic resonance imaging guided cardiovascular interventions in congenital heart diseases," *J Interv Cardiol*, Vol. 16, pp. 143–7, Apr 2003.

12. Spuentrup, E., A. Ruebben, T. Schaeffter, W. J. Manning, R. W. Gunther, and A. Buecker, "Magnetic resonance–guided coronary artery stent placement in a swine model," *Circulation*, Vol. 105, pp. 874–9, Feb 19 2002.

13. Vergara, G. R., L. McMullan, and N. F. Marrouche, "Right atrial perforation at the end of an atrial fibrillation ablation procedure," *Europace*, Vol. 13, pp. 901–902, Jun 2011.

14. Nordbeck, P., K. H. Hiller, F. Fidler, M. Warmuth, N. Burkard, M. Nahrendorf, P. M. Jakob, H. H. Quick, G. Ertl, W. R. Bauer, and O. Ritter, "Feasibility of contrast-enhanced and nonenhanced mri for intraprocedural and postprocedural lesion visualization in interventional electrophysiology animal studies and early delineation of isthmus ablation lesions in patients with typical atrial flutter," *Circulation-Cardiovascular Imaging*, Vol. 4, pp. 282–U136, May 2011.

15. Hoffmann, B. A., A. Koops, T. Rostock, K. Mullerleile, D. Steven, R. Karst, M. U. Steinke, I. Drewitz, G. Lund, S. Koops, G. Adam, and S. Willems, "Interactive real-time mapping and catheter ablation of the cavotricuspid isthmus guided by magnetic resonance imaging in a porcine model," *Eur Heart J*, Vol. 31, pp. 450–456, Feb 2010.

16. Dick, A. J., M. A. Guttman, V. K. Raman, D. C. Peters, B. S. Pessanha, J. M. Hill, S. Smith, G. Scott, E. R. McVeigh, and R. J. Lederman, "Magnetic resonance fluoroscopy allows targeted delivery of mesenchymal stem cells to infarct borders in swine," *Circulation*, Vol. 108, pp. 2899–904, Dec 9 2003.

17. Raval, A. N., P. V. Karmarkar, M. A. Guttman, C. Ozturk, S. Sampath, R. DeSilva, R. J. Aviles, M. Xu, V. J. Wright, W. H. Schenke, O. Kocaturk, A. J. Dick, V. K. Raman, E. Atalar, E. R. McVeigh, and R. J. Lederman, "Real-time magnetic resonance imaging-guided endovascular recanalization of chronic total arterial occlusion in a swine model," *Circulation*, Vol. 113, pp. 1101–7, Feb 28 2006.

18. Krueger, J. J., P. Ewert, S. Yilmaz, D. Gelernter, B. Peters, K. Pietzner, A. Bornstedt, B. Schnackenburg, H. Abdul-Khaliq, E. Fleck, E. Nagel, F. Berger, and T. Kuehne, "Magnetic resonance imaging-guided balloon angioplasty of coarctation of the aorta: a pilot study," *Circulation*, Vol. 113, pp. 1093–100, Feb 28 2006.

19. McVeigh, E. R., M. A. Guttman, R. J. Lederman, M. Li, O. Kocaturk, T. Hunt, S. Kozlov, and K. A. Horvath, "Real-time interactive mri-guided cardiac surgery: aortic valve replacement using a direct apical approach," *Magn Reson Med*, Vol. 56, pp. 958–64, Nov 2006.

20. Horvath, K. A., D. Mazilu, M. Guttman, A. Zetts, T. Hunt, and M. Li, "Midterm results of transapical aortic valve replacement via real-time magnetic resonance imaging guidance," *Journal of Thoracic and Cardiovascular Surgery*, Vol. 139, pp. 424–430, Feb 2010.

21. Kahlert, P., N. Parohl, J. Albert, L. Schafer, R. Reinhardt, G. M. Kaiser, I. McDougall, B. Decker, B. Plicht, R. Erbel, H. Eggebrecht, M. E. Ladd, and H. H. Quick, "Towards real-time cardiovascular magnetic resonance guided transarterial corevalve implantation: in vivo evaluation in swine," *Journal of Cardiovascular Magnetic Resonance*, Vol. 14, Mar 27 2012.

22. Duerk, J. L., J. S. Lewin, M. Wendt, and C. Petersilge, "Remember true fisp? a high snr, near 1-second imaging method for t2-like contrast in interventional mri at .2 t," *Jmri-Journal of Magnetic Resonance Imaging*, Vol. 8, pp. 203–208, Jan-Feb 1998.

23. Glover, G. H., "Simple analytic spiral k-space algorithm," *Magnetic Resonance in Medicine*, Vol. 42, pp. 412–415, Aug 1999.

24. Cline, H. E., X. L. Zong, and N. Gai, "Design of a logarithmic k-space spiral trajectory," *Magnetic Resonance in Medicine*, Vol. 46, pp. 1130–1135, Dec 2001.

25. Nayak, K. S., B. A. Hargreaves, B. S. Hu, D. G. Nishimura, J. M. Pauly, and C. H. Meyer, “Spiral balanced steady-state free precession cardiac imaging,” *Magn Reson Med*, Vol. 53, pp. 1468–73, Jun 2005.

26. Boll, D. T., E. M. Merkle, D. M. Seaman, R. C. Gilkeson, A. P. Larson, O. P. Simonetti, J. L. Duerk, and J. S. Lewin, “Comparison of ecg-gated rectilinear vs. real-time radial k-space sampling schemes in cine true-fisp cardiac mri,” *J Cardiovasc Magn Reson*, Vol. 6, no. 4, pp. 793–802, 2004.

27. Wu, V., I. M. Barbash, K. Ratnayaka, C. E. Saikus, M. Sonmez, O. Kocaturk, R. J. Lederman, and A. Z. Faranesh, “Adaptive noise cancellation to suppress electrocardiography artifacts during real-time interventional mri,” *Journal of Magnetic Resonance Imaging*, Vol. 33, pp. 1184–1193, May 2011.

28. Odille, F., C. Pasquier, R. Abacherli, P. A. Vuissoz, G. P. Zientara, and J. Felblinger, “Noise cancellation signal processing method and computer system for improved real-time electrocardiogram artifact correction during mri data acquisition,” *Ieee Transactions on Biomedical Engineering*, Vol. 54, pp. 630–640, Apr 2007.

29. Oduneye, S. O., L. Biswas, S. Ghate, V. Ramanan, J. Barry, A. Laish-FarKash, E. Kadmon, T. Z. Shwiri, E. Crystal, and G. A. Wright, “The feasibility of endocardial propagation mapping using magnetic resonance guidance in a swine model, and comparison with standard electroanatomic mapping,” *Ieee Transactions on Medical Imaging*, Vol. 31, pp. 977–983, Apr 2012.

30. Kim, K., “Toward cardiac electrophysiological mapping based on micro-tesla nmr: a novel modality for localizing the cardiac reentry,” *Aip Advances*, Vol. 2, Jun 2012.

31. Chinchapatnam, P., M. R. Ginks, M. Sermesant, K. Rhode, S. Arridge, P. D. Lambiase, J. Bostock, C. A. Rinaldi, and R. Razavi, “A novel electrophysiological model using hybrid x-ray/mri and non-contact mapping to estimate electrical recruitability of myocardial tissue,” *Circulation*, Vol. 118, pp. S617–S617, Oct 28 2008.

32. Dukkipati, S. R., R. Mallozzi, E. J. Schmidt, G. Holmvang, A. d’Avila, R. Guhde, R. D. Darrow, G. Slavin, M. Fung, Z. Malchano, G. Kampa, J. D. Dando, C. McPherson, T. K. Foo, J. N. Ruskin, C. L. Dumoulin, and V. Y. Reddy, “Electroanatomic mapping of the left ventricle in a porcine model of chronic myocardial infarction with magnetic resonance-based catheter tracking,” *Circulation*, Vol. 118, pp. 853–62, Aug 19 2008.

33. Ratnayaka, K., A. Z. Faranesh, M. S. Hansen, A. M. Stine, M. Halabi, I. M. Barbash, W. H. Schenke, V. J. Wright, L. P. Grant, P. Kellman, O. Kocaturk, and R. J. Lederman, “Real-time mri-guided right heart catheterization in adults using passive catheters,” *Eur Heart J*, Vol. 34, pp. 380–389, Feb 2013.

34. Razavi, R., D. L. G. Hill, S. F. Keevil, M. E. Miquel, V. Muthurangu, S. Hegde, K. Rhode, M. Barnett, J. van Vaals, D. J. Hawkes, and E. Baker, “Cardiac catheterisation guided by mri in children and adults with congenital heart disease,” *Lancet*, Vol. 362, pp. 1877–1882, Dec 6 2003.

35. Muthurangu, V., D. Atkinson, M. Sermesant, M. E. Miquel, S. Hegde, R. Johnson, R. Andriantsimiavona, A. M. Taylor, E. Baker, R. Tulloh, D. Hill, and R. S. Razavi, “Measurement of total pulmonary arterial compliance using invasive pressure monitoring and mr flow quantification during mr-guided cardiac catheterization,” *American Journal of Physiology-Heart and Circulatory Physiology*, Vol. 289, pp. H1301–H1306, Sep 2005.

36. Kuehne, T., S. Yilmaz, C. Meinus, P. Moore, M. Saeed, O. Weber, C. B. Higgins, T. Blank, E. Elsaesser, B. Schnackenburg, P. Ewert, P. E. Lange, and E. Nagel, "Magnetic resonance imaging-guided transcatheter implantation of a prosthetic valve in aortic valve position: Feasibility study in swine," *J Am Coll Cardiol*, Vol. 44, pp. 2247–9, Dec 7 2004.

37. Unal, O., J. Li, W. Cheng, H. Yu, and C. M. Strother, "Mr-visible coatings for endovascular device visualization," *J Magn Reson Imaging*, Vol. 23, pp. 763–9, May 2006.

38. Omary, R. A., O. Unal, D. S. Koscielski, R. Frayne, F. R. Korosec, C. A. Mistretta, C. M. Strother, and T. M. Grist, "Real-time mr imaging-guided passive catheter tracking with use of gadolinium-filled catheters," *J Vasc Interv Radiol*, Vol. 11, pp. 1079–85, Sep 2000.

39. Bakker, C. J., R. M. Hoogeveen, J. Weber, J. J. van Vaals, M. A. Viergever, and W. P. Mali, "Visualization of dedicated catheters using fast scanning techniques with potential for mr-guided vascular interventions," *Magn Reson Med*, Vol. 36, pp. 816–20, Dec 1996.

40. Mekle, R., E. Hofmann, K. Scheffler, and D. Bilecen, "A polymer-based mr-compatible guidewire: a study to explore new prospects for interventional peripheral magnetic resonance angiography (ipmra)," *J Magn Reson Imaging*, Vol. 23, pp. 145–55, Feb 2006.

41. Buecker, A., E. Spuentrup, T. Schmitz-Rode, S. Kinzel, J. Pfeffer, C. Hohl, J. J. van Vaals, and R. W. Gunther, "Use of a nonmetallic guide wire for magnetic resonance-guided coronary artery catheterization," *Invest Radiol*, Vol. 39, pp. 656–60, Nov 2004.

42. Krueger, S., S. Schmitz, S. Weiss, D. Wirtz, M. Linssen, H. Schade, N. Kraemer, E. Spuentrup, G. Krombach, and A. Buecker, "An mr guidewire based on micropultruded fiber-reinforced material," *Magn Reson Med*, Vol. 60, pp. 1190–6, Nov 2008.

43. Rubin, D. L., A. V. Ratner, and S. W. Young, "Magnetic susceptibility effects and their application in the development of new ferromagnetic catheters for magnetic resonance imaging," *Invest Radiol*, Vol. 25, pp. 1325–32, Dec 1990.

44. Zuehlsdorff, S., R. Umathum, S. Volz, P. Hallscheidt, C. Fink, W. Semmler, and M. Bock, "Mr coil design for simultaneous tip tracking and curvature delineation of a catheter," *Magn Reson Med*, Vol. 52, pp. 214–8, Jul 2004.

45. Bock, M., S. Muller, S. Zuehlsdorff, P. Speier, C. Fink, P. Hallscheidt, R. Umathum, and W. Semmler, "Active catheter tracking using parallel mri and real-time image reconstruction," *Magn Reson Med*, Vol. 55, pp. 1454–9, Jun 2006.

46. Feng, L., C. L. Dumoulin, S. Dashnaw, R. D. Darrow, R. Guhde, R. L. Delapaz, P. L. Bishop, and J. Pile-Spellman, "Transfemoral catheterization of carotid arteries with real-time mr imaging guidance in pigs," *Radiology*, Vol. 234, pp. 551–7, Feb 2005.

47. Kuehne, T., R. Fahrig, and K. Butts, "Pair of resonant fiducial markers for localization of endovascular catheters at all catheter orientations," *J Magn Reson Imaging*, Vol. 17, pp. 620–4, May 2003.

48. Quick, H. H., M. O. Zenge, H. Kuehl, G. Kaiser, S. Aker, S. Massing, S. Bosk, and M. E. Ladd, "Interventional magnetic resonance angiography with no strings attached: wireless active catheter visualization," *Magn Reson Med*, Vol. 53, pp. 446–55, Feb 2005.

49. Eggers, H., S. Weiss, P. Boernert, and P. Boesiger, "Image-based tracking of optically detunable parallel resonant circuits," *Magn Reson Med*, Vol. 49, pp. 1163–74, Jun 2003.

50. Wong, E. Y., Q. Zhang, J. L. Duerk, J. S. Lewin, and M. Wendt, “An optical system for wireless detuning of parallel resonant circuits,” *J Magn Reson Imaging*, Vol. 12, pp. 632–8, Oct 2000.

51. Ocali, O., and E. Atalar, “Intravascular magnetic resonance imaging using a loopless catheter antenna,” *Magn Reson Med*, Vol. 37, pp. 112–8, Jan 1997.

52. Qian, D., A. M. El-Sharkawy, E. Atalar, and P. A. Bottomley, “Interventional mri: tapering improves the distal sensitivity of the loopless antenna,” *Magn Reson Med*, Vol. 63, pp. 797–802, Mar 2010.

53. Karmarkar, P. V., D. L. Kraitchman, I. Izbudak, L. V. Hofmann, L. C. Amado, D. Fritzges, R. Young, M. Pittenger, J. W. M. Bulte, and E. Atalar, “Mr-trackable intramyrocardial injection catheter,” *Magnetic Resonance in Medicine*, Vol. 51, pp. 1163–1172, Jun 2004.

54. Kocaturk, O., A. H. Kim, C. E. Saikus, M. A. Guttman, A. Z. Faranesh, C. Ozturk, and R. J. Lederman, “Active two-channel 0.035 ” guidewire for interventional cardiovascular mri,” *Journal of Magnetic Resonance Imaging*, Vol. 30, pp. 461–465, Aug 2009.

55. Saikus, C. E., and R. J. Lederman, “Interventional cardiovascular magnetic resonance imaging a new opportunity for image-guided interventions,” *Jacc-Cardiovascular Imaging*, Vol. 2, pp. 1321–1331, Nov 2009.

56. Ratnayaka, K., A. Z. Faranesh, M. A. Guttman, O. Kocaturk, C. E. Saikus, and R. J. Lederman, “Interventional cardiovascular magnetic resonance: still tantalizing,” *Journal of Cardiovascular Magnetic Resonance*, Vol. 10, pp. –, Dec 29 2008.

57. Raman, V. K., and R. J. Lederman, “Interventional cardiovascular magnetic resonance imaging,” *Trends Cardiovasc Med*, Vol. 17, pp. 196–202, Aug 2007.

58. Lederman, R. J., “Cardiovascular interventional magnetic resonance imaging,” *Circulation*, Vol. 112, pp. 3009–17, Nov 8 2005.

59. Horvath, K. A., M. Li, D. Mazilu, M. A. Guttman, and E. R. McVeigh, “Real-time magnetic resonance imaging guidance for cardiovascular procedures,” *Semin Thorac Cardiovasc Surg*, Vol. 19, pp. 330–5, Winter 2007.

60. Muthurangu, V., and R. S. Razavi, “The value of magnetic resonance guided cardiac catheterisation,” *Heart*, Vol. 91, pp. 995–996, Aug 2005.

61. Bock, M., and F. K. Wacker, “Mr-guided intravascular interventions: techniques and applications,” *J Magn Reson Imaging*, Vol. 27, pp. 326–38, Feb 2008.

62. Quick, H. H., H. Kuehl, G. Kaiser, S. Bosk, J. F. Debatin, and M. E. Ladd, “Inductively coupled stent antennas in mri,” *Magn Reson Med*, Vol. 48, pp. 781–90, Nov 2002.

63. Chanu, A., O. Felfoul, G. Beaudoin, and S. Martel, “Adapting the clinical mri software environment for real-time navigation of an endovascular untethered ferromagnetic bead for future endovascular interventions,” *Magn Reson Med*, Vol. 59, pp. 1287–97, Jun 2008.

64. Kanal, E., F. G. Shellock, and L. Talagala, “Safety considerations in mr imaging,” *Radiology*, Vol. 176, pp. 593–606, Sep 1990.

65. Ham, C. L., J. M. Engels, G. T. van de Wiel, and A. Machielsen, “Peripheral nerve stimulation during mri: effects of high gradient amplitudes and switching rates,” *J Magn Reson Imaging*, Vol. 7, pp. 933–7, Sep-Oct 1997.

66. Schaefer, D. J., “Safety aspects of switched gradient fields,” *Magn Reson Imaging Clin N Am*, Vol. 6, pp. 731–48, Nov 1998.

67. Konings, M. K., L. W. Bartels, H. F. Smits, and C. J. Bakker, “Heating around intravascular guidewires by resonating rf waves,” *J Magn Reson Imaging*, Vol. 12, pp. 79–85, Jul 2000.

68. Nitz, W. R., A. Oppelt, W. Renz, C. Manke, M. Lenhart, and J. Link, “On the heating of linear conductive structures as guide wires and catheters in interventional mri,” *J Magn Reson Imaging*, Vol. 13, pp. 105–14, Jan 2001.

69. Pictet, J., R. Meuli, S. Wicky, and J. J. van der Klink, “Radiofrequency heating effects around resonant lengths of wire in mri,” *Phys Med Biol*, Vol. 47, pp. 2973–85, Aug 21 2002.

70. Yeung, C. J., and E. Atalar, “Rf transmit power limit for the barewire loopless catheter antenna,” *J Magn Reson Imaging*, Vol. 12, pp. 86–91, Jul 2000.

71. Triventi, M., E. Mattei, G. Calcagnini, F. Censi, P. Bartolini, W. Kainz, and H. Bassen, “Magnetic-resonance-induced heating of implantable leads,” *Ann Ist Super Sanita*, Vol. 43, no. 3, pp. 229–40, 2007.

72. Mattei, E., M. Triventi, G. Calcagnini, F. Censi, W. Kainz, G. Mendoza, H. I. Bassen, and P. Bartolini, “Complexity of mri induced heating on metallic leads: experimental measurements of 374 configurations,” *Biomed Eng Online*, Vol. 7, p. 11, 2008.

73. Martin, A. J., B. Baek, G. Acevedo-Bolton, R. T. Higashida, J. Comstock, and D. A. Saloner, “Mr imaging during endovascular procedures: an evaluation of the potential for catheter heating,” *Magn Reson Med*, Vol. 61, pp. 45–53, Jan 2009.

74. Weiss, S., P. Vernickel, T. Schaeffter, V. Schulz, and B. Gleich, “Transmission line for improved rf safety of interventional devices,” *Magn Reson Med*, Vol. 54, pp. 182–9, Jul 2005.

75. Ladd, M. E., and H. H. Quick, “Reduction of resonant rf heating in intravascular catheters using coaxial chokes,” *Magn Reson Med*, Vol. 43, pp. 615–9, Apr 2000.

76. Seeber, D., J. Jevtic, and A. Menon, “Floating shield current suppression trap,” *Concepts in Magnetic Resonance Part B: Magnetic Resonance Engineering*, Vol. 21B, pp. 26–31, April 2004.

77. Greatbatch, W., V. Miller, and F. G. Shellock, “Magnetic resonance safety testing of a newly-developed fiber-optic cardiac pacing lead,” *J Magn Reson Imaging*, Vol. 16, pp. 97–103, Jul 2002.

78. Memis, O. G., Y. Eryaman, O. Aytur, and E. Atalar, “Miniaturized fiber-optic transmission system for mri signals,” *Magnetic Resonance in Medicine*, Vol. 59, pp. 165–173, Jan 2008.

79. S, W., D. B, L. O, W. J, and K. S, “Comparison of rf heating in cables equipped with different types of current limitations [e-poster],” *In Proceedings of ISMRM 19th Annual Meeting and Exhibition.*, Vol. 7-13, May 2011.

80. Yeung, C. J., R. C. Susil, and E. Atalar, “Rf safety of wires in interventional mri: using a safety index,” *Magn Reson Med*, Vol. 47, pp. 187–93, Jan 2002.

81. Yeung, C. J., P. Karmarkar, and E. R. McVeigh, "Minimizing rf heating of conducting wires in mri," *Magn Reson Med*, Vol. 58, pp. 1028–34, Nov 2007.

82. Bassen, H., W. Kainz, G. Mendoza, and T. Kellom, "Mri-induced heating of selected thin wire metallic implants– laboratory and computational studies– findings and new questions raised," *Minim Invasive Ther Allied Technol*, Vol. 15, no. 2, pp. 76–84, 2006.

83. van den Bosch, M. R., M. A. Moerland, J. J. W. Lagendijk, L. W. Bartels, and C. A. T. van den Berg, "New method to monitor rf safety in mri-guided interventions based on rf induced image artefacts," *Med Phys*, Vol. 37, pp. 814–821, Feb 2010.

84. Zanchi, M. G., R. Venook, J. M. Pauly, and G. C. Scott, "An optically coupled system for quantitative monitoring of mri-induced rf currents into long conductors," *Ieee Transactions on Medical Imaging*, Vol. 29, pp. 169–178, Jan 2010.

85. Reiter, T., D. Gensler, O. Ritter, I. Weiss, W. Geistert, R. Kaufmann, S. Hoffmeister, M. T. Friedrich, S. Wintzheimer, M. During, P. Nordbeck, P. M. Jakob, M. E. Ladd, H. H. Quick, and W. R. Bauer, "Direct cooling of the catheter tip increases safety for cmr-guided electrophysiological procedures," *Journal of Cardiovascular Magnetic Resonance*, Vol. 14, Feb 1 2012.

86. Armenean, C., E. Perrin, M. Armenean, O. Beuf, F. Pilleul, and H. Saint-Jalmes, "Rf-induced temperature elevation along metallic wires in clinical magnetic resonance imaging: influence of diameter and length," *Magn Reson Med*, Vol. 52, pp. 1200–6, Nov 2004.

87. Akca, I. B., O. Ferhanoglu, C. J. Yeung, S. Guney, T. O. Tasci, and E. Atalar, "Measuring local rf heating in mri: Simulating perfusion in a perfusionless phantom," *J Magn Reson Imaging*, Vol. 26, pp. 1228–35, Nov 2007.

88. Liu, C. Y., K. Farahani, D. S. Lu, G. Duckwiler, and A. Oppelt, "Safety of mri-guided endovascular guidewire applications," *J Magn Reson Imaging*, Vol. 12, pp. 75–8, Jul 2000.

89. Susil, R. C., C. J. Yeung, and E. Atalar, "Intravascular extended sensitivity (ives) mri antennas," *Magn Reson Med*, Vol. 50, pp. 383–90, Aug 2003.

90. "Astm f2119-07: Standard test method for evaluation of mr image artifacts from passive implants," *American Society for Testing and Materials.*

91. "Astm f2182-11a: Standard test method for measurement of radio frequency induced heating on or near passive implants during magnetic resonance imaging," *American Society for Testing and Materials.*

92. "Nema publishes ms 1-2008 determination of signal-to-noise ratio (snr) in diagnostic magnetic resonance imaging," *National Electrical Manufacturer Association.*

93. Weibell, F. J., *Electrical Safety in the Hospital, Annals of Biomedical Engineering*, Vol. 2, 1974.

94. Spalding, L. E. S., W. P. Carpes, and N. J. Batistela, "A method to detect the microshock risk during a surgical procedure," *Ieee Transactions on Instrumentation and Measurement*, Vol. 58, pp. 2335–2342, Jul 2009.

95. "Iec 60601-1 - medical equipment, medical electrical equipment - part 1: General requirements for basic safety and essential performance," *International Electrotechnical Commission.*

96. El-Sharkawy, A. M., P. P. Sotiriadis, P. A. Bottomley, and E. Atalar, "Absolute temperature monitoring using rf radiometry in the mri scanner," *IEEE Trans Circuits Syst I Regul Pap*, Vol. 53, pp. 2396–2404, Nov 2006.

97. Atalar, E., "Radiofrequency safety for interventional mri procedures," *Acad Radiol*, Vol. 12, pp. 1149–57, Sep 2005.

98. Nyenhuis, J. A., P. Sung-Min, R. Kamondetdacha, A. Amjad, F. G. Shellock, and A. R. Rezai, "Mri and implanted medical devices: basic interactions with an emphasis on heating," *Device and Materials Reliability, IEEE Transactions on*, Vol. 5, no. 3, pp. 467–480, 2005.

99. Buchli, R., P. Boesiger, and D. Meier, "Heating effects of metallic implants by mri examinations," *Magn Reson Med*, Vol. 7, pp. 255–61, Jul 1988.

100. Luechinger, R., V. A. Zeijlemaker, E. M. Pedersen, P. Mortensen, E. Falk, F. Duru, R. Candinas, and P. Boesiger, "In vivo heating of pacemaker leads during magnetic resonance imaging," *Eur Heart J*, Vol. 26, pp. 376–383, Feb 2005.

101. Roguin, A., M. M. Zviman, G. R. Meininger, E. R. Rodrigues, T. M. Dickfeld, D. A. Bluemke, A. Lardo, R. D. Berger, H. Calkins, and H. R. Halperin, "Modern pacemaker and implantable cardioverter/defibrillator systems can be magnetic resonance imaging safe - in vitro and in vivo assessment of safety and function at 1.5 t," *Circulation*, Vol. 110, pp. 475–482, Aug 3 2004.

102. Shively, M., B. Riegel, D. Waterhouse, D. Burns, K. Templin, and T. Thomason, "Testing a community level research utilization intervention," *Applied Nursing Research*, Vol. 10, pp. 121–127, Aug 1997.

103. Sonmez, M., C. E. Saikus, J. A. Bell, D. N. Franson, M. Halabi, A. Z. Faranesh, C. Ozturk, R. J. Lederman, and O. Kocaturk, "Mri active guidewire with an embedded temperature probe and providing a distinct tip signal to enhance clinical safety," *Journal of cardiovascular magnetic resonance : official journal of the Society for Cardiovascular Magnetic Resonance*, Vol. 14, p. 38, 2012.

104. Overall, W. R., J. M. Pauly, P. P. Stang, and G. C. Scott, "Ensuring safety of implanted devices under mri using reversed rf polarization," *Magn Reson Med*, Vol. 64, pp. 823–33, Sep 2010.

105. Nordbeck, P., F. Fidler, I. Weiss, M. Warmuth, M. T. Friedrich, P. Ehses, W. Geistert, O. Ritter, P. M. Jakob, M. E. Ladd, H. H. Quick, and W. R. Bauer, "Spatial distribution of rf-induced e-fields and implant heating in mri," *Magn Reson Med*, Vol. 60, pp. 312–9, Aug 2008.